Nonlinear and Quantum Superresolution and Fast-Light Pulse-Distortion Management

by

Heedeuk Shin

Submitted in Partial Fulfillment of

the Requirements for the Degree

Doctor of Philosophy

Supervised by

Professor Robert W. Boyd

The Institute of Optics
Arts, Sciences and Engineering
Edmund A. Hajim School of Engineering and Applied Sciences

University of Rochester
Rochester, New York

2011

To My Wife, My Son and My Parents

Curriculum Vitae

Heedeuk Shin was born in Seoul, Korea in 1974. He graduated *Summa Cum Laude* with a Bachelor of Science in Physics from Hanyang University in Seoul, Korea in 2000. He, also, obtained a Master of Science in Physics from Hanyang University in 2002 and received an Honor Scholarship for 2 years. His master's thesis was entitled 'Analysis for the photo-induced molecular reorientation in an azobenzene polymer' and was supervised by Professor Cha-Hwan Oh. In 2002 and 2003, he worked at Quantum Photonics Science Research Center in Hanyang University. As a full-time researcher, he researched surface relief grating (SRG) on polymers containing azobenzene molecules as a substrate for self-assembly photonic bandgap crystals. In 2004, he began the Ph.D. program at the Institute of Optics, University of Rochester and joined the Nonlinear Optics group directed by Prof. Robert W. Boyd. Under the supervision of Prof. Boyd, he has worked on pulse distortion management in fast/slow light propagation, sub-wavelength interferometry lithography using nonlinear effects, large nonlinear optical response of ferroelectric thin films, holographic single-photon sorter, and quantum imaging and lithography.

Publications related to the thesis

1. "Quantum spatial super-resolution by optical centroid measurement," H. Shin, K. C. Chan, H. J. Chang, and R. W. Boyd, Phys. Rev. Lett. (preparing for publication).

2. "Reducing pulse distortion in fast-light pulse propagation through an erbium-doped fiber amplifier using a mutually incoherent background field," Heedeuk Shin, Aaron Schweinsberg, and Robert W. Boyd, Opt. Comm. **282**, 2085 (2009).

3. "Reducing pulse distortion in fast-light pulse propagation through an erbium-doped fiber amplifier," Heedeuk Shin, Aaron Schweinsberg, George Gehring, Katie Schwertz, Hye Jeong Chang, Robert W. Boyd, Q-Han Park and Daniel J. Gauthier, Opt. Lett. **32**, 906 (2007), [April 2007 issue of Virtual Journal of Ultrafast Science]

4. "Implementation of sub-Rayleigh resolution lithography using an N-photon absorber," Hye Jeong Chang, Heedeuk Shin, Malcolm N. OSullivan-Hale and Robert W. Boyd, J. Modern Optics **53**, 2271 (2006).

Other publications

1. "Tunable optical time delay of quantum signals using a prism pair," G. M. Gehring, H. Shin, R. W. Boyd, C. Kim, and B. S. Ham, Opt. Express. **18**, 19156 (2010).

2. "Quantum Ghost Image Identification with Correlated Photon Pairs," M. Malik, H. Shin, P. Zerom, and R. W. Boyd, Phys. Rev. Lett. **104**, 163602 (2010). [May 2010 issue of Virtual Journal of Quantum Information]

3. "Observation of a Microscopic Cascaded Contribution to the Fifth-Order Nonlinear Susceptibility," Ksenia Dolgaleva, Heedeuk Shin, and Robert W. Boyd, Phys. Rev. Lett. **103**, 113902 (2009). [September 2009 issue of Virtual Journal of Quantum Information]

4. "Discriminating Orthogonal Single Photon Images," Curtis J. Broadbent, Petros Zerom, Heedeuk Shin, John C. Howell, and Robert W. Boyd, Phys. Rev. A **79**, 033802 (2009). [March 2009 issue of Virtual Journal of Quantum Information]

5. "Large nonlinear optical response of polycrystalline Bi3.25La0.75Ti3O12 ferroelectric thin films on quartz substrates," Heedeuk Shin, Hye Jeong Chang, Robert W. Boyd, M. R. Choi, and W. Jo, Opt. Lett. **32**, 2453 (2007).

6. "Propagation of smooth and discontinuous pulses through materials with very large or very small group velocities," M. S. Bigelow, N. N. Lepeshkin, H. Shin, and R. W. Boyd, J. of Phys.: Condens. Matter **18**, 3117 (2006).

7. "Synthesis and Photoisomerization Properties of Polynorbornenes with Azobenzene Chromophores," S. H. Kang, H. D. Shin, C. H. Oh, D. H. Choi, and K. H. park, Bull. Korean Chem. Soc. **23**, 957 (2002).

8. "Determination of transition rate constants of trans-cis isomerization in a poly(malonic ester) containing disperse red 1," H. D. Shin, W. J. Joo, C. H. Oh, P. S. Kim, and Y. K. Han, J. of Chem. Phys., **117**, 1677 (2002).

9. "Novel mechanism of fast relaxation of photo-induced anisotropy in a poly(malonic esters) containing p-cyanoazobenzene," Won-Jae Joo, Hee-Deuk Shin, Cha-Hwan Oh, Seok-Ho Song, Pill-Soo Kim, Bong-Soo Ko, and Yang-Kyoo Han, J. of Chem. Phys., **113**, 8848 (2000).

Conference Papers related the thesis

1. "Experimental Demonstration of Quantum Superresolution by Optical Centroid Measurement," H. Shin, K. W. C. Chan, H. J. Chang, and R. W. Boyd, *Frontier in Optics* (2010).

2. "Pulse-distortion Management Using the Pulse-on-Background Method and Multiple Closely Spaced Gain Lines in Slow/Fast Light Propagation," H. Shin, Z. Shi, A. Schweinsberg, G. Gehring, and R. W. Boyd, *Frontier in Optics* (2008).

3. "Reducing pulse distortion in fast light pulse propagation by Pulse-on-Background method through an erbium-doped fiber amplifier," H. Shin, A. Schweinsberg, G. Gehring, and R. W. Boyd, *CLEO / Pacific Rim* (2007).

4. "Sub-Rayleigh lithography using a Multi-Photon Absorber," H. Shin, M. N. O'Sullivan-Hale, H. J. Chang, and R. W. Boyd *ICQI* (2007).

5. "Pulse broadening or compression in fast-light pulse propagation through an erbium-doped fiber amplifier," H. Shin, A. Schweinsberg, G. M. Gehring, K. Schwertz, H. J. Chang, Q. Park, D. J. Gauthier, and R. W. Boyd, *CLEO/QELS* (2007).

6. "Demonstration of Sub-Rayleigh Lithography Using a Multi-Photon Absorber", H. Shin, H. J. Chang, M. N. O'Sullivan-Hale, S. Bentley, and R. W. Boyd, *Frontier in Optics* (2006).

7. "Sub-Rayleigh lithography using an N-photon absorber," H. J. Chang, H. Shin, M. N. O'Sullivan-Hale, and R. W. Boyd, *CLEO* (2006).

Other conference papers

1. "Quantum imaging: enhanced image formation using quantum states of light," R. W. Boyd, K. W. C. Chan, A. Jha, M. Malik, C. O'Sullivan, H. Shin, and P. Zerom, Proc. SPIE, Vol. 7342, 73420B (2009).

2. "Experimental separation of microscopic cascading induced by local-field effects," K. Dolgaleva, H. Shin, R. W. Boyd, and J. E. Sipe, *FiO/LS* (2008).

3. "Microscopic Cascading Induced by Local-Field Effects as a Tool for Quantum Lithography," K. Dolgaleva, H. Shin, R. W. Boyd, and J. E. Sipe, *ICQI* (2008).

4. "Giant Nonlinear Optical response of Bi3.25La0.75Ti3O12 Ferroelectric thin films on quartz substrate," H. Shin, H. J. Chang, R. W. Boyd, M. R. Choi, W. Jo, *CLEO / Pacific Rim* (2007).

5. "Progress in Quantum Lithography," R. W. Boyd, H. J. Chang, H. Shin, and M. C. O'Sullivan-Hale, Proc. SPIE, Vol. 5893, 58930G-1 (2005).

Acknowledgments

Though only my name appears on the cover of this dissertation, this thesis could not have been possible without the assistance of many people whose contributions I gratefully acknowledge.

First and foremost, I would like to thank my advisor Professor Robert W. Boyd for supporting me to develop as a scientist. The knowledge, joy and enthusiasm he has for his research were always contagious and motivational for me. Also without his politeness and constant encouragement, along with his delightful sense of humour about life and science, I could easily have lost my mind by the research projects.

I gratefully acknowledge great collaborations and useful discussions of the subject matters of the articles published in scientific journals with Professor John C. Howell, Professor Byoung Seung Ham, Professor Q-Han Park, Professor Daniel J. Gauthier, Professor William Jo, Professor Chil-min Kim, Professor Nick Lepeshkin, Professor Matt Bigelow, Dr. Annabel A. Muenter, and Professor Sean Bentley. I also thank Dr. Semyon Papernov and Brian McIntyre for technical support and the great courses in the measurement of the AFM and SEM images.

I am grateful to Professor Pill-Soo Kim, Professor Young-Pak Lee, Professor Kisik Kim, Professor Seok-Ho Song, Dr. Hoon Soo Kang, and Professor Cha-Hwan Oh for their support and encouragement of my study. I would especially like to acknowledge Professor Cha-Hwan Oh for his mentoring to make some crucial decisions that cardinally changed my future towards the best.

I thank all the professors of the Institute of Optics for their excellent courses exploring all of the various areas of optics. The Ph.D. program with such great courses prepares me to carry out independent creative research. I would especially like to thank Professor Govind P. Agrawal and Dr. Svetlana Lukishova for the insightful telecommunications and quantum optics laboratory courses. I have got good ideas and intuition about my research from what I have learned during the courses.

I am thankful to Professor Carlos R. Stroud and Professor Nicholas P. Bigelow for agreeing to serve on my Ph. D. committee and for their suggestions and comments on how to improve my Ph. D. thesis.

I would like to thank Maria Schnitzler, Lissa Cotter, Noelene Votens, Betsy Benedict, Gina Kern, Lori Russell, Marie Banach, and Per Adamson for the excellent support. Without their help, I could not succeed to complete my program.

I am endlessly grateful to the other members of Professor Boyd's research group. I would like to thank Colin O'Sullivan and Dr. Anand Jha for the fruitful chalk talks about the quantum optics work. I thank Dr. Kam Wai Clifford Chan, Dr. Ksenia Dolgaleva, Dr. Giovanni Piredda, Aaron Schweinsberg, Petros Zerom, George Gehring, Mehul Malik, Andreas Liapis, Boshen Gao, and Brandon Rodenburg for the wonderful collaborations and great discussions. I also acknowledge Joe Vornehm, Luke Bissell and Zhimin Shi for for discussing research problems and sharing the joyful experience with children.

I have many great friends whom I met in Rochester: Dr. Seong-Jong Woo, Dr.

Kyeseung Lee, Dr. Zeguang Ren, Fran C. Paxson, Vicki Duval, Kiwan Park, Jaewon Park, Jaehong Park, Taekyong Hwang, Seong Keun Cho, Yun Jin Choi, Joseph Choi, and Kyoung-Seok Yoo. I would like to give a special thanks to Hyup Woo Lee and Kyoung Hee Kim for being my son's Godparents. I also thank to my best friends YongJun Lee and HyungJoo Youn for the constant friendship.

This work would have not been possible without my endlessly supportive family. I devote my deepest gratitude to my wife, Hye Jeong Chang for her understanding and love. She was also an excellent colleague for my research, and we could achieve many great results together during the past few years. I also love my son, Matthew Limkyu Shin. It is really joyful watching him grow up. I am endlessly grateful to other members of my family, especially, my brother Hee-Myoung Shin, my sister Hee-Sook Shin, my sister-in-law Soo-Hyun Lee, my aunt Kyoung-Hwa Kim and my uncle YoungKi Choi, my wife's sister Myoung-A Chang and her husband Ji-hun Lee, my wife's brother Sewon Chang and his wife Ik-Ran Um, and my parents-in-law Sun-Sang Chang and Keum-Ja Ham.

Finally, I dedicate this thesis to my parents Chang-Hee Shin and Kyoung-Ja Kim. Words can not express the depth of my gratitude for what you have done for me.

Abstract

I describe my research on two topics in the area of experimental nonlinear optics: interferometric superresolution and fast-light pulse-distortion management. In the first topic, I study means to achieve enhanced resolution over the classical Rayleigh limit through the use of nonlinear and quantum optical methods. In the second topic, I suggest and demonstrate a new procedure for fast-light pulse-distortion management in a saturable gain medium.

The minimum peak-to-peak distance of an optical interference fringe pattern is half of the wavelength of recording light at grazing incidence angle, called the Rayleigh limit. I experimentally demonstrate two optical methods to achieve an enhancement of resolution over the classical Rayleigh limit. First, a nonlinear optical phase-shifted-grating method is experimentally demonstrated, achieving two- and three-fold enhanced resolution. Poly(methyl-methacrylate) (PMMA) is used as a real N-photon absorbing lithographic recording material. In addition, I generated a non-sinusoidal pattern by irradiating a PMMA film with non-uniform phase shifts between exposures. Second, I experimentally demonstrate quantum superresolution by measuring optical centroids of path-entangled photons instead of using inefficient multi-photon absorbing detectors. Superresolution of interference patterns with higher detection efficiency is achieved. These results place us one step closer to the realization of superresolution in lithography and quantum imaging systems.

In addition, I describe the pulse distortion in slow-/fast-light pulse propagation. Anomalous dispersion produced by coherent population oscillations in an erbium doped fiber can induce fast-light pulse propagation, but it also produces pulse distortion. In this thesis, we suggest a new procedure for pulse-distortion management. Two competing mechanisms determine the output pulse-width in an erbium doped fiber, and we can adjust the two mechanisms by adding a constant background field to minimize pulse-shape distortion. This technique, referred to as the pulse-on-background method, is successfully demonstrated under various experimental conditions. Numerical calculations give results well-matched with the experimental results.

Contents

List of Tables

List of Figures

Foreword

The contents of this thesis come from various research projects during my doctoral studies at University of Rochester, many of which are collaborative projects with my advisor, my fellow group members as well as other researchers at or outside of University of Rochester.

Chapter 2 is an extended version of a research paper entitled "Implementation of sub-Rayleigh-resolution lithography using an N-photon absorber" published in *Journal of Modern Optics*, **53**, 2271-2277 (2006). This paper is the result of a joint work with H. J. Chang, H. Shin, M. N. O'Sullivan-Hale, and R. W. Boyd at the University of Rochester. H. J. Chang and R. W. Boyd designed the project and experiments, and H. J. Chang wrote the paper for publication. M. N. O'Sullivan-Hale carried out the parts of experimental work and was involved in the discussion of the forming of the paper. I made significant contributions to the design and building of the experimental setups, measurements, and data analysis. Note that I am the second author of the published paper.

Chapter 3 is primarily based on a collaboration with R. W. Boyd at the University

of Rochester, K. W. C. Chan at Rochester Optical Manufacturing Company, and H. J. Chang at Korean Intellectual Property Office. R. W. Boyd designed the project. I designed the experiments and carried out most of the experimental work and data analysis. K. W. C. Chan and H. J. Chang performed parts of the theoretical and experimental work. I also wrote a manuscript for publication entitled "Quantum spatial superresolution by an optical centroid measurement," and it is submitted to *Physical Review Letters*.

Chapter 4 is the result of a joint work with A. Schweinsberg, G. Gehring, K. Schwertz, H. J. Chang and R. W. Boyd at the University of Rochester, Q. Park at Korea University, and D. J. Gauthier at Duke University. R. W. Boyd and I designed the project. I designed the experiments and performed most of the experimental work and data analysis. A. Schweinsber, G. Gehring, and K. Schwertz carried out parts of the experimental work. All coauthors were involved in continuous discussions. Note that I am the first author of the two research papers that came out of this collaboration entitled "Reducing pulse distortion in fast-light pulse propagation through an erbium-doped fiber amplifier," published in *Optics Letters* **32**, 906–908 (2007) and "Reducing pulse distortion in fast-light pulse propagation through an erbium-doped fiber amplifier using a mutually incoherent background field," published in *Optics Communications* **282**, 20852087 (2009).

Chapter 1

Background

1.1 Introduction

Nonlinear optics is the study of phenomena that occur as a consequence of the modification of the optical properties of a material system by the presence of light [1]. In this thesis, I describe my research in experimental nonlinear optics. In the first topic, I investigate means of spatial resolution enhancement of interference fringe patterns through the use of nonlinear and quantum optical methods. In the second topic, I suggest a new procedure for fast-light pulse-distortion management in a saturable gain medium and demonstrate the method using an erbium doped fiber amplifier.

Optical interference can be interpreted as the superposition of two or more classical electro-magnetic fields or that of the quantum probability amplitudes for a photon to take one of several possible paths. The nature of interference is of interest to

physicists and engineers due to its wide range of applications such as metrology [2], holography [3], lithography [4], rotation [5], astronomical optical interferometry [6], gravitational-wave observation [7] and optical coherence tomography [8]. The ability of generating arbitrary patterns makes optical interference even more useful for its practical implementation in lithography and imaging [9, 10, 11, 12, 13, 14]. Since the interferometric resolution is ultimately limited by diffraction, referred to as the Rayleigh limit [15], one of the biggest issues in optical lithography and imaging is to generate the smallest possible spot or line with a given imaging system. Due to the diffraction limit, the minimum peak-to-peak distance of the recorded pattern is half of the wavelength of recording light at grazing incidence angle. The most common way to improve the interferometric resolution is using a light source of shorter wavelength and lens systems with larger numerical apertures [16]. Such a conventional way, however, requires costly optical systems because of absorption of the optical system, new light sources, and new optical recording materials.

Besides developing shorter-wavelength optical systems, a lot of methods have been proposed to improve the interference fringe resolution without changing the wavelength of light. The proposed methods can be classified into two groups, nonlinear methods using the classical state of light and quantum methods using the quantum state of light. The nonlinear methods can be described as follows: The multi-exposure method was proposed by using nonlinear photosensitivity and the multiple exposure technique [17]. An interference fringe pattern with two-fold spatial resolution

enhancement was recorded in an alternate way on a two-photon commercial photographic film using two-photon absorption employing a multiplicity of two-photon excitation frequencies [18, 19]. However, the film is not a lithographic material, and the resulting pattern had a visibility of only 3%. In addition, a thermal light source can produce a sub-wavelength interference pattern in a joint intensity measurement [20]. The phase-shifted grating method using multi-photon absorption with multiple exposures (M) shows that spatial resolution enhancement by a factor of M is possible [21, 22, 23]. Multi-photon resonance or multiple resonances can also achieve a spatial resolution of $\lambda/(2N)$ [24, 25, 14]. Furthermore, the creation of superresolution pattern was studied by using the dark states formed by the interaction between atoms and optical fields [26]. On the other hand, quantum lithography, which utilizes path-entangled multi-photon states and multi-photon absorption, was proposed to beat the diffraction limit by a factor of N [4]. In this thesis, I investigate means to achieve an enhancement of resolution over the classical Rayleigh limit and present experimental demonstrations of nonlinear and quantum optical methods.

In the second half of this dissertation, the group velocity of light is studied. The speed of light has been studied in great detail for a long period of time [27]. The speed of light in a vacuum, usually denoted by c, is one of the most fundamental to all physical constants. For example, the meter was redefined by the 17th Conférence Générale des Poids et Mesures (CGPM) in 1983 as the length of the path traveled by light in vacuum during a time interval of 1/299 792 458 of a second [28]. However,

it is well known that when an optical pulse propagates through dispersive media, the pulse experiences large or small refractive index near a material resonance [29, 30]. The first slow- and fast-light pulse propagation was observed in a resonant system [31, 32], but the pulse experienced very strong resonant absorption. Strong dispersion with relatively low loss was reported by using the technique of electromagnetically induced transparency (EIT) [33, 34]. The spectral transparency window induced by EIT is so narrow that "ultra-slow" pulse propagation was observed in Pb vapor cell and a Bose-Einstein condensate [35, 36]. Ultra-slow light in a solid medium was first demonstrated at a cryogenic temperature of 5 K [37]. The first use of room-temperature solid-state materials [38, 39] opened the possibility of using slow-light effect to develop practical devices via various mechanisms, such as coherent population oscillation (CPO) [40], stimulated Brillouin scattering (SBS) [41], coupled-resonator induced transparency (CRIT) [42], stimulated Raman scattering (SRS) [43], and wave mixing in semiconductor optical amplifiers (SOA) [44, 45].

Recently, the use of controllable slow- and fast-light pulse propagation through material systems has been studied intensively due to its useful applications, such as tunable optical delay lines, optical buffers, and true time delay methods for synthetic aperture radar [46, 47]. Pulse distortion due to material dispersion is one of the limits of optical pulse delay or advancement, and several methods have been suggested for reducing pulse distortion in slow- and fast-light propagation [48, 49, 50, 51, 52, 53, 54, 55, 56]. In this thesis, I study a new method to reduce pulse distortion in an

erbium doped fiber amplifier by adding a proper amount of optical continuous wave background to pulses.

This chapter is organized as follows. The standard spatial interference fringe pattern is described by quantum mechanics in Section 1.2. The multi-photon absorption process and the interference patterns by means of MPA using the classical state of light are studied in Section 1.3, and Quantum lithography using the quantum entangled states of light is described in Sections 1.4. Sections 1.5 briefly introduces the nonlinear optical process of parametric down conversion. In Section 1.6, the fundamentals of slow- and fast-light pulse propagation in a dispersive medium are described. Coherent population oscillation, a mechanism of slow- and fast-light propagation, is discussed in Section 1.7. Slow- and fast-light pulse propagation in erbium doped fiber is studied in Section 1.8. Finally, Section 1.9 presents the summary.

1.2   Interference fringe pattern

Interferometry can be characterized by quantum mechanics using photon operators and two-dimensional matrices representing individual optical elements [4, 57]. This section describes spatial interference in a MachZehnder interferometer as shown in Fig. 1.1. The phase differential due to the path-length difference between the upper and lower paths of the interferometer can be replaced by a single phase shifter (PS) located in the upper path. Most optical elements, such as beam splitter, mirror, and
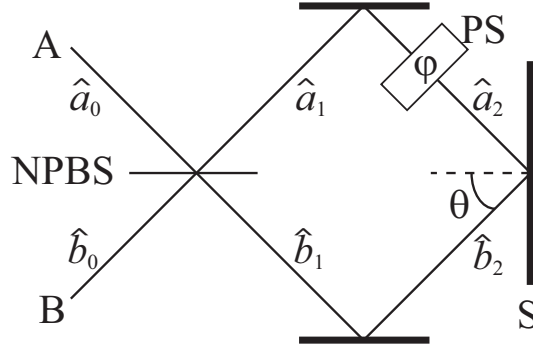
Figure 1.1: Schematic diagram of an interferometer setup.

phase shifter, can respectively be expressed by two-dimensional matrices as follows:

$$
\text{NPBS} = \frac{1}{\sqrt{2}} \begin{pmatrix} 1 & i \\ i & 1 \end{pmatrix},
$$

$$
\text{M} = \begin{pmatrix} -1 & 0 \\ 0 & -1 \end{pmatrix},
$$

$$
\text{PS} = \begin{pmatrix} e^{i\varphi} & 0 \\ 0 & 1 \end{pmatrix}, \tag{1.1}
$$

where $\varphi = 2\pi(2\sin\theta/\lambda)\,x$ is the phase differential, x is the lateral dimension on the substrate, and θ is the incidence angle of recording beams on the substrate.

Consider the schematic setup for interferometry, illustrated in Fig. 1.1, where $\hat{a}_0$, $\hat{a}_1$, $\hat{a}_2$, $\hat{b}_0$, $\hat{b}_1$, and $\hat{b}_2$ are photon annihilation operators at each position of the interferometer, NPBS means 50:50 non-polarizing beam splitter, and S indicates a substrate. The input photons ($\hat{a}_0$ and $\hat{b}_0$) at ports A and B, respectively, arrive at

the substrate varying their modes to $\hat{a}_2$ and $\hat{b}_2$ by

$$\begin{pmatrix} \hat{a}_2 \\ \hat{b}_2 \end{pmatrix} = \begin{pmatrix} e^{i\varphi} & 0 \\ 0 & 1 \end{pmatrix} \begin{pmatrix} -1 & 0 \\ 0 & -1 \end{pmatrix} \frac{1}{\sqrt{2}} \begin{pmatrix} 1 & i \\ i & 1 \end{pmatrix} \begin{pmatrix} \hat{a}_0 \\ \hat{b}_0 \end{pmatrix}. \tag{1.2}$$

The field annihilation operators $\hat{a}_2$ and $\hat{b}_2$ of two upper and lower paths at the imaging plane are given by

$$\hat{a}_2 = \frac{-1}{\sqrt{2}} \left(e^{i\varphi} \hat{a}_0 + i\, e^{i\varphi} \hat{b}_0 \right),$$
$$\hat{b}_2 = \frac{-1}{\sqrt{2}} \left(i\, \hat{a}_0 + \hat{b}_0 \right), \tag{1.3}$$

and the total field annihilation operator $\hat{c}$ at the substrate is

$$\hat{c} = \frac{1}{\sqrt{2}} (\hat{a}_2 + \hat{b}_2)$$
$$= \frac{-1}{2} \left[(i + e^{i\varphi}) \hat{a}_0 + (1 + ie^{i\varphi}) \hat{b}_0 \right]. \tag{1.4}$$

The mean value of arriving photons (in other words, the intensity distribution, $I_{\hat{c}}$) at the substrate along the x-axis varies as

$$I_{\hat{c}} \equiv \langle \Psi_{\text{in}} | \hat{c}^\dagger \hat{c} | \Psi_{\text{in}} \rangle \equiv \langle \hat{c}^\dagger \hat{c} \rangle, \tag{1.5}$$

where $|\Psi_{\text{in}}\rangle$ is the input state. In a standard interferometer, the input state is a

coherent state at the A port and the vacuum state at the B port as,

$$|\Psi_{\text{in}}\rangle = |\alpha\rangle_A |0\rangle_B = |\alpha,\, 0\rangle, \tag{1.6}$$

and the intensity distribution can be described by

$$
\begin{aligned}
I_{\hat{c}}(x) &= \langle \alpha,\, 0 | \hat{c}^\dagger\, \hat{c} | \alpha,\, 0 \rangle \\
&= \left| \left(1 + e^{i\phi}\right) \right|^2 \langle \alpha,\, 0 | \hat{a}_0^\dagger\, \hat{a}_0 | \alpha,\, 0 \rangle / 4 \\
&= \frac{|\alpha|^2}{2}(1 + \cos\varphi) = \frac{I_0}{2}(1 + \cos\varphi) \\
&= \frac{I_0}{2}\{1 + \cos[2\pi(2\sin\theta/\lambda)\,x]\},
\end{aligned}
\tag{1.7}
$$

where $|\alpha|^2 \equiv I_0$ is the input intensity. Note that the intensity peak exists whenever φ varies by 2π, so the intensity of the interference fringe has a period of

$$\triangle x = \lambda/(2\sin\theta). \tag{1.8}$$

Thus, the interference pattern has its minimum value, $\lambda/2$ of the period at grazing incidence, and it is called Rayleigh limit. In the following sections, I describe nonlinear and quantum interferometry using the same photon operators and matrices.

1.3 Multi-photon absorption

It has been well known that when photons interact with matter (atoms or molecules), there is an energy exchange between the light field and the matter, referred to as the absorption or emission of photons by the matter. One-photon process is the most general field-matter interaction. If the energy of the incident light field is comparable to the spacing between the two energy levels involved in a molecular transition, an atom (or molecule) may absorb a photon through a transition from a ground energy level to an excited energy level, or conversely, the atom may emit a photon through a transition ending in a lower energy level.

The first theoretical prediction of field-matter interaction with more than one photon was done by Göppert-Mayer in 1931 [58]. In her doctoral dissertation, she foretold that a simultaneous two-photon absorption (2PA) process induces a transition to an excited energy level of an atom via an intermediate state. 30 years later, the first observation of 2PA was reported by using a strong laser light field [59]. Since then, enormous number of works has been reported due to the development of high energy lasers and new materials responding to two-photon absorption, three-photon absorption (3PA), four-photon absorption (4PA), and even higher-order multi-photon excitation [60].

The MPA process can be understood as a multi-step event introducing the concept of intermediate states between real energy levels as shown in Fig. 1.2 [60]. For simplicity, consider the two-photon absorption process. In the first step, an atom
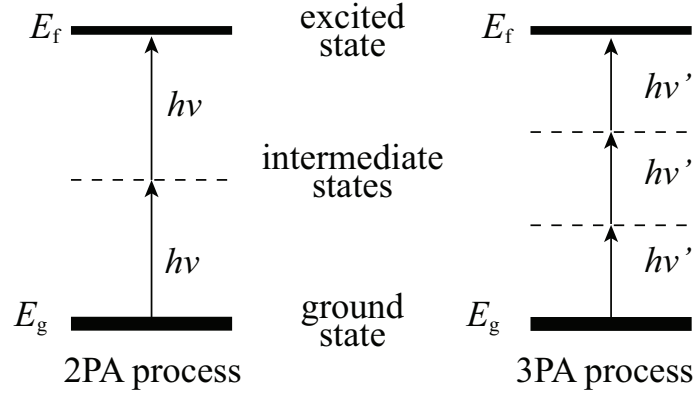
Figure 1.2: Schematic description of two-photon and three-photon absorptions.

absorbs one photon being excited to an intermediate state, so the atomic status can

be distributed somewhere between its ground state and excited state with a certain

probability. Because of the large range of the distribution uncertainty, the lifetime

in the intermediate state has to be short ($<$ 10 fs). In the second step, the same

atom absorbs another photon almost immediately to complete its transition from the

intermediate state to the excited state. Since each transition step is proportional to

the photon flux, the 2PA transition rate R depends on the quadratic power of light

intensity, I as

$$R \propto \sigma^{(2)}I^2 \tag{1.9}$$

where $\sigma^{(2)}$ is the 2PA cross-section of the molecule. The MPA cross-section determines

how sensitive the material is to the MPA process, and general materials have so small

value ($\sim 10^{-50}$ cm^4 s/photon for two-photon absorption and $\sim 10^{-85}$ cm^6 s^2/photon^2

for three-photon absorption [60, 61]) that it requires high optical intensity. The

TPA cross-section is sometimes quoted in the units of Goeppert-Mayer (GM, the name abbreviation of Göppert-Mayer), where 1 GM is 10^{-50}cm^{4}s/photon, and general materials have very small value about $0.1 \sim 1$ GM, so 2PA is a very rare phenomenon. Similarly, the 3PA transition rate has dependence on the third power of the light intensity and more of the same.

New multi-photon absorbing materials has been developed due to the great potentials of various applications based on multi-photon absorption, such as optical power limiting [62], frequency-upconversion lasing [63] and microscopy [64], optical data storage [65], and optical microfabrication [66]. These applications based on nonlinear optical multi-photon process has the advantages of (a) large penetration depth because of no linear absorption, (b) high spatial confinement of multi-photon interaction due to the nonlinear material's response, (c) the power of frequency up-conversion with tunability within a quite broad spectral range, (d) the change of nonlinear optical properties, such as refractive index, transmittance, and population, (e) no need of short wavelength laser, (f) effective rejection of background due to no linear and nonlinear response of materials, and (g) ultrafast response of the material due to the short lifetime of intermediate states. Especially, the first two features can be used to fabricate 3D microstructure with a spatial resolution much shorter than the excitation wavelength [67]. Due to the second advantage, photo-reactions will be occurred in smaller volume near the focal point position than the light intensity distribution because of the high-order power dependence of material's response.

This spatial confinement of multi-photon interaction will affect interference fringe patterns recorded on a multi-photon absorbing material. In this section, nonlinear interferometry will be described by quantum mechanics similarly with Section 1.2. The classical intensity distribution $I_{\hat{c}}(x)$ of a standard interferometer forms the interference fringe of Eq. 1.7. This intensity distribution can be recorded onto the N-photon absorber as a function of

$$I_{\hat{c}}(x)^N \equiv \langle \hat{c}^\dagger \ldots \hat{c}^\dagger \, \hat{c} \ldots \hat{c} \rangle / N!, \tag{1.10}$$

due to the nonlinear response of the N-photon absorbing material. The recorded pattern, $R(x)$, on the N-photon absorber is given by

$$
\begin{aligned}
R_{NLO}(x) \propto I_{\hat{c}}^N(x) &= \langle \alpha, \, 0|\hat{c}^{\dagger N} \, \hat{c}^N |\alpha, \, 0\rangle / N! \\
&= \left|\left(1 + e^{i\phi}\right)\right|^{2N} \langle \alpha, \, 0|\hat{a}_0^{\dagger N} \, \hat{a}_0^N |\alpha, \, 0\rangle / ((2)^{2N}/N!) \\
&= \frac{|\alpha|^{2N}}{N!2^N}\{1 + \cos[2\pi(2\sin\theta/\lambda)\, x]\}^N.
\end{aligned}
\tag{1.11}
$$

Note that the period of interference fringe does not change, but full width at half maximum (FWHM) of a period reduces from $\lambda/(4\sin\theta)$ for linear interference pattern to about $\lambda/(5.49\sin\theta)$ for 2PA interference pattern and to about $\lambda/(6.66\sin\theta)$ for 3PA interference pattern. The diminished width of MPA patterns can be used to fabricate sub-wavelength interference patterns on a multi-photon absorbing material and the detail will be described in Chapter 2. In the next section, I study quantum

interferometry using the same method in Section 1.2 and 1.3.

1.4   Quantum lithography

In 2000, Boto et al. proposed a new method to beat the Rayleigh limit in real multi-photon imaging systems using quantum entanglement and multi-photon absorption [4]. Consider the schematic setup for an interferometer, illustrated in Fig. 1.1. As shown in equation 1.4, the field annihilation operator at the imaging plane can be expressed by two input field annihilation operators $\hat{a}_0$ and $\hat{b}_0$ in the upper and lower input ports to the beam splitter. Consider the nonclassical input state $|\Psi_{\text{in}}\rangle = |1,\ 1\rangle_{A,B}$ indicating one photon at both A and B ports simultaneously. This photon-number state can be obtained by the parametric down-conversion (PDC) process which was predicted in 1968 [68] and was first observed experimentally in 1970 [69]. The detail about PDC will be studied in the next section. If the substrate is sensitive to the two-photon absorption process, the 2PA transition rate for the nonclassical state is given by

$$
\begin{aligned}
R_{QL}(x) &\propto \langle 1,\ 1|\hat{c}^\dagger\,\hat{c}^\dagger\,\hat{c}\,\hat{c}|1,\ 1\rangle/2! \\
&= \left|\frac{i}{2}\left(1 + e^{2i\varphi}\right)\right|^2 \langle 0,\ 0|0,\ 0\rangle/2 \\
&= \frac{1}{2}\left[1 + \cos(2\varphi)\right].
\end{aligned}
\tag{1.12}
$$
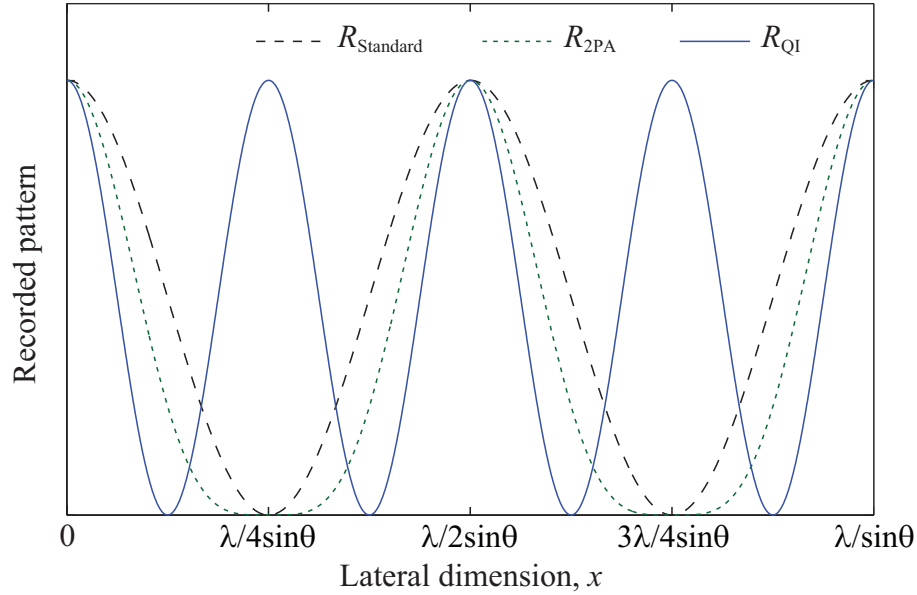
Figure 1.3: The recorded patterns by classical standard interferometry (black dashed), classical 2PA interferometry (green dotted), and quantum interferometry (blue solid) vs the lateral dimension, x.

Fig. 1.3 shows the recorded patterns for classical standard interferometry of equation 1.7 (R_{Standard}), classical 2PA interferometry of equation 1.11 for $N = 2$ (R_{2PA}), and quantum interferometry of equation 1.12 (R_{QI}) against the lateral dimension, x. The 2PA pattern has narrower features than the standard pattern, but quantum interferometry generate even narrower feature than 2PA. Another advantage of quantum interferometry is its visibility of one. Most of all, the quantum interferometry pattern as a function of $\cos(2\varphi)$ varies twice as fast as the classical standard interference pattern.

This two-fold enhanced resolution of quantum interferometry is caused by quantum entanglement. The quantum entanglement is a property of the quantum mechanical state of a composite system which cannot be written as a product of the states of

individual subsystems, even if the individual subsystems are spatially separated [70].

For example, if two noninteracting subsystems A and B have individually two possible states $|0\rangle$ and $|1\rangle$, $\left(|1\rangle_A|0\rangle_B + |0\rangle_A|1\rangle_B\right)/\sqrt{2}$ is an entangled state. Lets go back to the interferometry shown in Fig. 1.1. From equation 1.3, the photon annihilation operators $\hat{a}_2$ and $\hat{b}_2$ before the substrate output state can be expressed by $\hat{a}_0$ and $\hat{b}_0$ as follows:

$$\hat{a}_0 = \frac{-1}{\sqrt{2}}\left(e^{-i\varphi}\hat{a}_2 + i\hat{b}_2\right),$$

$$\hat{b}_0 = \frac{1}{\sqrt{2}}\left(i\,e^{-i\varphi}\,\hat{a}_2 - \hat{b}_2\right), \tag{1.13}$$

and the nonclassical input state $|1, 1\rangle_{A,B}$ can be rewritten as

$$\begin{aligned}
|1, 1\rangle_{A,B} &= \hat{a}_0^\dagger \hat{b}_0^\dagger |0, 0\rangle_{A,B} \\
&= \frac{-1}{\sqrt{2}}\left(e^{i\varphi}\,\hat{a}_2^\dagger - i\,\hat{b}_2^\dagger\right)\frac{1}{\sqrt{2}}\left(-i\,e^{i\varphi}\,\hat{a}_2^\dagger - \hat{b}_2^\dagger\right)|0, 0\rangle \\
&= \left[\frac{i}{2}\left(e^{2i\varphi}\,\hat{a}_2^{\dagger 2} + \hat{b}_2^{\dagger 2}\right) + \frac{1}{2}\,e^{i\varphi}\left[\hat{a}_2^\dagger,\,\hat{b}_2^\dagger\right]\right]|0, 0\rangle \\
&= \frac{i}{2}\left(e^{2i\varphi}\,\hat{a}_2^{\dagger 2} + \hat{b}_2^{\dagger 2}\right)|0, 0\rangle \\
&= \frac{i}{\sqrt{2}}\left(e^{2i\varphi}\,|2, 0\rangle_{u,l} + |0, 2\rangle_{u,l}\right), \tag{1.14}
\end{aligned}$$

where the operators $\hat{a}_2$ and $\hat{b}_2$ commute with each other and the subscripts u and l mean the upper and lower paths, respectively. Equation 1.14 indicates that when two identical photons simultaneously enter a 50:50 beam splitter (one in each input

mode), both photons propagate either through the upper path or the lower path in the interferometer. It is a well known effect, referred to as the Hong-Ou-Mandel interference effect [71]. The entanglement is between photon number and path, and that is why it is called the path-entangled photon-number state. Since both photons pass through the phase shifter only on the upper path, they acquire twice the phase shift as with a single-photon process. Since the two paths are indistinguishable, the amplitudes corresponding to these two paths will interfere, and the two-fold phase shift will induce the doubling of the resolution.

Assume an optical light source having a superposition of N photons on the upper arm with no photon on the lower arm, and vice versa. The N photons on the only upper arm will experience the phase shift of $(N\varphi)$, and the path-entangled photon-number state of N photons will be given by

$$\frac{1}{\sqrt{2}} \left(e^{N i \varphi} \, | \, N, \, 0 \rangle_{\mathrm{u,l}} + | \, 0, \, N \rangle_{\mathrm{u,l}} \right). \tag{1.15}$$

The N-photon path-entangled photon-number state is referred to as the NOON state [72]. If the NOON state is prepared and the substrate is an N-photon absorbing material, then the recorded interference pattern may be computed as

$$
\begin{aligned}
R_{QL}(x) &\propto \langle \mathrm{NOON} | \hat{c}^{\dagger N} \, \hat{c}^N | \mathrm{NOON} \rangle / N! \\
&= \left| \frac{i}{2} \left(1 + e^{2i\varphi} \right) \right|^2 \langle 0, \, 0 | 0, \, 0 \rangle \\
&= \frac{1}{2} \left[1 + \cos(N\varphi) \right].
\end{aligned}
\tag{1.16}
$$

The minimum peak-to-peak feature size at the grazing angle will be $\lambda/2N$, so the resolution can be enhanced by a factor of N. Also, theoretically there is no limit for N and the visibility of the interference fringe is unity.

1.5 Quantum states induced by spontaneous parametric down conversion

Spontaneous parametric down-conversion (SPDC) is one of the most important second-order nonlinear process in quantum optics to generate a light source of the nonclassical state. A pump photon of higher frequency interacts with a non-centrosmmetric crystal and splits into two separate photons (generally referred to as signal and idler photons) of lower frequencies [1]. The birth time, the time at which the signal and idler are created in the nonlinear crystal, is extremely short, of the order of 100 fs [71]. The initial and final quantum-mechanical states of the crystal are left unchanged in the process, so energy must be conserved as shown in Fig. 1.4(a),

$$\omega_{\mathrm{p}} = \omega_{\mathrm{s}} + \omega_{\mathrm{i}}, \tag{1.17}$$

where ω is the angular frequency of the photon, and the subscripts p, s, and i refer to the pump, the signal, and the idler photon, respectively. Note that the signal and idler frequencies are anticorrelated with respect to each other about $\omega_{\mathrm{p}}/2$.
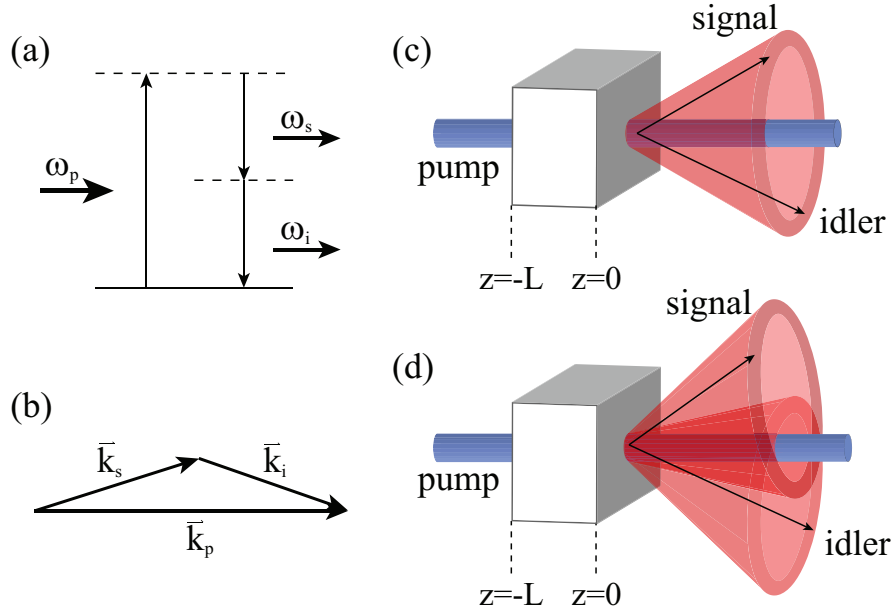
Figure 1.4: The spontaneous parametric down-conversion process. (a) energy diagram, (b) momentum diagram, (c) geometry of type-I SPDC, and (d) geometry of type-II SPDC.

In addition, the momentum conservation law of the form

$$\vec{k}_p = \vec{k}_s + \vec{k}_i, \tag{1.18}$$

must be met in this process as shown in Fig. 1.4(b). Here $\vec{k}$ is the wave vector of the photon. Since the nonlinear material has dispersion and birefringence, the momentum conservation law is only satisfied when the phase matching condition in nonlinear optics is fulfilled, and two types of SPDC exist depending on down-converted photons polarizations. The type-I SPDC process generates signal and idler photons sharing the same polarization, and the output geometry is shown in Fig. 1.4(c). At the detection plane, there exists a ring originated by signal and idler

photons. Meanwhile the type-II SPDC process creates two rings as shown in Fig. 1.4(d) at a detection plane, each ring is produced by either signal or idler photons having orthogonal polarizations to each other.

The forms $(|\,1,1\rangle)$ in equation 1.12 is the simplest expression of the quantum state from SPDC, but the photons generated by SPDC have a complicated multi-mode two-photon Fock-state. Consider a classical pump field in a nonlinear medium of a length of L in z-direction and the pump field has a cross section of a, so that the interaction volume is $\upsilon \equiv aL$ [73]. The origin is located at the center of the cross section and at the end of the interaction volume as shown in Fig. 1.4(c) & (d). The SPDC process is a three-wave mixing process having the medium polarization vector $\mathbf{P}^{(NL)}$ as follows:

$$\mathbf{P}_i^{(NL)}(\mathbf{r},t) = \int dt_1 dt_2 \chi_{ijk}^{(2)}(t-t_1, t-t_2) E_j(\mathbf{r}, t_1) E_k(\mathbf{r}, t_2), \qquad (1.19)$$

where $\chi^{(2)}{}_{ijk}$ is the second-order nonlinear susceptibility tensor, E is the electric field. The nonlinear interaction Hamiltonian of the electromagnetic system is given by

$$\begin{aligned}
\mathcal{H}_I &= \frac{1}{8\pi} \int_\upsilon d^3\mathbf{r} \, 4\pi \mathbf{P^{NL}} \cdot \mathbf{E} \\
&= \frac{1}{2} \int_\upsilon d^3\mathbf{r} \, E_i \int dt_1 dt_2 \chi_{ijk}^{(2)} E_j E_k \qquad (1.20)
\end{aligned}$$

Since electromagnetic field can be treated as an infinite set of harmonic oscillators, the field can be quantized and expressed as an operator $\hat{E}(\mathbf{r}, t)$.

The electric field operators consist of two components for positive and negative

frequencies, $\hat{\mathbf{E}}(\mathbf{r}, t) = \hat{\mathbf{E}}^{(-)}(\mathbf{r}, t) + \hat{\mathbf{E}}^{(+)}(\mathbf{r}, t)$ and the E-field operator with positive

frequency is given by

$$\hat{\mathbf{E}}^{(+)} = \frac{1}{\sqrt{2\pi}} \int d^3\mathbf{k} \sum_{\nu=1,2} \epsilon_{\mathbf{k},\nu} l(\omega) \hat{a}_{\mathbf{k},\nu} \exp[i(\mathbf{k} \cdot \mathbf{r} - \omega t)], \tag{1.21}$$

where $l(\omega) = i\sqrt{\hbar\omega/2c}$ and $\epsilon_{\mathbf{k},\nu}$ are the unit vectors for two independent polariza-

tions. $\hat{a}_{\mathbf{k},\nu}$ is the annihilation operator for the mode given by $\mathbf{k}, \nu$ and satisfies the

commutation relation:

$$[\hat{a}_{\mathbf{k},\nu}, \hat{a}^{\dagger}_{\mathbf{k}',\nu'}] = \delta_{\nu\nu'}\delta(\mathbf{k} - \mathbf{k}') \tag{1.22}$$

In real experiments, due to the material dispersion and the finite length of the crystal,

the phase matching condition is not perfect. Moreover, the angular frequency of the

pump photon (ω_{p}) is much larger than those of down-converted photons ($\omega_s \& \omega_i \sim$

$\omega_0 = \omega_p/2$). The corresponding nonlinear Hamiltonian operator using positive and

negative frequency components of the field operators is given by

$$\hat{\mathcal{H}}_I = \int_{[\omega_p]} d^3\mathbf{k}_3 \int_{[\omega_0]} d^3\mathbf{k}_1 d^3\mathbf{k}_2 \sum_{\nu_1,\nu_2,\nu_3} \chi^{(2)}_{ijk}(\omega_1, \omega_2, \omega_3)(\epsilon_{\mathbf{k}_3,\nu_3})_i (\epsilon_{\mathbf{k}_1,\nu_1})^*_j (\epsilon_{\mathbf{k}_2,\nu_2})^*_k$$
$$\times \hat{a}_{\mathbf{k}_3,\nu_3} \hat{a}^{\dagger}_{\mathbf{k}_1,\nu_1} \hat{a}^{\dagger}_{\mathbf{k}_2,\nu_2} e^{i(\omega_1+\omega_2-\omega_3)t} \int_v d^3\mathbf{r} \exp(i\Delta\mathbf{k} \cdot \mathbf{r}) + H.\,c., \tag{1.23}$$

where $H.\,c.$ stands for the Hermitian conjugate, $\chi^{(2)}_{ijk}(\omega_1, \omega_2, \omega_3)$ is the second-order

nonlinear susceptibility tensor in the frequency domain, and the phase mismatch is

given by

$$\Delta \mathbf{k} \equiv \mathbf{k}_3 - \mathbf{k}_1 - \mathbf{k}_2. \tag{1.24}$$

Normally, the second-order nonlinear susceptibility is a slowly varying function.

Next, the state of the system at time t is related to the state at time t' by

$$|\Psi(t)\rangle = \hat{U}(t, t')|\Psi(t')\rangle, \tag{1.25}$$

where the unitary operator is defined and expanded as

$$\hat{U}(t, t') = \exp \left[\frac{1}{i\hbar} \int_{t'}^{t} \hat{\mathcal{H}}_I(\tau) \, d\tau \right]$$

$$\approx 1 + \frac{1}{i\hbar} \int_{t'}^{t} \hat{\mathcal{H}}_I(\tau) \, d\tau + \frac{1}{2!} \left[\frac{1}{i\hbar} \int_{t'}^{t} \hat{\mathcal{H}}_I(\tau) \, d\tau \right]^2 \ldots. \tag{1.26}$$

Substituting equation 1.23 into the above equation, we obtain a complicated expression, but it can be simplified under several assumptions. If the pump field is a continuous wave, we can treat $t' = -\infty$ and $t = \infty$ and the time integral of the exponential term in equation 1.23 becomes

$$\int_{-\infty}^{\infty} d\tau e^{i(\omega_1 + \omega_2 - \omega_3)\tau} = 2\pi \delta(\omega_3 - \omega_1 - \omega_2) \tag{1.27}$$

The Hermitian conjugate term in equation 1.23 describes an opposite process of

SPDC, so we can drop this term. In addition, the photon polarizations are determined by the phase matching condition of the nonlinear crystal, so we can ignore the summation over ν's. In this thesis, we are interested in the collinear phase matching condition in which the directions of the down-converted photons are same. In the collinear phase matching condition, we can treat the process as a one-dimensional case, and then the time integral of the Hamiltonian operator in equation 1.23 can be rewritten as

$$\frac{1}{i\hbar}\int_{-\infty}^{\infty}\hat{\mathcal{H}}_I(\tau)d\tau = \xi\int_{[\omega_p]}d\omega_3\int_{[\omega_0]}d\omega_1 d\omega_2\delta(\omega_1+\omega_2-\omega_3)$$
$$\times\hat{a}_p(\omega_3)\hat{a}_s^{\dagger}(\omega_1)\hat{a}_i^{\dagger}(\omega_2)\Phi(\omega_1,\omega_2)h(L\Delta k), \quad (1.28)$$

where

$$h(Lx) = \int_{-L}^{0}dz\,e^{ixz} = \frac{1-e^{-iLx}}{iLx} = e^{-iLx/2}\operatorname{sinc}(Lx/2), \quad (1.29)$$

with L is the length of the nonlinear crystal and ξ is a constant showing how strong the nonlinear effect is. Note that the nonlinear interaction Hamiltonian operator consists of an annihilation operator of the pump field and two creation operators of the signal and idler photons illustrating the SPDC process as shown in Fig. 1.4(a).

The initial state $(|\alpha(\omega),0,0\rangle_{\mathrm{p,s,i}})$ is a multi-mode coherent state at the pump field frequency and all the other modes in vacuum. The subscriptions p, s, and i stand for the pump, signal, and idler modes, respectively. The pump field is so strong that we

assume that it does not deplete while the SPDC process, and we only care about the signal and idler photons. Then the initial state becomes

$$|\Psi_0\rangle = |\,0,\,0\rangle_{\text{s,i}}.$$ (1.30)

Substituting equations 1.26, 1.28, and 1.30 into equation 1.25, we obtain the final photon state generated by SPDC as follows:

$$|\Psi\rangle_{\text{SPDC}} \approx |\,0,0\rangle + \eta \int d\omega_1 d\omega_2 \delta(\omega_1 + \omega_2 - \omega_p) h(L\Delta k)|\omega_{1s}, \omega_{2i}\rangle$$

$$+\eta^2/2 \int d\omega_1 d\omega_2 d\omega_1' d\omega_2' \delta(\omega_1 + \omega_2 - \omega_p)\delta(\omega_1' + \omega_2' - \omega_p)$$

$$\times h(L\Delta k) h(L\Delta k')|\omega_{1s}, \omega_{1's}, \omega_{2i}, \omega_{2'i}\rangle,$$ (1.31)

where $\eta = \alpha_{\text{p}} * \xi$ is the amplitude of generating photon pair at a given pump power with α_{p} is the pump-field strength. The second and third terms are the two- and four-photon states. This photon state can be simplified by assuming a very large and long crystal and single-mode description as follows:

$$|\Psi\rangle_{\text{SPDC}} \approx |\,0,0\rangle_{s,i} + \eta|1,1\rangle_{s,i} + \frac{\eta^2}{2}|2,2\rangle_{s,i},$$ (1.32)

Note that the two-photon state is proportional to η and the four-photon state is $\eta^2/2$. At a low pump power ($\eta \ll 1$), the four-photon and higher photon-number states can be neglected.

1.6   Slow- and fast-light pulse propagation

When monochromatic light propagates through a material, its speed, v changes and becomes slower than the vacuum speed, c. The ratio between the vacuum speed and the speed of light in a dispersive medium is referred to as the refractive index of the material. The phase velocity of a monochromatic wave in a dispersive medium is defined as the velocity of points of constant phase in the form of $v = \omega/k = c/n$, where k is the wavenumber and n is the refractive index. Since the refractive index is a function of frequency of light, if the field is not a monochromatic wave (e.g. a pulse), different frequency components of the field will experience a different value of the refractive index. Due to the dispersion of the material, the group velocity is defined as

$$v_{\mathrm{g}} = \frac{d\omega}{dk} = c/n_{\mathrm{g}}, \qquad (1.33)$$

where n_{g} is the group refractive index at a frequency of ω_0 in the form of

$$n_{\mathrm{g}}(\omega_0) = c\frac{dk}{d\omega}|_{\omega_0} = n(\omega_0) + \omega_0\frac{dn(\omega_0)}{d\omega}. \qquad (1.34)$$

In general, the group velocity will be slightly different from the phase velocity since the second term of equation 1.34 has a small value. Near an optical resonance, however, the group index becomes significant. Fig. 1.5(a) shows an absorption spectrum near a spectral hole. According to the Kramers-Kronig relations [1], the imaginary
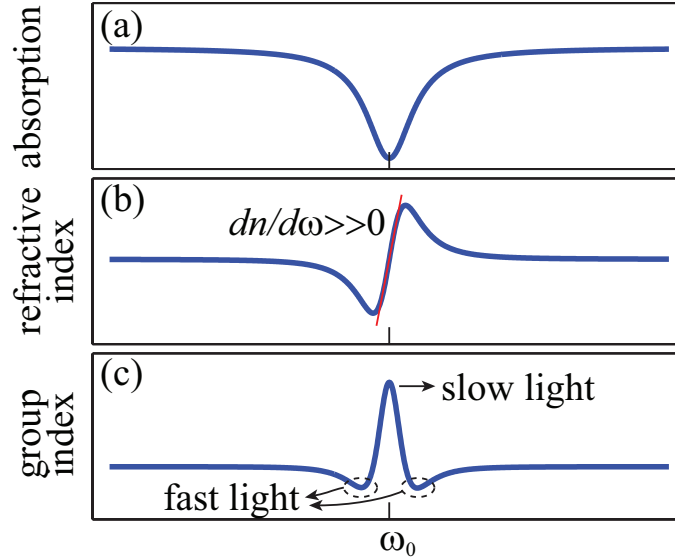
Figure 1.5: (a) A spectral hole, (b) the refractive index, and (c) the group index at near the center frequency ω_0.

part (absorption) and the real part of the refractive index of a material are related to each other. Therefore, near the spectral hole, the refractive index of the material also changes in a very narrow frequency range as shown in Fig. 1.5(b) producing large normal dispersion $(dn/d\omega \gg 0)$. Finally, a narrow dip in an absorption spectrum will induce huge group index at the center frequency of ω_0 and small or even negative group index on both sides of the resonance as illustrated in Fig. 1.5(c). In addition, a narrow peak in an absorption spectrum will produce small group index leading to fast-light propagation effects at near ω_0 and slow-light effects on both sides of the resonance. Therefore, a strong but narrow spectral feature is required to have slow (or fast) light pulse propagation effects.

One interesting topic of slow- and fast-light effects is whether the group velocity is equal to the information velocity [74, 75, 76]. The information arrival time

can be defined as the earliest possible moment at which one can observe a non-zero value in the electromagnetic field that propagates through a system. In our group, the information velocity has been studied using the propagation of a pulse with an abrupt change in pulse amplitude as shown in Fig. 1.6 [77]. The leading edge of the input pulse is Gaussian, but at the peak, the intensity rapidly drops to zero. Two solid-state optical materials, alexandrite and ruby, are used to induce superluminal or very small group velocity by coherent population oscillations, respectively. As shown in Fig. 1.6, the smoothly varying portions of the pulse propagate at the group veloc-
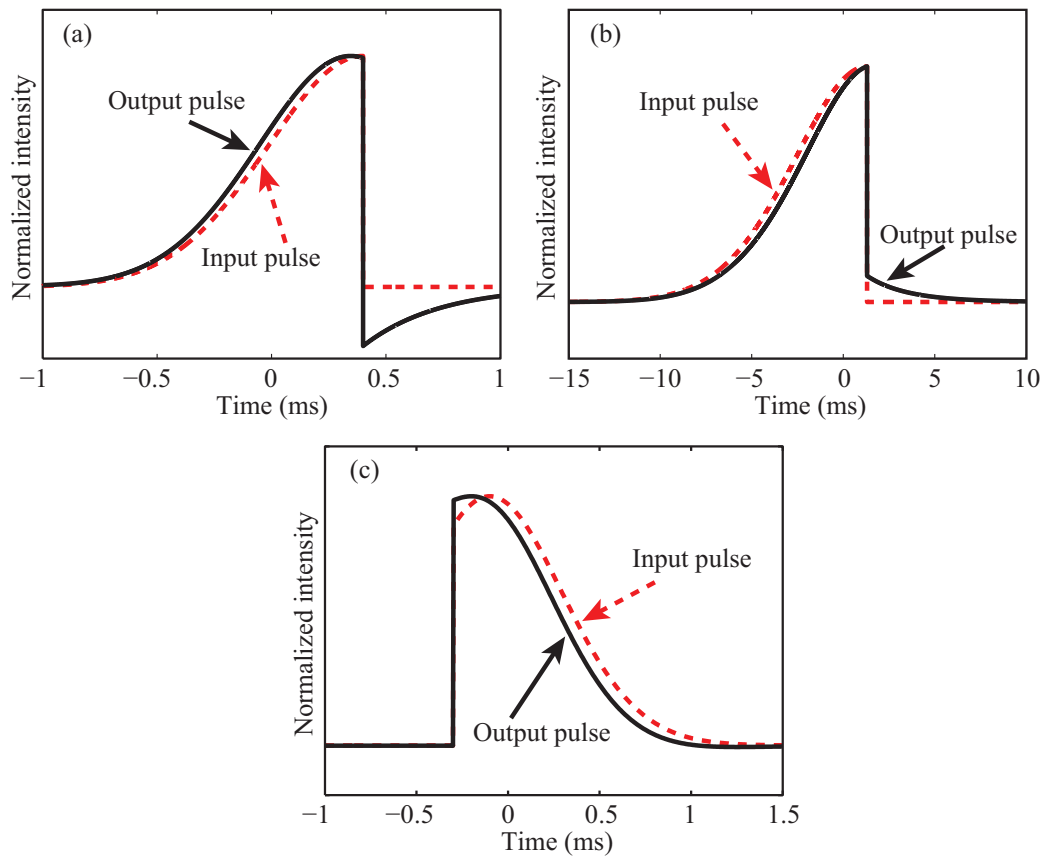
Figure 1.6: Calculated input and normalized output intensities of a truncated Gaussian pulse after propagation through (a) alexandrite and (b) ruby.

ity, but information (discontinuity) was neither advanced nor delayed indicating the information velocity is equal to the phase velocity, not the group velocity.

Another interesting topic in the fast-light effects is whether the superluminal propagation violates causality. The superluminal pulse propagation indicates that the peak of the output pulse exits the dispersive medium before the peak of the input pulse enters. This superluminal pulse propagation is caused by a negative value of the group velocity. In Fig. 1.6(c), the nature of discontinuity propagation explains why there is no violation of causality even with the superluminal pulse propagation. The peak of a pulse is advanced in time showing the fast-light effect, but there is no change before the discontinuity. Therefore, we can conclude that superluminal effects are initiated by the leading edge of the pulse.

Furthermore, theory predicts an interesting behavior of the superluminal pulse propagation inside of the medium. During the superluminal pulse propagation, a pulse will appear to propagate in the backward direction within the medium. This nature of backward pulse propagation has been investigated in our group [78], and the backward pulse propagation within the medium has been experimentally observed in an erbium doped fiber amplifier by successively cutting back the length of the fiber. In Fig. 1.7, the superluminal pulse propagation is illustrated by two arrows representing the input and output pulse-peak positions, and inside the fiber another arrow moves backwards in time. Further investigation was performed to determine the energy flow direction in the medium with a negative group index, and showed that energy

transport is always in the forward direction even if the peak of a pulse inside the medium travels backward.

In the following two sections, I study coherent population oscillations as a mechanism of slow- and fast-light effect and describe an experimental observation of slow- and fast-light propagation in erbium-doped optical fiber.
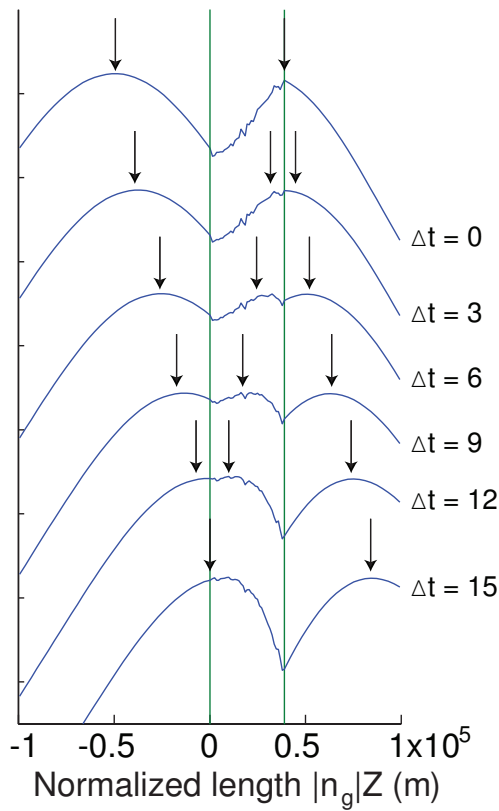
Figure 1.7: Experimentally observed time evolution of the pulse as it propagates through the fiber.

1.7 Coherent population oscillation

Room-temperature solid-state slow- and fast-light systems have been developed [38, 39, 41, 42, 43, 44, 45] and in many ways they are practically suitable for use in applications. The mechanism investigated in this thesis is coherent population oscillations (CPO). Spectral holes due to wave interactions in saturable absorbers were first predicted in 1967 by Schwartz and Tan [79] and experimentally observed by Hillman *et al*. in ruby [80]. The first experimental demonstration of slow- and fast-light effects by CPO was performed in ruby and alexandrite [38, 39]. The slow- and fast-light propagation speeds based on the process of CPO have some specific properties compared to other mechanisms as follows: the occurrence in room-temperature solid-state systems, very wide range of resonance, and no dependence on laser linewidth [81].

CPO results in slow-light propagation for the following reason. A strong pump field and a signal field of slightly different frequencies can excite population from the ground state to the excited broad absorption band as shown in Fig. 1.8. Population decays from the excited state to the metastable level within a very short time and then returns to the ground state with a transition rate of $1/T_1$. The excited state has very short life time, but the meta stable state has relatively long lifetime. Due to the frequency difference, the pump and signal fields will interact, causing the population of the ground state to oscillate in time at the beat frequency ($\omega_\pm$) of the two fields. This oscillation occurs only when the beat frequency is less than the transition rate ($1/T_1 > \omega_\pm$). Due to the oscillating population, the signal field will
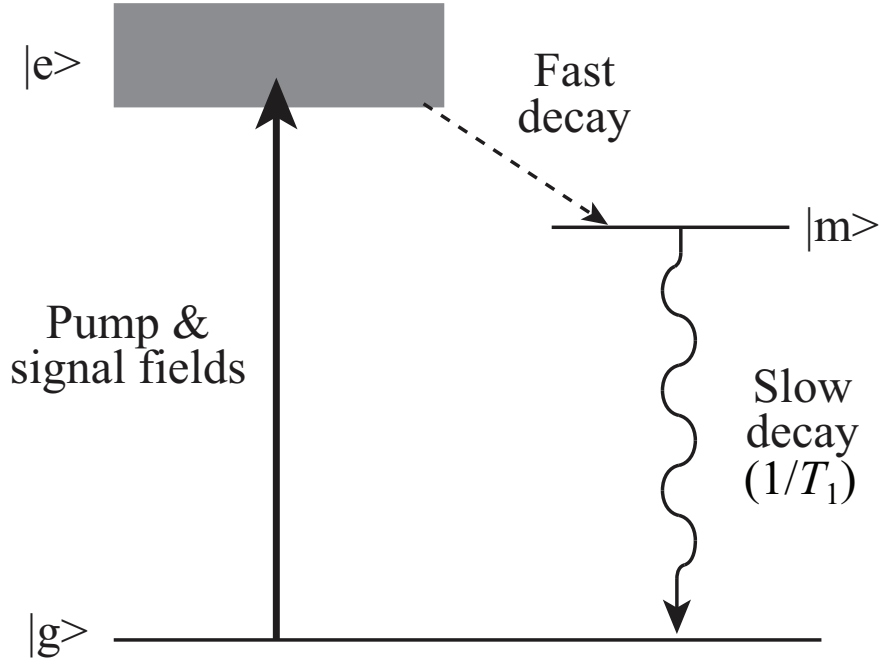
Figure 1.8: Energy levels of saturable absorber.

experience reduced absorption within a narrow range, and an absorption spectral hole is centered at the laser frequency as shown in Fig. 1.5(a). Therefore, coherent population oscillation produces large group refractive index. Similarly, a gain spectral hole or absorption spectral antihole can be respectively created in a saturable gain medium or reverse saturable absorption medium, inducing fast or even superluminal pulse propagation.

Assume that the intensity of the incident light is modulated with a modulation frequency of $\triangle$. Due to no dependence on laser linewidth, the CPO effect reacts only to intensity variation of the incident light. A mathematical description of CPO in frequency domain leads to absorption coefficients of the unmodulated and modulated components of the input intensity [81]. The absorption coefficient of the unmodulated

intensity, α_0 is given by

$$\alpha_0 = \frac{\alpha_{\text{lin}}}{1 + I_0/I_{\text{sat}}}, \tag{1.35}$$

where α_{lin} is the linear unsaturated absorption coefficient, and $I_{\text{sat}} = \hbar\omega/(\sigma T_1)$ is the saturation intensity of the material. The absorption coefficient of the unmodulated intensity has the common property of saturable absorber. Meanwhile, the modulated component at a modulation frequency of $\triangle$ has its absorption coefficient, α_1 as

$$\alpha_1(\triangle) = \alpha_0 - \alpha_{\text{lin}} \left(\frac{I_0/I_{\text{sat}}}{1 + I_0/I_{\text{sat}}} \right) \left(\frac{1 + I_0/I_{\text{sat}}}{(1 + I_0/I_{\text{sat}})^2 + (\triangle T_1)^2} \right), \tag{1.36}$$

where $\triangle$ is the modulation frequency of the input intensity. It will show a spectral hole on the very wide background absorption versus the modulation frequency as shown in Fig. 1.5(a). In addition, the modulated component will experience the nonlinear refractive index, n_1 as

$$n_1(\triangle) = 1 + \frac{\alpha_{\text{lin}}c}{2\omega_{\text{c}}} \left(\frac{I_0/I_{\text{sat}}}{1 + I_0/I_{\text{sat}}} \right) \left(\frac{\triangle T_1}{(1 + I_0/I_{\text{sat}})^2 + (\triangle T_1)^2} \right), \tag{1.37}$$

where ω_{c} is the center frequency of the incident light. Fig. 1.5(b) illustrates the refractive index of the signal field versus the modulation frequency. Using the expression of the nonlinear refractive index, the group refractive index of the signal field

versus the modulation frequency is given by

$$n_{\text{g}}(\triangle) = n_1(\omega_{\text{c}}) + \frac{\alpha_{\text{lin}}c}{2}\left(\frac{I_0/I_{\text{sat}}}{1 + I_0/I_{\text{sat}}}\right)\left(\frac{T_1}{(1 + I_0/I_{\text{sat}})^2 + (\triangle T_1)^2}\right), \qquad (1.38)$$

and is illustrated in Fig. 1.5(c). The spectral hole due to coherent population oscillations causes large group index at near the center wavelength of the input laser beam.

1.8 Slow- and fast-light pulse propagation in an erbium doped fiber amplifier

In the previous two sections, we studied slow- and fast-light effects and coherent population oscillations as a mechanism of the effects. In this section, we describe experimental observation of slow and superluminal pulse propagation through an erbium doped fiber amplifier (EDFA) by means of coherent population oscillations. The EDFA was first demonstrated for use of a single-mode fiber laser source in 1986 [82]. The core of an EDFA is doped with erbium ions, and the population inversion of the ions can be induced by a pump field at a wavelength of 980 nm or 1480 nm, exhibiting gain in C-band (1530 - 1565 nm). It is well known that an erbium doped fiber is a saturable absorber at no pump power and becomes an amplifier with saturable gain at high pump powers.

Slow and superluminal pulse propagation through an EDFA was first observed
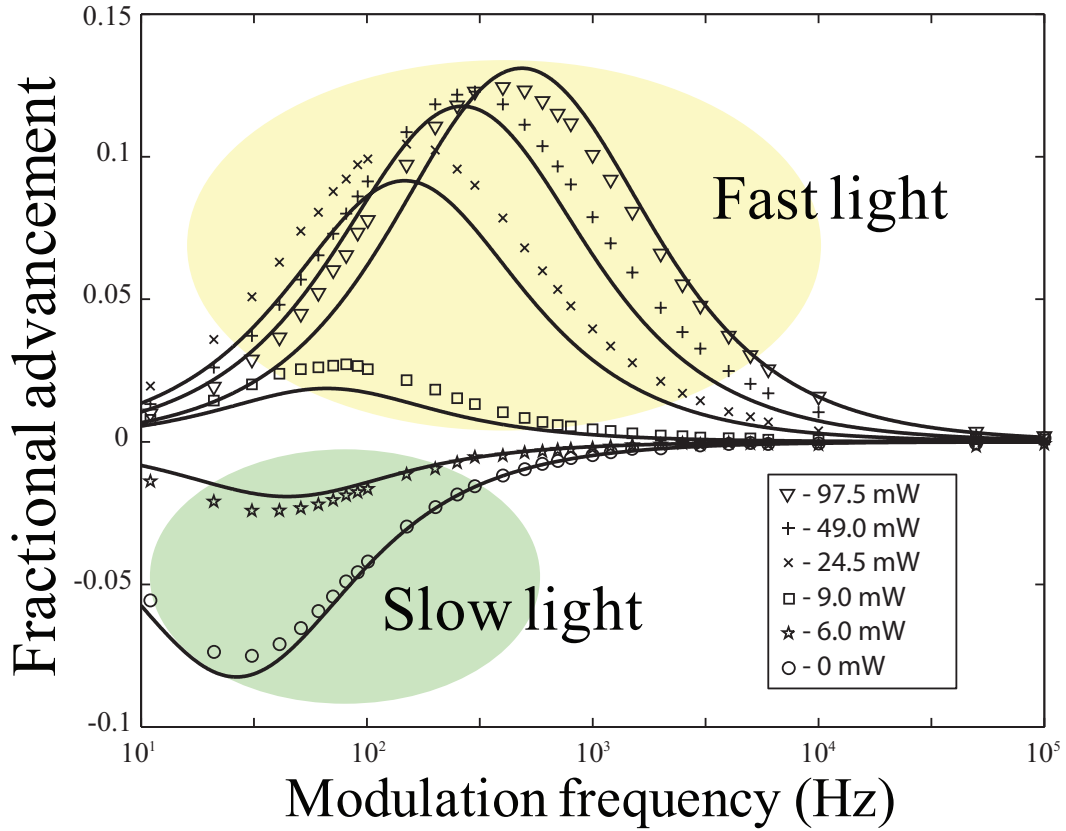
Figure 1.9: Experimentally measured (symbols) and numerically calculated (solid lines) fractional advancement for various pump powers vs. the modulation frequency of the signal.

in our group [40]. A sinusoidally modulated signal at 1550 nm was sent through an EDFA for various 980-nm pump powers. The degree of signal delay or advancement versus the modulation frequency is shown in Fig. 1.9, and the effect is tunable from one regime to the other by varying the pump power. At low pump power, the signal experiences large group index, but negative group index at high pump power. The controllable slow- and fast-light pulse propagation could have important implications for applications in photonics.

1.9 Summary

In this chapter, I have reviewed the basics of interference described by quantum mechanics. The spatial patterns of classical standard interference, classical nonlinear interference, and quantum interference are studied and compared to each other. I have discussed the quantum states generated by a nonlinear optical process of spontaneous parametric down-conversion producing two photons and four photons, simultaneously. I have also discussed some of the key concepts of slow- and fast-light pulse propagation effects, and studied how the coherent population oscillation process induces slow- and fast-light effects and explained the first experimental demonstration of the controllable slow- and fast-light effect in an EDFA.

In the next two chapters, I present our studies of the spatial interferometric super-resolution due to the nonlinear and quantum methods and fast-light pulse-distortion management in an erbium doped fiber amplifier. In Chapter 2, I study the nonlinear optical phase-shifted grating method and the details of multi-photon absorption. The experimental demonstration of the phase-shifted grating method was performed using a real N-photon absorbing lithographic recording material to achieve two- and three-fold enhancement of spatial resolution. I also investigate a way to generate non-sinusoidal patterns by the phase-shifted grating method. In Chapter 3, I describe the theory of the quantum optical centroid measurement method and experimentally demonstrate this new method. I then compare it with the traditional quantum lithography method that responds by means of multi-photon absorption. The optical

centroid measurement method shows spatial resolution enhancement as much as the quantum lithography method, but with much higher detection efficiency.

In Chapter 4, a new method for fast-light pulse-distortion management is described. Anomalous dispersion produced by coherent population oscillations can induce fast-light pulse propagation and also pulse distortion. By adding the proper amount of a constant background field, pulse-shape distortion will be minimized, and this technique is successfully demonstrated under various experimental conditions. The numerical calculations are performed, and the results are well matched with the experimental results. Chapter 5 presents the general conclusions.

Chapter 2

Nonlinear method for superresolution

2.1 Introduction

In standard linear interferometric lithography, the interference fringes have the form $I = 1 + \cos(Kx)$, where $K = 4\pi \sin\theta/\lambda$, θ is the angle of incidence and λ is the wavelength of light. Thus, the highest resolution pattern that can be recorded has a period of $\lambda/2$ at grazing incidence $\theta \to \pi/2$. This is called the Rayleigh limit[9, 15]. Several proposals have been suggested to achieve an N-fold resolution enhancement over the classical diffraction limit by using lithographic materials that work via N-photon absorption [17, 18, 19, 4, 21, 22, 23, 24, 25, 14]. In particular, Bentley and Boyd proposed the phase-shifted grating method and demonstrated that an M-fold

enhancement in resolution can be achieved by exposing an N-photon absorber M times and adjusting the phase difference between the two recording beams after each exposure [21, 22]. In their experiment, an N-photon absorbing medium was simulated by Nth harmonic generation followed by a CCD camera.

In the present chapter, the phase-shifted grating method is further studied for verifying the possibility of superresolution. This method was originally proposed by Ooki in 1994 [17], and improved by Bentley [21]. In the first proposal of Ooki *et. al.*, they considered N exposures of light on a N-photon absorbing material with equal amount of phase shift between exposures. Unlike the multiple exposure method of Ooki, however, the number of exposures M is allowed to be different from the number of photons N needed for multi-photon absorption in the way of Bentley *et. al.*. The advantage of Bentley's proposal is that the visibility can be high, approaching unity for $N \gg M$.

This chapter is organized as follows. In Section 2.2, the theory of the phase-shifted grating method is reviewed. An experimental demonstration is performed using poly(methyl-methacrylate) (PMMA), and optical properties of PMMA is given in Section 2.3. PMMA is a UV lithographic material, but, in our research, it is considered as a multi-photon absorbing lithographic material at the wavelength of 800 nm. Sections 2.4 present experimental details. In Section 2.5, we report an experimental result showing a recorded fringe pattern with resolution beyond the diffraction limit at grazing angle. Section 2.6 presents additional experimental results of three-fold

enhanced resolution with reduced incidence angle and non-sinusoidal patterns with this technique. The summary is given in Section 2.7. The work described in this chapter has been published in Journal of Modern Optics [83].

2.2 Theory

A schematic of this technique is illustrated in Fig. 2.1. The two recording beams are brought together on an N-photon absorber and interference fringes are formed. Note that the interference pattern recorded by a N-photon absorbing material after a single exposure is given by

$$I_1^N = I[1 + \cos(Kx + \phi_{\text{arb}})]^N, \tag{2.1}$$

where I is the intensity of the recording beams for an exposure, $K = 4\pi \sin\theta/\lambda$ is the wavevector of the incidence light, and ϕ_{arb} is an arbitrary phase of a fixed value. This pattern has the same spatial period as a classical standard interference pattern, but with sharpened features. In one arm of the interferometer, we inserted a phase-shifter which is used to adjust the phase difference between the two recording beams of light. We then expose the PMMA M-times with the relative phase of successive laser pulses incremented by a fixed amount. For instance, when the optical path-length difference between the two arms changes by λ/M after each exposure, the phase of the jth laser
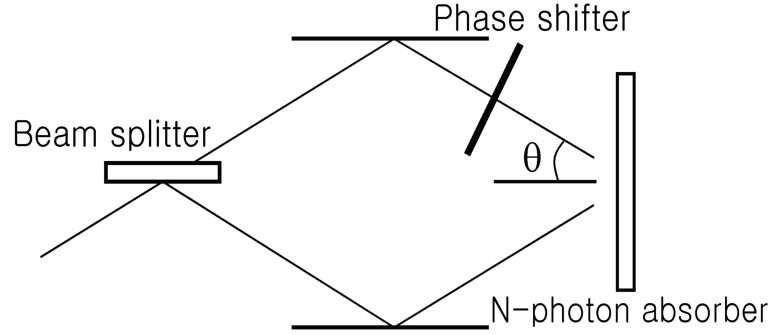
Figure 2.1: Schematic representation of the method.

pulse is given by [21]

$$\triangle\phi_j = \frac{2\pi j}{M}. \hspace{3cm} (j = 1, 2, \ldots, M) \hspace{2cm} (2.2)$$

In this case, the interference pattern recorded on the N-photon absorbing material after exposing it using M shots with progressively increasing phase shifts is given by

$$\sum_{m=1}^{M} I_m^N = \sum_{m=1}^{M} I_m[1 + \cos(Kx + 2\pi m/M + \phi_{\mathrm{arb}})]^N, \hspace{2cm} (2.3)$$

where I_m is the intensity of the recording beams for the mth exposure. Thus, we record an interference pattern with a fringe period of $\lambda/(2M\sin\theta)$, where θ is the incidence angle of the recording beams. For example, if one uses a 3-photon absorber (N=3) and two exposures (M=2) with equal intensity for each exposure, where the second exposure is shifted as described above, the resulting intensity pattern on the
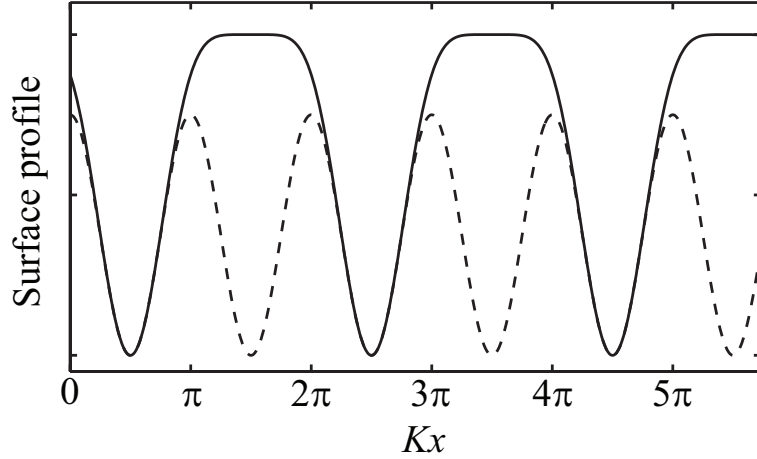
Figure 2.2: Theoretical surface profile for various experimental parameters. Solid curve is for $N=3$, $M=1$; dotted curve is for $N=3$, $M=2$.

3-photon absorber is given by

$$
\begin{aligned}
I_1^3 + I_2^3 &= (1 + \cos Kx)^3 + [1 + \cos(Kx + \pi)]^3 \\
&= 4 + 3\cos(2Kx) \\
&= 4[1 + V\cos(2Kx)], \tag{2.4}
\end{aligned}
$$

where $V = (I_{\max} - I_{\min})/(I_{\max} + I_{\min}) = 3/4$ is the visibility of the fringes. $I_{\max}$ and $I_{\min}$ are the maximum and minimum values of the interference patterns. In Fig. 2.2, we plot the theoretical surface profile calculated from Eq. (2) under the assumption that the surface profile varies linearly with the exposure pattern. Note that this method reduces the fringe period by a factor of two, although the visibility is also reduced.

The pattern's resolution is enhanced by a factor of M compared to normal inter-

Table 2.1: Visibility as a function of resolution and absorption process.

Number of exposures (M)	Order of absorption (N)	Visibility (V)
2	2	33%
2	3	60%
2	6	94%
2	8	98%
3	3	10%
3	6	48%
3	8	67%
3	17	97%
4	4	3%
4	6	14%
4	8	28%
4	30	97%

ferometric lithography. A high visibility fringe pattern can be achieved for the case where the value of N is chosen to be much larger than that of M. To see this, the visibilities for various combinations of N and M are calculated and summarized in Table 2.1 [21].

Moreover, if one does not use uniform phase shifts between exposures, then non-sinusoidal patterns can also be formed. Let us assume that the lithographic material is a 3-photon absorber and is exposed twice with a $\pi + \Delta$ phase shift on the second exposure, where Δ is a small phase deviation. Using Eq. (1) we calculate the fringe pattern and compare it to the uniformly phase-shifted result. The results are presented in Fig. 2.3(a). The dashed curve shows the interference pattern for N=3 and M=2 with the phase shift of the second shot given by $\pi + \Delta(\Delta = \pi/3)$. The solid curve shows the pattern for N=3 and M=2, where the phase shift of the second shot is π. This figure shows that the various combinations of the phase shifts be-
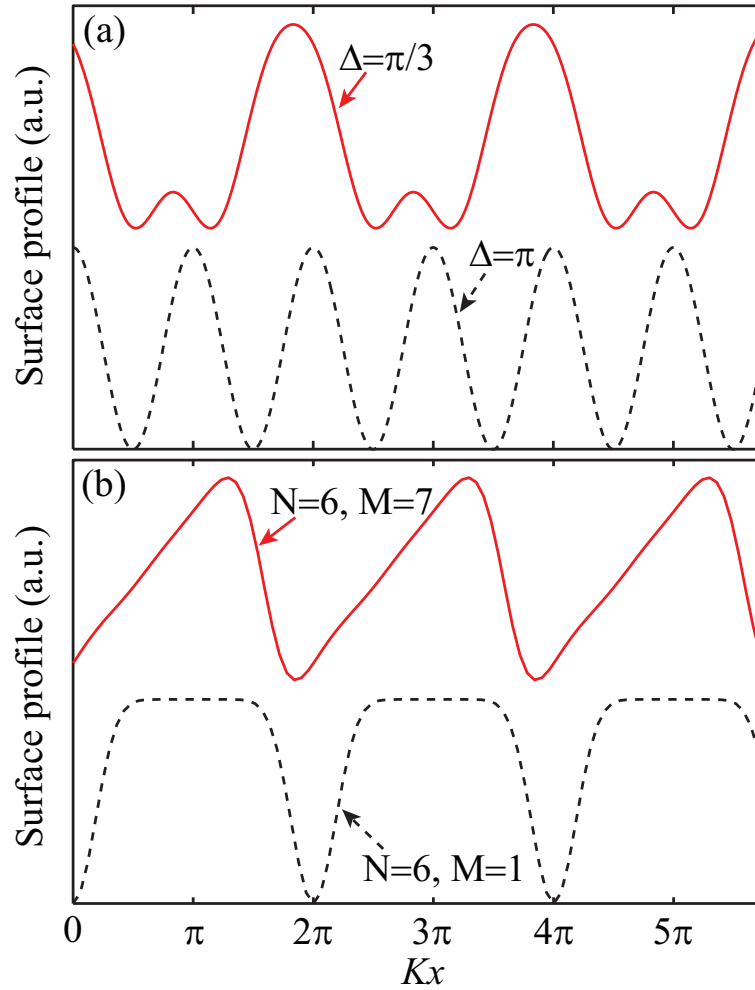
Figure 2.3: Theoretical surface profile for non-sinusoidal fringe patterns.

tween the two arms can cause various non-sinusoidal patterns. Furthermore, the field

amplitude of each exposure is an additional free parameter for varying the shape of

interference patterns. If each exposure has different energy $(I_i \neq I_j)$ with control-

lable phase shift, arbitrary patterns can also be obtained. For instance, Fig. 2.3(b)

illustrates interference patterns recorded on a six-photon absorber for two different

exposure conditions. The dashed curve is the recorded interference pattern for $N=6$

and $M=1$. The solid curve shows the pattern for $N=6$ and $M=7$. The normalized in-
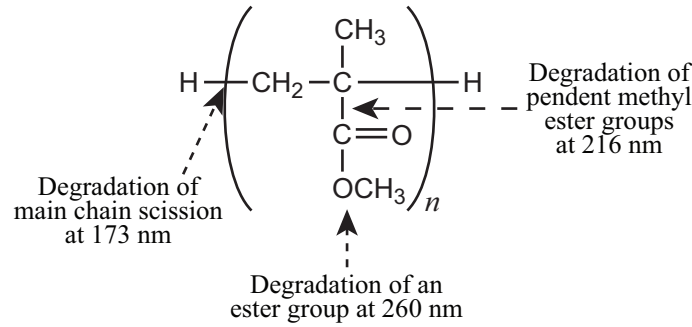
Figure 2.4: Chemical structure of PMMA.

tensities for multiple exposures are $I_1 = 1$, $I_2 = 0.76$, $I_3 = 0.61$, $I_4 = 0.52$, $I_5 = 0.36$, $I_6 = 0.25$, and $I_7 = 0.1$. The phase shifts for multiple shots are $D_1 = 0$, $D_2 = \pi/4$, $D_3 = \pi/2$, $D_4 = 3\pi/4$, $D_5 = \pi$, $D_6 = 5\pi/4$, $D_7 = 3\pi/2$.

2.3   Optical properties of PMMA

Poly(methyl methacrylate) is a lightweight material with a density of 1.17~1.20 g/cm^3, often called acrylic glass. It also has good impact strength, higher than both glass and polystyrene. Its molecular formula is $(C_5O_2H_8)_n$, and its chemical structure is illustrated in Fig. 2.4. PMMA is a transparent plastic transmitting visible light and infrared light (300 nm - 2800 nm) and reflecting about 4% of incident light from each of its surfaces on account of its refractive index (1.49 at 587.6 nm [84]). It has strong absorption in the ultraviolet region near 216 nm and 260 nm as shown in Fig. 2.5. The absorption peak at 216 nm with FWHM of 26 nm of is caused by the absorption band of pendent meyhyl ester groups which consists of two bonds (C-CO and OC-O bonds) [85], and another higher absorption peak (roughly 7 times
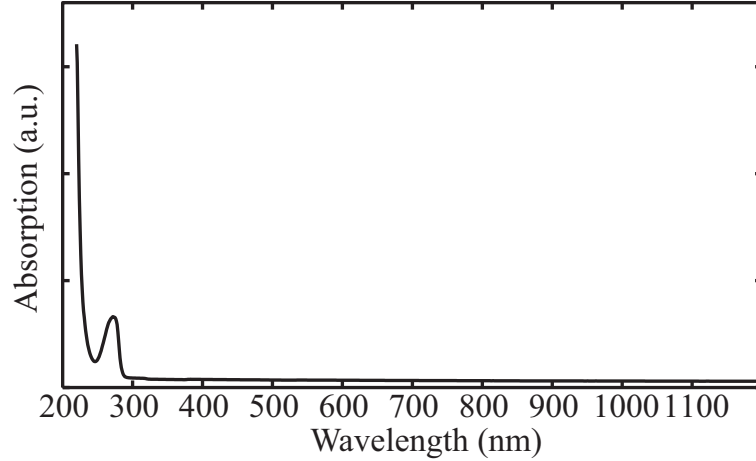
Figure 2.5: The UV absorption spectrum of the PMMA film.

stronger) at 173 nm with FWHM of 14 nm is induced by the absorption band of the main chain scission (C-CH$_2$ bond) [86]. In addition, weakly absorbed photons ($\sim$100 times less) at around 260 nm results in the degradation of an ester group (O-CH$_3$ bond) [87]. With a strong intensity of light at a wavelength of 800 nm, three- or four-photon absorption can occur and break one of PMMA's chemical bonds in Fig. 2.4. The broken bonds can be removed later by developing process.

2.4 Experimental details

The sample film was prepared as follows. PMMA (Molecular weight $\sim$ 120,000, Aldrich) was dissolved in toluene (Fisher Scientific) at 20 wt% and was spin-coated on a glass substrate with a spin speed of 1000 rpm for 20 seconds. The film was dried on a hotplate for 3 minutes. To fabricate a thicker film, we spin-coated the sample again on top of the first coat of film and dried it. The absorption spectrum of the
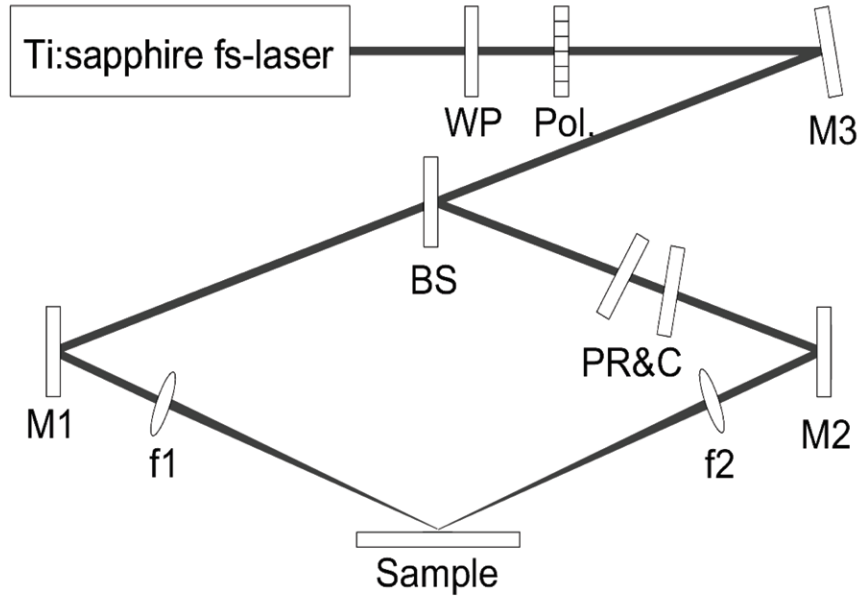
Figure 2.6: Experimental set-up.

PMMA film was measured to confirm its linear absorption properties. The spectrum

is shown in Fig. 2.5. The PMMA film is transparent throughout the visible region

down to a wavelength of 250 nm. Thus, light at a wavelength of 800 nm will not

experience linear absorption through the PMMA film. A high intensity pulse with

a wavelength of 800 nm, however, will induce three- or four-photon absorption. In

our experiment, we use an 800-nm Ti:sapphire mode-locked laser with regenerative

amplification (120 fs, Spectra-Physics) for the light source.

We interfered beams at an angle of incidence of $\theta = 70°$, which is close to grazing

angle limit, $\theta \to \pi/2$. Hence, the fundamental period of the fringes is 425 nm. The

experimental set-up is shown in Fig. 2.6, where 'WP' indicates a half-wave plate,

'Pol' a polarizer, 'BS' a 50:50 non-polarizing beam splitter, and 'M1', 'M2', & 'M3'

mirrors. To introduce a phase-shift between the two arms, we use a glass plate that

can be rotated. A second glass plate is used to compensate for the lateral beam displacement caused by the first plate (PR & C : phase retarder and compensator). The focal lengths of two lenses (f1 and f2) are both 50 cm. After each exposure, we observed the diffraction pattern of a green diode laser incident on the exposed area (Beam of Light Technologies, $\lambda = 532$ nm, ~ 5mW).

After irradiating the sample, we put it in the developer, 1:1 MIBK (MicroChem Corp.) for 10 seconds and rinsed it in deionized water for 30 sec. After development, we used an atomic force microscope (AFM) to confirm the fringe pattern recorded onto the surface of the film.

2.5 Results

In our first experiment, experimental dosimetry was performed to verify the multi-photon nature of absorption in PMMA. First, the green laser light was illuminated at normal incidence on a spot of a PMMA film. Then we irradiated the sample at the same spot interfering two beams of 800-nm re-amplified pulses until a diffracted beam at 532 nm was observed. The number of pulses exposed on the sample was counted using a pulse counter. We repeated the measurement for various recording pulse energies, and the dosage energy was calculated by multiplying the number of exposed pulses by the pulse energy. Fig. 2.7 shows the average amount of energy needed to write a grating versus the pulse peak power of the recording beams on a log-log scale. The uncertainty of the measurement was quantified in terms of standard deviations,
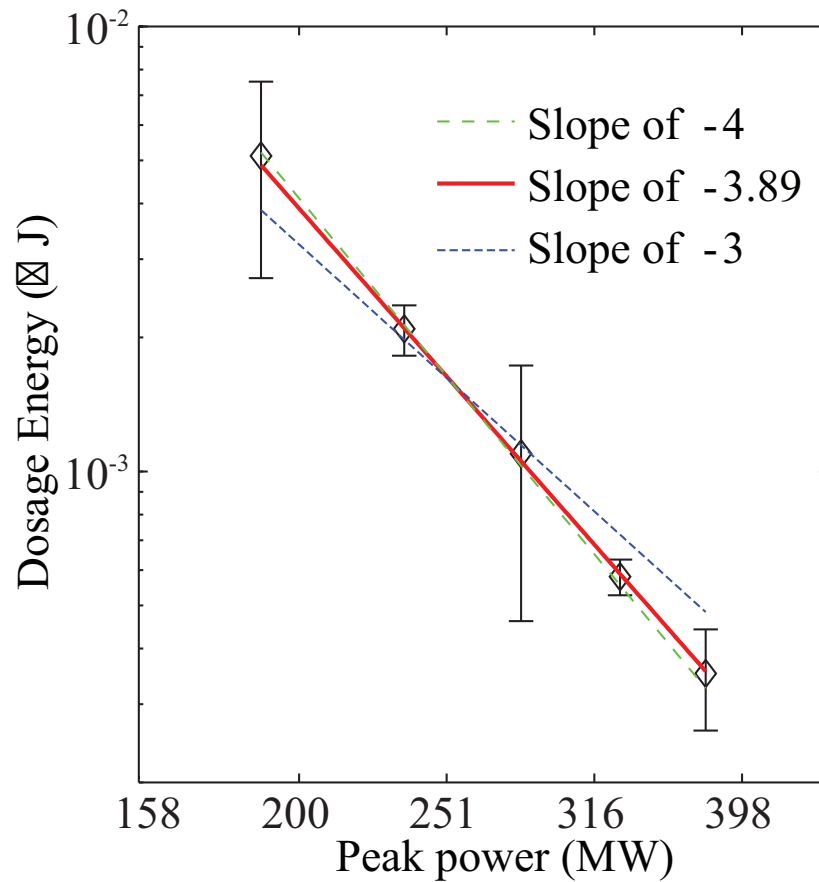
Figure 2.7: The average dosage energy needed to writing a grating vs. the pulse peak power of the recording beams.

and these values are expressed as the error bars on the graph. The theoretical lines for 3-photon absorption (dotted blue) and 4-photon absorption (dashed green) are added to the experimental data. The solid red line is the best fitted line, and has a slope of -3.89 ± 0.18. This result suggests that perhaps both three-photon absorption and four-photon absorption contribute to the writing of a grating.

Next, we irradiated the sample with a single pulse to observe a standard inter-ference pattern recorded on a multi-photon absorption material. To determine the
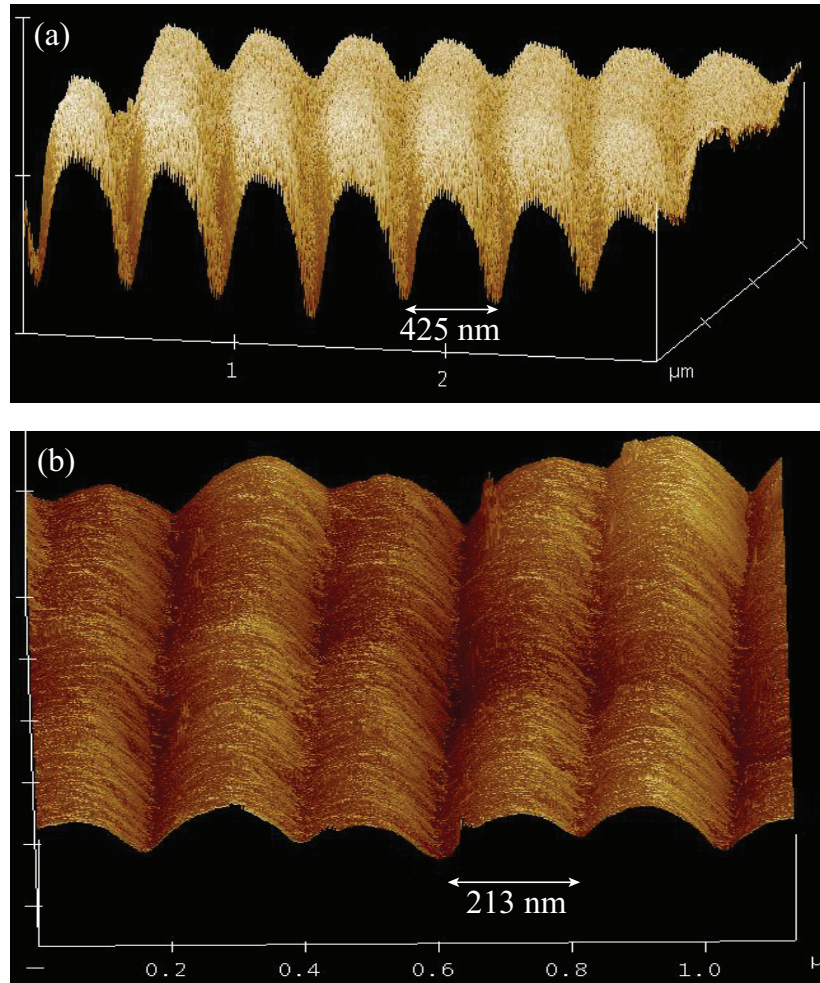
Figure 2.8: AFM images of the fringes recorded on a PMMA film as a result of (a) a single exposure and (b) a sequence of two exposures.

appropriate pulse energy, we repeated this measurement several times with different pulse intensities. We found that damage to the surface of the PMMA occurred when the pulse energy of either light beam exceeded 135 μJ. We also found that pulses weaker than 80 μJ could not produce a change in surface morphology even after development. We therefore used pulse energies in the range of 80 μJ to 135 μJ. The film's surface profile after exposure to the single pulse was measured by an atomic

force microscope and is shown in Fig. 2.8(a). In this case, the pulse energy was 130

μJ. As predicted in Eq. 1.8 using the incident angle of $\sim$70 degree, the recorded fringe

pattern has a period of 425 nm, which is close to the classical Rayleigh limit of $\lambda/2$.

As shown in the figure, the surface profile is sharp and not sinusoidal indicating that

the fringes are due to multi-photon absorption. From the sharpness of the grooves, we

can also conclude that PMMA is an N-photon absorber with $N \geq 3$ at a wavelength

of 800 nm.
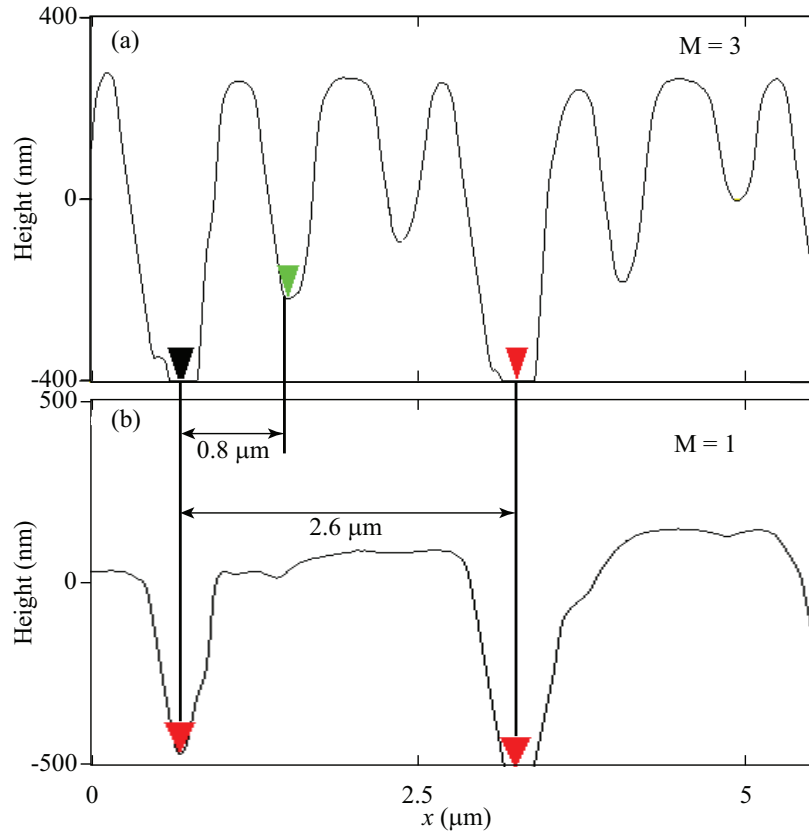
Figure 2.9: Cross sections from the AMF images of the fringes recorded on a PMMA film for (a) three-pulse irradiation in sequence (period $= 0.85$ μm $\sim \lambda/6sin\theta'$, $\theta' = 8.9°$) and (b) single-pulse irradiation (period $= 2.6$ μm $\sim \lambda/2sin\theta'$, $\theta' = 8.9°$).

To enhance the resolution of the fringes, we irradiated the sample twice in sequence. For the second exposure, the field in one arm is phase-shifted by π with respect to another arm. After the exposures, we performed the same development procedure as mentioned above. The surface profile is shown in Fig. 2.8(b). One can see that the fringe period is nearly 213 nm. This shows that we achieved a resolution that exceeds the Rayleigh limit ($\lambda/2$) at grazing angle by a factor of two.

In addition, we have shown that PMMA is at least a 3-photon absorber. We repeated the experimental process with three pulses with 80μJ per pulse in sequence, where the path-length difference between the two arms is adjusted to $\lambda/3$ and $2\lambda/3$ for the second and third shots respectively. For experimental simplicity, we reduced the incident angle to 8.9 degrees, so that the standard interference pattern has a period of 2.6 μm. The resulting surface modulation is shown in Fig. 2.9. As shown in Fig. 2.9(b), the fundamental period of the fringes using this incident angle with single pulse is 2.6 μm, and in Fig. 2.9(a), the period of written grating with three pulses is about 0.85 μm, indicating a three-fold resolution enhancement. As far as we know, this is the first experimental demonstration of spatial resolution enhancement by the phase-shifted grating method using a real lithographic material.

In Chapter of 2.3, the method to generate non-sinusoidal patterns was explained. Using non-uniform phase shifts between exposures, arbitrary patterns can be recorded in a multi-photon absorber and theoretical surface profile for non-sinusoidal fringe patterns are shown in Fig. 2.3. In our experiment, we irradiated a PMMA film
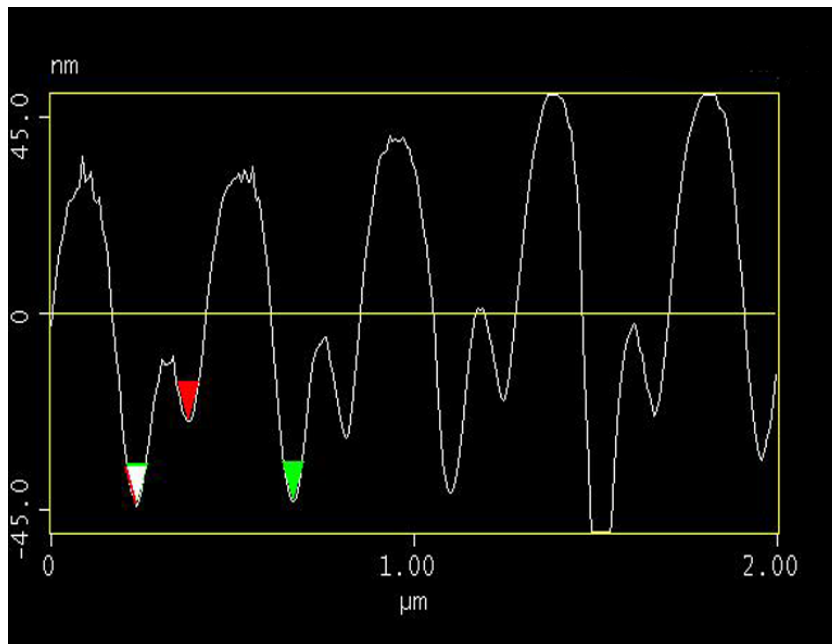
Figure 2.10: Surface profile of the non-sinusoidal fringes. In this case, we shifted the phase of the second shot by $\Delta = 4\pi/3$.

twice with non-uniform phase shift. A cross-section of the measured surface profile is shown in Fig. 2.10. The non-sinusoidal pattern was created by use of a $\pi + \triangle$ phase shift for $\triangle = \pi/3$. The smallest distance between any two fringes is 140 nm. Thus, PMMA should be able to support feature sizes of 140 nm or less. The experimental result matches the theory very well. This result might be useful in making arbitrary patterns from sinusoidal patterns[9, 10, 11, 12, 13, 14].

2.6 Summary

In summary, we have studied the phase-shifted grating method, and have demonstrated sub-Rayleigh lithography using PMMA as a multiphoton lithographic mate-

rial. PMMA is a UV lithographic material and we verified the multi-photon absorption nature of PMMA by measuring the average dosage energy needed to writing a grating versus the pulse peak power of the recording beams. The result of dosimetry shows that PMMA requires at least 3-photon absorption to break its chemical bonds at 800 nm. We have experimentally demonstrated the phase-shifted grating method, showing resolution enhancement by a factor of two and three, which is beyond the classical Rayleigh limit by means of the phase-shifted-grating method using a classical light source. In addition, we succeeded to generate arbitrary patterns by irradiating a PMMA film with non-uniform phase shifts between exposures.

Chapter 3

Quantum super-resolution

3.1 Introduction

The spatial resolution of optical imaging systems has traditionally been considered to be limited by the Rayleigh resolution criterion. One means of overcoming this limit [88] is to make use of the photon correlations that exist in certain quantum states of light. A specific example of such an approach is the quantum lithography (QL) proposal of Dowling and coworkers [4]. In this approach, a path-entangled state of N photons (a $N00N$ state) is used to write an interference pattern onto a recording material that responds by means of multi-photon absorption (MPA), producing N-fold-enhanced resolution as compared with a classical fringe pattern. Experimental procedures for creating $N00N$ states with up to $N = 5$ photons by means of spontaneous parametric down conversion have been reported by several groups

[71, 89, 90, 91, 92]. Experimental demonstrations of spatial superresolution through the QL procedure have, however, been rather limited. In one approach, multiphoton absorbing lithographic materials are mimicked by using two single-photon detectors operated in coincidence [93, 94]. In another, poly(methyl-methacrylate) was used as a MPA lithographic material for recording sub-Rayleigh interference patterns, but only when excited by intense classical light [83]. To realize true quantum lithography, very sensitive lithographic materials that can respond by MPA to weak quantum states of light are required. The use of time-energy-entangled multi-photons can provide significant enhancement of the MPA transition rate because of the near-zero variation in birth time [95, 96]. There has been some uncertainty in the trade-off between resolution enhancement and MPA enhancement [97, 98, 99, 100]. In summary, true quantum lithography has yet to be realized because of the low MPA efficiency of available materials.

In the present chapter, a new "optical centroid" method is described for achieving spatial interferometric superresolution with much higher detection efficiency than that of quantum lithography [101]. Instead of using detectors that respond MPA with low efficiency, single-photon measurements followed by post-processing will generate an interference pattern of optical centroids with resolution enhancement identical to QL, but with higher efficiency. Furthermore, we proposed an improved variation of Tsang's OCM method. The improvement comes about by implementing a form of photon-number-resolving (PNR) detection. A proof-of-principle demonstration

of spatial superresolution based on two-photon interference is demonstrated and is compared with that of the QL method. The interference fringes obtained by the OCM method are found to show resolution enhancement identical to that of the QL method, but with higher detection efficiency. To the best of our knowledge, ours is the first experimental demonstration of spatial resolution enhancement using the OCM method.

This chapter is organized as follows. The details of the optical centroid measurement method is introduced in Section 3.2, and the theory using quantum mechanics and combinatorics are described in Section 3.3 and 3.4, respectively. In Section 3.5, we describe the ways to generate $N00N$ states in our experiment. Section 3.6 presents experimental details, and experimental results are reported in Section 3.7. The summary is given in Section 3.8. The work described in this chapter is being prepared for publication.

3.2 Optical centroid measurement method

Tsang proposed an "optical centroid" method for achieving spatial interferometric superresolution with much higher detection efficiency than that of quantum lithography [101]. Instead of using detectors that respond by MPA as in quantum lithography, an array of single-photon detectors followed by postprocessing is used as shown in Fig. 3.1(a). The array is positioned on the detector plane of an interferometer, and N-photons arrive at N different pixels through either solid path or dashed path. The red
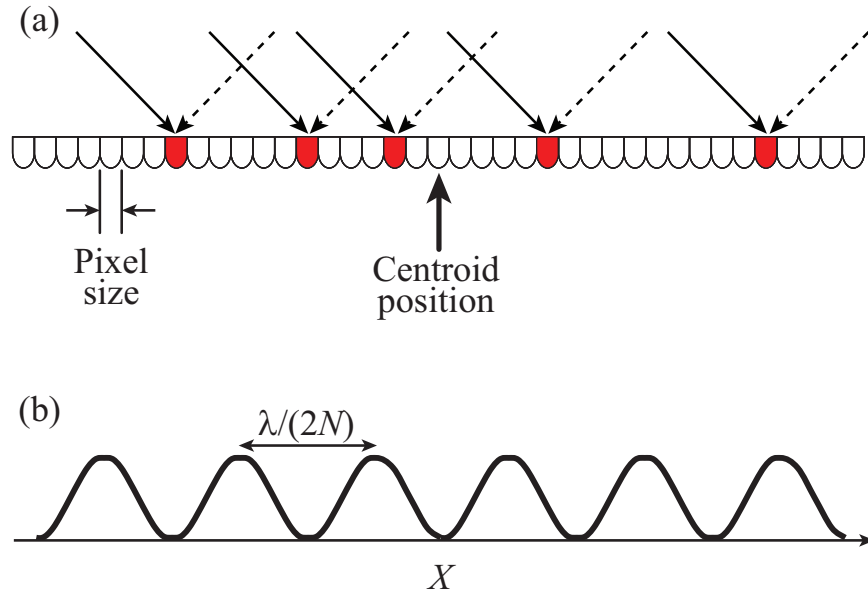
Figure 3.1: Schematic diagram of the optical centroid measurement method.

pixels represent the detectors fired by single-photon absorption. When the addresses

of the red detectors are determined, the centroid of the positions of those detectors is

computed (the vertical arrow). As shown in Fig. 3.1(b), a histogram of the positions

of optical centroids determined by repeated measurements is then produced. This

histogram shows an interference pattern with a resolution enhancement identical to

that of the QL method by a factor of N. If the pixel size of the detector array is much

smaller than the correlation area of the entangled photons, the probability that the

photons arrive at different pixels is much larger than the probability that they arrive

at same pixel. For this reason, the detection efficiency of the OCM method is much

higher than that of the QL method, which relies on MPA.

3.3   Quantum mechanical theory of OCM

Quantum mechanics can describe the spatial resolution of the quantum interfer-ometry. in the detector plane, using the approximation of one-dimension (x) and monochromatic light [98], the electric field operator is given by

$$\hat{E}^{(+)}(x) = i\sqrt{\frac{\eta}{(2\pi)^2}} \int dq \ \hat{a}(q)e^{iqx}, \tag{3.1}$$

where $\eta = \hbar/(2\epsilon_0 c^2 T)$ with T being the normalization time scale. Here q and x are respectively the transverse wavevector and transverse position on the detector plane. The $N00N$ state in the detector plane is given by

$$|N00N\rangle \ = \ \frac{1}{\sqrt{2N!}} \left\{ \left[\hat{A}^\dagger\right]^N + \left[\hat{B}^\dagger\right]^N \right\} |0\rangle \tag{3.2}$$

where $\hat{A}^\dagger$ and $\hat{B}^\dagger$ represent the annihilation operators of photons in arms A and B in front of the detector plane, respectively. These annihilation operators are given by

$$\hat{A}^\dagger \equiv (1/\sqrt{\Delta\kappa}) \int d\kappa \ F^* \left[(\kappa_A + \kappa)/\Delta\kappa\right] \hat{a}^\dagger(\kappa),$$
$$\hat{B}^\dagger \equiv (1/\sqrt{\Delta\kappa}) \int d\kappa \ F^* \left[(\kappa_B + \kappa)/\Delta\kappa\right] \hat{a}^\dagger(\kappa), \tag{3.3}$$

where κ_A and κ_B are the mean x-component of wavevector in arms A and B, respec-tively. Assume that $\hat{B}^\dagger$ has opposite direction to κ_A, so $\kappa_A = -\kappa_B = \kappa_0$. $\triangle\kappa$ is the uncertainty of the transverse wavevector. $F(q)$ is the transverse wavevector profile of

the photon packet and it is normalized as

$$\int dq \, |F(q)|^2 = 1. \tag{3.4}$$

Note that

$$[\hat{A}, \hat{A}^\dagger] = [\hat{B}, \hat{B}^\dagger] = 1 \tag{3.5}$$

By setting $\Delta\kappa$ small enough, i.e., $\kappa_0 \gg \triangle\kappa$, we have

$$\int d\kappa F\left(\frac{\kappa_0 + \kappa}{\Delta\kappa}\right) F^*\left(\frac{-\kappa_0 + \kappa}{\Delta\kappa}\right) = 0, \tag{3.6}$$

so that $[\hat{A}, \hat{B}^\dagger] = 0$.

In traditional N-photon coincidence quantum imaging, the spatial resolution measurement is achieved via the coincidence detection

$$
\begin{aligned}
P_C(x) &= \left\langle : \hat{I}(x)^N : \right\rangle \\
&= \left\langle \left[\hat{E}^{(-)}(x)\right]^N \left[\hat{E}^{(+)}(x)\right]^N \right\rangle \\
&= \left| \langle 0| \left[\hat{E}^{(+)}(x)\right]^N |N00N\rangle \right|^2 \\
&= N! \eta^N \Delta\kappa^N \left[f\left(-\Delta\kappa x\right)\right]^{2N} \left[1 + \cos\left(2N\kappa_0 x\right)\right],
\end{aligned}
\tag{3.7}
$$

where $f(z)$ is the Fourier transform of $F(q)$. On the other hand, the probability

distribution of the centroid is

$$
P_M(X) = \int d\xi_1 \cdots d\xi_{N-1} \left\langle : \prod_{n=1}^{N} \hat{I}(X + \xi_n) : \right\rangle
$$

$$
= \frac{N! \eta^N}{2(2\pi)^{2N} \Delta\kappa^N} \int d\xi_1 \cdots d\xi_{N-1}
$$

$$
\left\| \left[e^{-i\kappa_0 \left(NX + \sum_{m=1}^{N} \xi_m \right)} \prod_{n=1}^{N} \int d\kappa_n e^{i(\kappa_0 + \kappa_n)(X + \xi_n)} F^* \left(\frac{\kappa_0 + \kappa_n}{\Delta\kappa} \right) \right. \right.
$$

$$
\left. \left. + e^{i\kappa_0 \left(NX + \sum_{m=1}^{N} \xi_m \right)} \prod_{n=1}^{N} \int d\kappa_n e^{i(-\kappa_0 + \kappa_n)(X + \xi_n)} F^* \left(\frac{-\kappa_0 + \kappa_n}{\Delta\kappa} \right) \right] \right\|^2
$$

$$
= N! \eta^N \Delta\kappa^N \int d\xi_1 \cdots d\xi_{N-1} \prod_{n=1}^{N} |f(-\Delta\kappa(X + \xi_n))|^2
$$

$$
\times [1 + \cos(2N\kappa_0 X)], \tag{3.8}
$$

where the centroid and relative-position coordinates are defined as $X = \sum_{n=1}^{N} x_n / N$ and $\xi_n = x_n - X$ with $n = 1, \cdots, N$, respectively. Note that the term $\sum_{m=1}^{N} \vec{\xi}_m$ in the exponential factors sums to zero by its definition. Now $P_M(\vec{X})$ is a marginal probability density whereas $P_C(\vec{x})$ is a conditional probability density. They both give the same spatial resolution, but $P_M(\vec{X})$ can be much greater than $P_C(\vec{x})$.

If we set

$$
F(q) = (1/\sqrt{\pi}) \exp\left(-q^2/(2q_0^2)\right), \tag{3.9}
$$

where q_0 is some transverse scale parameter, the N-photon, conditional probability

density for the QL method becomes

$$P_C(x) = \frac{N! \eta^N \Delta\kappa^N}{\pi^N} e^{\left(-N\Delta\kappa^2 x^2\right)} \left[1 + \cos\left(2N\kappa_0 \, x\right)\right], \tag{3.10}$$

whereas the probability distribution of the centroid is given by

$$P_M(X) = \frac{N! \eta^N \Delta\kappa}{\sqrt{N}\pi^{N+1}} e^{\left(-N\Delta\kappa^2 X^2\right)} \left[1 + \cos\left(2N\kappa_0 \, X\right)\right], \tag{3.11}$$

The ratio of probabilities for two cases is

$$\frac{P_M(x)\delta x}{P_C(x)\delta x^N} = \left(\frac{\sqrt{\pi}}{\Delta\kappa\delta x}\right)^{N-1}, \tag{3.12}$$

where δx means the pixel size of detector. For typical applications in which the beam size is much larger than the pixel size of detector, $\Delta\kappa\delta x \ll 1$. Therefore, $P_M(X)$ can be much greater than $P_C(x)$.

3.4 Combinatorial theory of OCM

To provide an intuitive understanding of the tradeoffs between the QL and OCM methods, we present an analysis based on the use of combinatorics. We suppose that the correlation area of the photon field is M times larger than the pixel size on the detector array and that N entangled photons arrive at random positions on the detector array within this correlation area. The total number of combinations with

repetition for N photons falling on M pixels is

$$C_{\text{total}} = \frac{(M + N - 1)!}{N!(M - 1)!}.$$ (3.13)

Every such case occurs with equal probability $1/C_{\text{total}}$ because of the assumption of random positions. Therefore, the more combinations a particular method has, the more efficient it is. For instance, quantum lithography requires N-photon absorption,
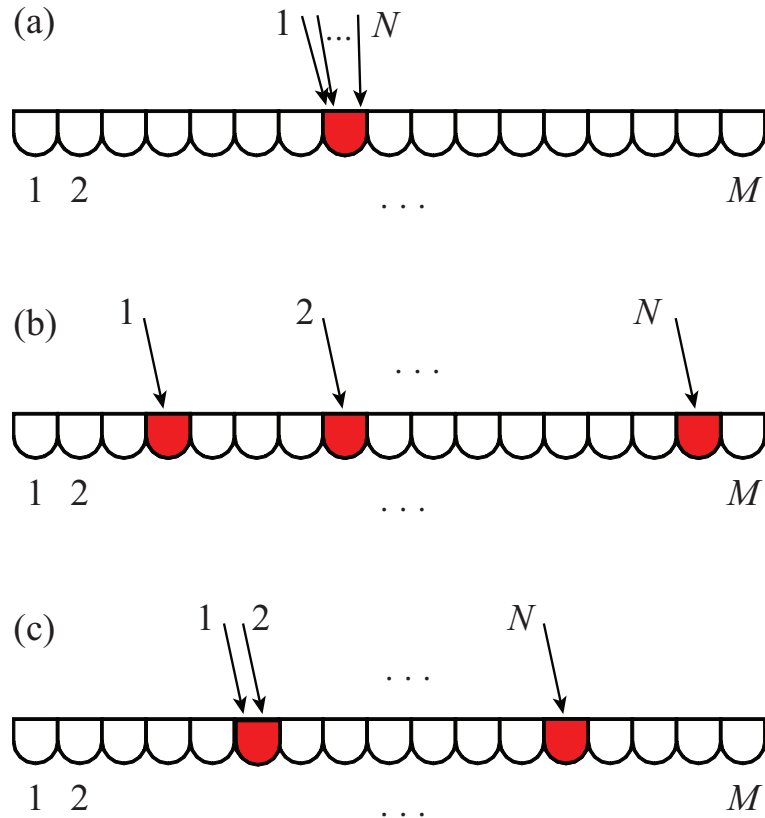
Figure 3.2: Schematic diagrams of three different detection cases. Optical centroid measurement by means of (a) multi-photon absorption, (b) single-photon absorption, and (c) photon-number-resolving.

and the number of cases of N photons falling onto the same pixel is

$$C_{\mathrm{MPA}} = M. \tag{3.14}$$

If all N photons do not fall onto the same detector this event will be lost, leading to decreased detection efficiency. In the OCM method, however, a single-photon detector array is used, and the number of combinations of detecting N photons by N different pixels among the M pixels is

$$C_{\mathrm{SPA}} = \frac{M!}{N!(M-N)!}. \tag{3.15}$$

For small pixel size or large correlation area $(M \gg N)$, the OCM method will be much more efficient than the QL method $(C_{\mathrm{total}} \sim C_{\mathrm{SPA}} \gg C_{\mathrm{MPA}})$ as Tsang predicted.

In the laboratory, however, practical concerns may preclude the pixel area from being much smaller than the correlation area. Moreover, most currently available high-sensitivity detectors are not photon-number resolving (PNR), that is, they cannot distinguish between one and several photons falling onto the detector. If more than one photon arrives at a given pixel, the single-photon detector will count this as a single event, and fewer than N detectors will register. Then the OCM protocol will discard this event, leading to decreased measurement efficiency. This loss of efficiency becomes increasingly more significant for large photon numbers N or small values of M.

Loss of efficiency due to multi-arrivals at one pixel can be eliminated by using a photon-number-resolving detector array. Recently, PNR detectors based on superconductive nanowire technology with high quantum efficiency have been developed [102]. The PNR detector array will measure the addresses of pixels that fire as well as the number of photons at these pixels. An accurate optical centroid of the detection process can thereby be computed. The OCM method with a PNR detector array has the number of combinations with repetition for N photons falling onto the array given by

$$C_{\mathrm{PNR}} = \frac{(M + N - 1)!}{N!(M - 1)!}.$$

(3.16)

This result indicates that the PNR detector array can use all of the cases of N photons arriving at the detector. The PNR detector array will work like a MPA detector array for $M \sim 1$ and will be almost equal to the single-photon OCM detector for $M \gg N$.

3.5 Experimental details

We have performed experimental studies of superresolution for two-photon interference (that is, $N = 2$) for both the QL and OCM methods. The experimental setups are the same for both cases except for the detection method, as shown in Fig. 3.3. A UV light beam at 400-nm wavelength is generated by second-harmonic generation of 100-fs pulses at 800-nm wavelength at repetition rate of 82 MHz and is split into

two beams by a beam splitter (BS1). A 1.5-mm-thick BBO crystal is placed in each (mutually coherent) UV beam, and spontaneous parametric down conversion occurs randomly in each crystal under type 1 collinear phase matching conditions. After blocking the pump beams using interference filters (IF), the photon number state $|\Phi\rangle$ in mode a and b is given by

$$|\Psi\rangle = |0\rangle_a|0\rangle_b + \gamma(|2\rangle_a|0\rangle_b + |0\rangle_a|2\rangle_b)/\sqrt{2} + \dots, \tag{3.17}$$

where γ is the probability of creating a photon pair by parametric down-conversion. At low pump power, γ is much smaller than unity and we can thus ignore multi-pair generation proportional to higher powers of γ. The generated light is then well approximated as a two-photon $N00N$ state. This procedure for generating the 2002 state is convenient because it avoids the need for a maintaining the sensitive alignment of a Hong-Ou-Mandel setup [71]. Moreover, strong photon flux can be obtained by using long crystals or periodically poled crystals [103]. The dashed lines indicate the downconverted photon-pair fluxes. We use a second beam splitter (BS2) to combine these two beams with a small angle ($\theta \sim 0.033°$) between them. To increase the collection efficiency, two spherical lenses with 10-cm focal length are located after each IF, and each spherical lens is defocused by 0.5 mm to make the correlation area larger than the pixel size. The measured correlation area has a diameter of approximately 0.5 mm.

The dashed box represents the detection system used to measure the two-photon
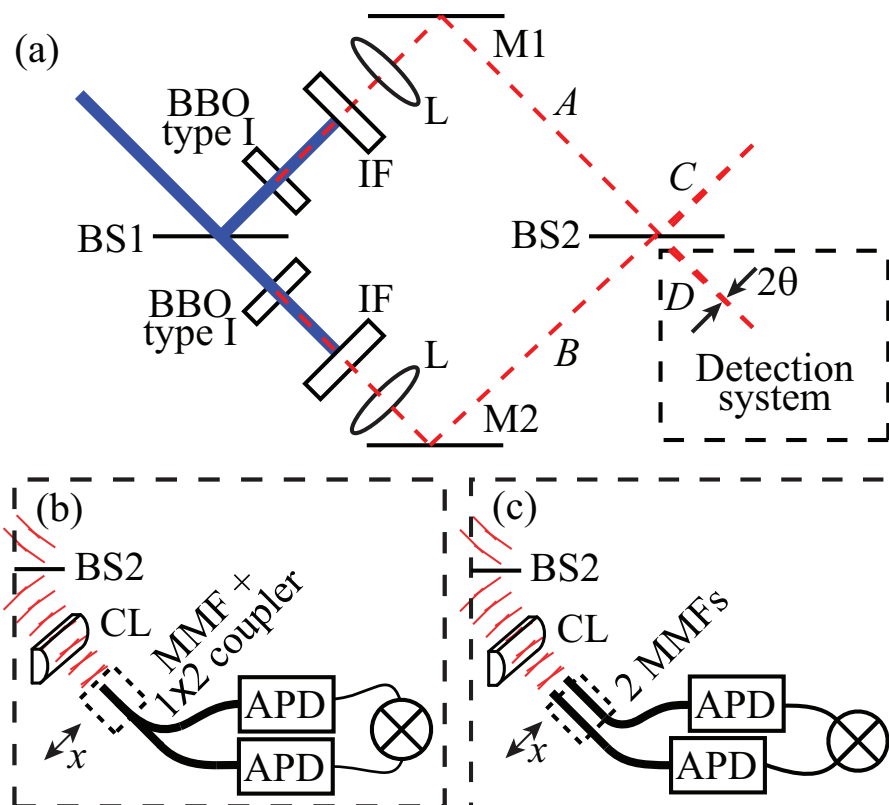
Figure 3.3: (a) Experimental setup for producing two-photon interference. (b) The detection system for the QL process. (c) Detection system for the OCM procedure, as described in the text. In each case, a cylindrical lens (CL) is positioned in front of the detection systems to increase collection efficiency and the coincidence window time was 7 ns. APD = avalanche photodiode.

interference pattern. The two detection systems were prepared using multimode fibers (MMFs) whose core and cladding sizes are 62.5 μm and 125 μm, respectively. For the QL case (see Fig. 3.3(b)), a single MMF acting as a collector was scanned in discrete steps of 50 μm across the detection region using a motorized translation stage. The output of this fiber was split into two additional MMFs whose outputs were monitored by two single-photon detectors operating in coincidence [94]. The coincidence circuit counts how many photon pairs arrive simultaneously at the position of the input fiber, thus emulating a two-photon detector.

The OCM detection system was constructed as follows. According to the OCM proposal, the detection system should consist of a linear array of detectors each of which can respond with high sensitivity to individual incident photons. Detector arrays of this sort are not readily available. Instead, we simulated such a detection system by using two MMFs of variable separation serving as detectors, as shown in Fig. 3.3(c). For a given fixed separation, this fiber pair is scanned through the detection region while coincidence counts are recorded. The coincidence circuit counts how many photons arrive simultaneously at the two spatially separated inputs. The centroid position is located at the mean position of the two fibers. This procedure is then repeated sequentially for other fiber-to-fiber separations of 125, 250, 375, 500, and 625 μm. The coincidence count rates at a given centroid position are then summed for all fiber separations. In this manner we collect the same data that would have been collected (although more rapidly) by a multielement detector array. To

simulate a PNR detector array, we include the case of a single collection fiber coupled to two single-photon detectors (Fig. 3.3(b)) to the cases of two collection fibers of variable separation (Fig. 3.3(c)). The coincidence circuit counts how many photons arrive at two spatially separated inputs simultaneously, and it is different from the QL detector due to non-overlapping positions of photons.

3.6 Results

Our experimental results are shown in Fig. 3.4. In part (a) of the figure, we show the form of the classical, single-photon interference fringes. These results were obtained using strongly attenuated laser light of 800-nm wavelength, and serve as a reference. Under our experimental conditions, the period of these classical interference fringes was 0.69 mm. Next, two-photon interference fringes were recorded using the QL detector of Fig. 3.3(b). Both singles counts and coincidence counts are shown in Fig. 3.4(b). The singles counts show a Gaussian profile, whereas the coincidence counts exhibit an interference pattern with a decreased period of about 0.34 mm. Therefore, the QL method shows a factor-of-two increase in spatial resolution as predicted [4] and observed previously in references [93] and [94].

Next, we repeated the measurement of the two-photon spatial interference pattern using our OCM detection system. The single- and two-photon count rates for MMFs separated by 125 μm are shown in Fig. 3.4(c). Because of the fiber separation, the single-photon data have different peak positions separated from each other by
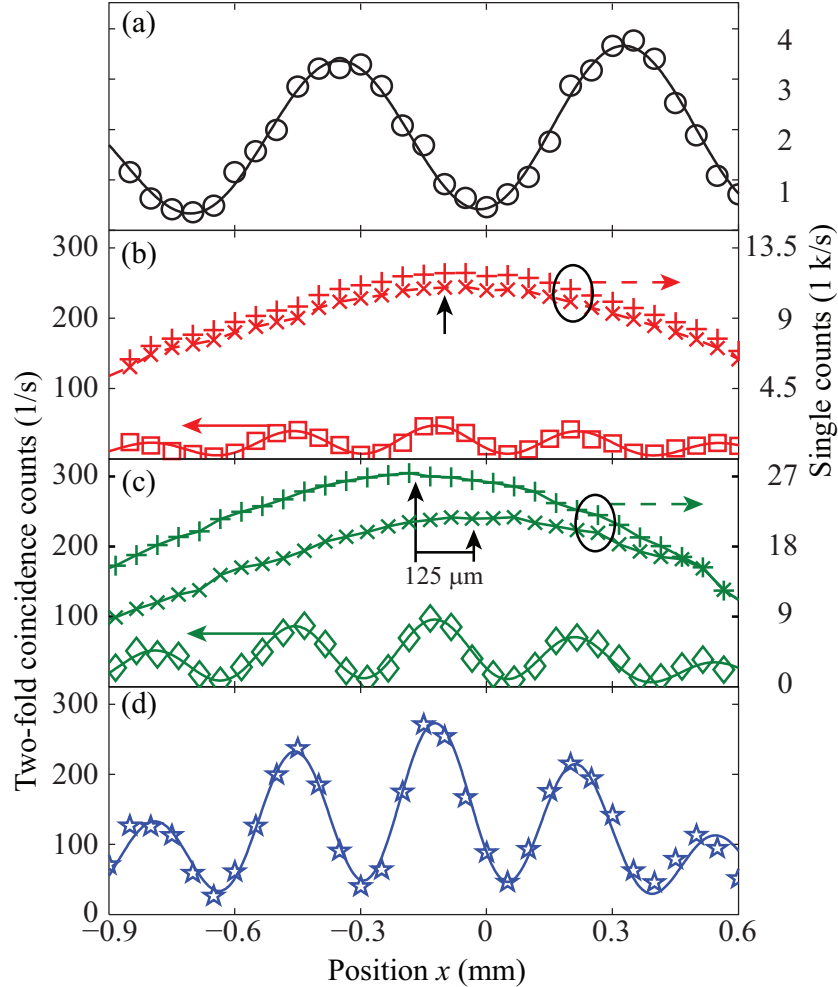
Figure 3.4: (a) Single-photon count rate using strongly attenuated coherent state beam at 800-nm wavelength vs the scanning position x. Single-photon (marked $+$ and $\times$) and two-photon count rates in the 2002 state detected by (b) the two-photon QL detector, (c) two parallel MMFs with two detectors for a fiber separation of 125 μm, and (d) the two-photon OCM system with PNR detectors. The vertical arrows point the positions of the maximum single-photon count rates. The fitted curves are added to the experimental data. The integration time was 10 seconds.
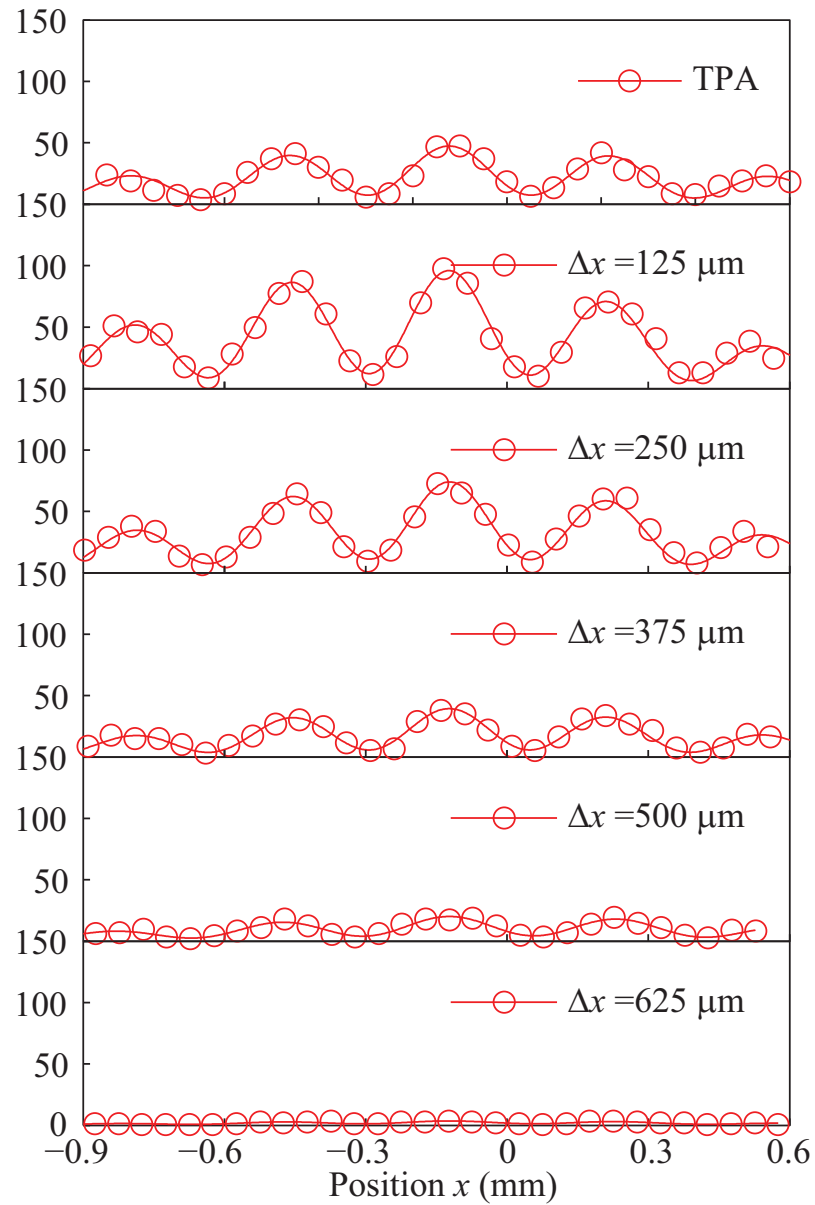
Figure 3.5: Two-photon count rates in the 2002 state detected by two parallel MMFs with two detectors for various fiber separation (0, 125, 250, 375, 500, and 625 μm), where the 0-μm fiber separation indicates the QL system.

approximately 125 μm. The period of the two-photon fringes is approximately 0.34 mm, the same as the QL result, demonstrating enhanced resolution by the OCM method. The fitted curve for the two-photon coincidence counts is a sinusoidal pattern weighted by a Gaussian function. Measurements of the sort shown in Fig. 3.4(c) were repeated for the other fiber separations as shown in Fig. 3.5. We then add all of these traces together to give the results shown in Fig. 3.4(d). Under our experimental conditions, the two-photon interference fringes obtained by the OCM method has about a six-times larger fringe amplitude than the QL result. This enhancement factor depends on the value of the parameter M. Specifically, the OCM method increases the efficiency compared to the QL method as we use a detector array of smaller pixel size or enlarge the correlation area.

The OCM method is expected to scale well to higher values of N and thus provide still greater spatial resolution. However, the implementation studied here based on the use of N detectors of variable separation provides a highly inefficient means of scaling to higher N, because of the large number of detector configurations that must be used. With incomplete OCM detection systems, the single-photon detection efficiency decreases proportionally to the ratio of the detector size to the beam size inducing an addition loss to the system. Any loss makes worse N-photon detection efficiency because of its Nth power dependence on the single-photon detection efficiency.

Instead of observing 'spatial' interference fringe patterns, we measured 'phase' four-photon interference patterns to test our system for four-photon interferometry
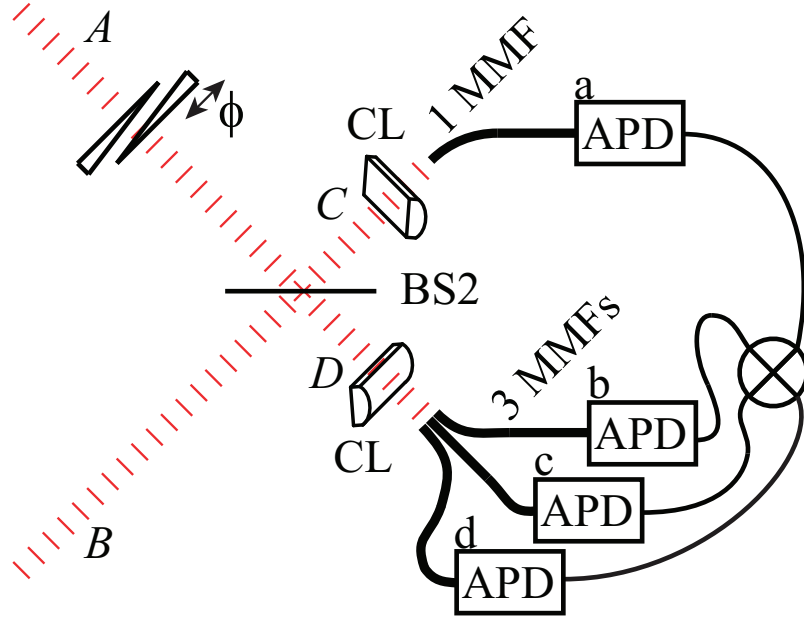
Figure 3.6: Schematic diagram of the detection system for four-photon interference using spatially separated MMFs.

and to prove that multi-photon effects can be measured by using spatially separated detectors like the OCM detectors not by using multi-photon absorbing detectors. Under our experimental conditions, the four-photon number state $|\Psi_4\rangle$ in mode A and B can be given as

$$|\Psi_4\rangle = \frac{1}{\sqrt{4}}(|4\rangle_A|0\rangle_B + |0\rangle_A|4\rangle_B) + \frac{1}{\sqrt{2}}|2\rangle_A|2\rangle_B), \tag{3.18}$$

but there exists the unwanted $|22\rangle_{AB}$ term. Quantum interference cancels the contribution from this $|22\rangle_{ab}$ state to one and three photons in modes C and D via post-selection [94]. As shown in Fig. 3.6, spatially separated four-photon detector consists of one MMF and three MMFs with four APDs at the upper and lower outputs

of the second beam splitter, respectively. We reduced the beam size at the detection plane covering barely our detector area (3 MMFs) to increase 4-photon detection efficiency, and the interference pattern was recorded while varying the phase of one arm with zero incidence angle ($\theta \sim 0$) as shown in Fig. 3.6. Two-photon interference fringes are plotted in Fig. 3.7(a) versus phase variation in arbitrary units. The odd number of reflection from BS2 induces π phase shift to the two-photon interference fringe by detector A and C compared to that by detector B and C. The four-photon interference fringe is shown in Fig. 3.7(b) showing two-fold enhancement of resolution compared to the resolution of the two-photon interference fringes. This result
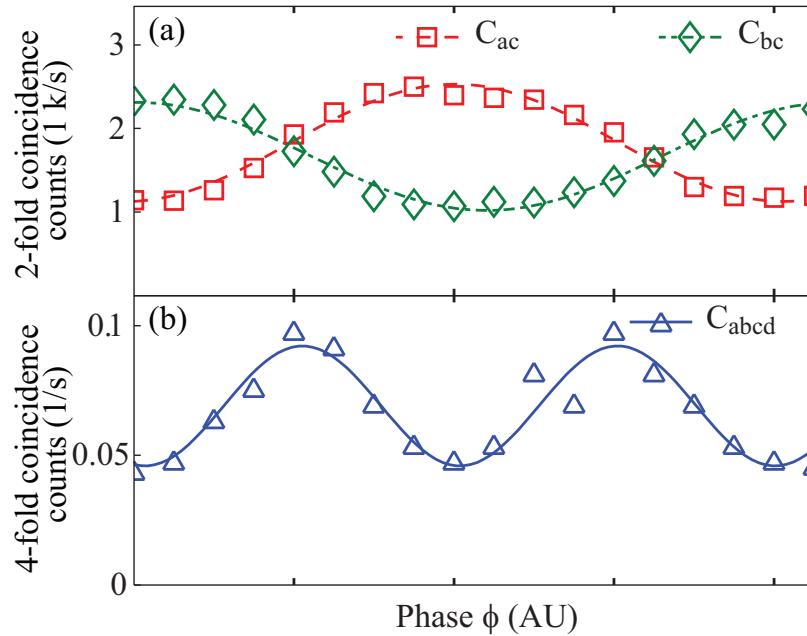
Figure 3.7: (a) Two-photon coincidence counts (C_{AC} and C_{BC}, marked $\square$ and $\diamondsuit$), and (b) four-photon coincidence counts (marked $\triangle$) of a phase interference vs phase variation in arbitrary units. The fitted curves are added to the experimental data. The integration time was 500 seconds.

indicates that four-photon effects can be measured by spatially separated detectors showing resolution enhancement by a factor 4.

Nonetheless, the results presented here provide a proof-of-principle demonstration that the OCM method for $N = 2$ can provide superresolution with a two-fold enhancement over the classical resolution limit. We have also shown that the OCM method provides the same degree of resolution enhancement as the QL method but with higher efficiency. We feel that when large arrays of single-photon detectors become available the OCM method will be a powerful means of providing still greater enhancement in resolution.

3.7 Summary

Quantum lithography (QL) has been suggested as a means of achieving enhanced spatial resolution for optical imaging, but its realization has been held back by the low multi-photon detection rates of recording materials. Recently, an optical centroid measurement (OCM) procedure was proposed as a way to obtain spatial resolution enhancement identical to that of QL but with higher detection efficiency [101]. In this chapter, we studied the OCM method using quantum mechanics and combinatorics. We report a laboratory demonstration of the OCM method based on two-photon interference monitored by single-photon detectors. We compare these results with those of the standard QL method based on multi-photon detection and show that the new method leads to superresolution but with higher detection efficiency. This is the

first proof-of-principle experiment of the OCM method showing two-fold resolution enhancement of quantum interference patterns with higher efficiency than the traditional QL method. We believe this method can be used for higher photon-number cases with much larger detection efficiency than the QL method and allow us to become one step closer to the realization of quantum imaging with super-resolution.

Chapter 4

Fast-Light Pulse-Distortion

Management

4.1 Introduction

The use of controllable slow- and fast-light pulse propagation through material systems has been of recent interest to the telecommunications and information processing communities [46, 47]. Since distortion can compromise the information content of a stream of pulses, distortion reduction mechanisms are particularly important. Recently, several methods for reducing pulse distortion in slow- and fast-light propagation have been reported for applications in telecommunication and information processing. Song *et al.* [48] reported that pulse advancement caused by the large anomalous dispersion appearing between two separated stimulated-Brillouin-

scattering (SBS) gain peaks induced less distortion than that of a slightly detuned single gain peak. Stenner *et al.* [49] achieved reduced distortion in a slow light system by using an overlapping SBS gain doublet, which decreased distortion by a factor of 2 compared with a single gain line. Khurgin *et al.* [50] suggested that the performance of tunable buffers can be improved by using gain flattening. In addition, Minardo *et al.* [51] applied distortion-management techniques using three equally spaced Lorentzian SBS gain lines. Recently, Shi *et al.* [52, 53] improved this technique for random pulse trains by optimizing the spacings and relative strengths of the SBS gain lines, and Pant *et al.* [54] designed optimal gain profiles for broadband SBS slow-light system. Schneider *et al.* [55] showed zero-broadening in SBS based slow light system. Furthermore, Camacho *et al.* [56] achieved large group delay with low distortion for a pulse tuned between two widely spaced absorption resonances in a rubidium vapor.

In the present chapter, the pulse-on-background (POB) method is studied for minimizing pulse distortion induced by the fast-light propagation through an erbium doped fiber amplifier (EDFA). When a pulse superposed on a continuous-wave background propagates through an erbium-doped fiber amplifier with a negative group velocity, either pulse broadening or pulse compression can be observed. These effects can be explained in terms of two competing mechanisms: gain recovery and pulse spectrum broadening. The distortion of the pulse shape caused by these effects depends on input pulse width as well as pulse power, pump power, and background-

to-pulse power ratio. With the proper choice of these parameters, distortion can be minimized while maintaining significant pulse advancement. Furthermore, we show that comparable distortion reduction can be obtained through use of a mutually incoherent background field such as from a separate laser, a procedure that could be much more readily implemented under many circumstances.

This chapter is organized as follows. In Section 4.2 and 4.3, the mechanisms of pulse broadening and pulse compression in an erbium doped fiber amplifier are introduced. Five-level-system rate equations for erbium ions are described in Section 4.4 for the purpose of numerical calculation of pulse propagation through the EDFA. Sections 4.5 present experimental details. In Section 4.6, we report experimental results of pulse-distortion management using the pulse-on-background method for various experimental conditions. Section 4.7 shows an experimental result of distortion reduction by means of using a mutually incoherent background field. The summary is given in Section 4.8. The work described in this chapter has been published in Optics Express [104] and Optics Communications [105].

4.2 Mechanism of pulse broadening

Recently, we observed pulse compression [78] as well as pulse broadening [40] in an erbium-doped fiber amplifier (EDFA) by about 10% of the pulse width in each case. In both cases, the amplifier was operated in the fast-light regime with fast-light propagation occurring as a consequence of coherent population oscillations (CPO). The

intent of the present and next sections is to investigate the mechanisms responsible for the pulse broadening and compression.

Pulse broadening can be understood in the time domain. Fast light by CPO occurs in the nonlinear regime, i.e., when the signal power is comparable to or greater than the saturation power of medium. Pulse broadening is caused by time dependent saturation of the amplifier gain when the input pulsewidth is comparable to the carrier lifetime. The process can be explained as follows: Without any background, the amplifier gain is quickly depleted by the leading edge of a pulse. If the pulsewidth of the input pulse is long enough, a strong applied pump field can re-excite the medium and the saturated gain has time to recover during the pulse. This "gain recovery" occurs over a characteristic time that depends on both the lifetime of the metastable state and the applied pump intensity. A partial gain recovery affects both the shape
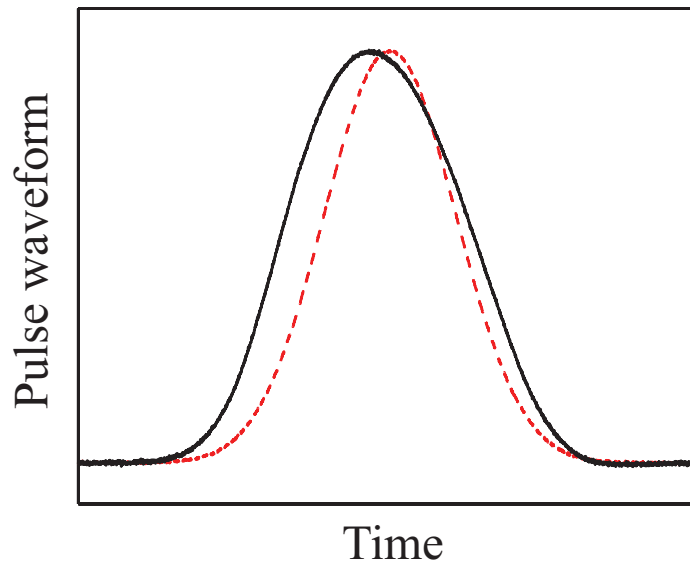
Figure 4.1: Input and output pulse waveforms without a background field vs. time.

and the spectrum of output pulses. If the input pulse duration is comparable to or longer than the gain recovery time, the trailing edge of the pulse may experience this recovered gain, broadening the pulse [106]. Fig. 4.1 shows an instance of pulse broadening. The solid and dashed curves are respectively the output and input pulse waveforms versus time. The peak of the output pulse is shifted forward, indicating fast-light pulse propagation. The leading edge of the output pulse is not altered significantly, but the trailing part of the output pulse becomes thicker than that of the input pulse, broadening the pulse due to the gain recovery effect. In the next section, we will explain the pulse compression mechanism.

4.3 Mechanism of pulse compression

Pulse compression can be explained in the frequency domain as spectral broadening; the broadened pulse spectrum results in a temporally narrower pulse. When a pulse is superposed on a continuous wave background that is larger than the saturation intensity of an EDFA ($I_{sat} \sim 3$ kW/cm^2 at 1550 nm), CPO creates a narrow hole in the EDFA gain profile as shown in Fig. 4.2(a), producing anomalous dispersion. In this case, the EDFA becomes a linear material. In Fig. 4.2(a), the solid blue curve is the gain spectrum near the central frequency versus frequency and the dashed red curve is the normalized pulse spectrum. The sharp peak on top of the pulse at the central frequency ω_0 is the CW background field. In this case, the wings of the pulse spectrum experience a larger gain than the central frequency components, broadening

the output pulse spectrum (the solid black curve) as shown in Fig. 4.2(b). An instance of pulse compression is illustrated in Fig. 4.2(c). The solid and dashed curves are respectively the output and input pulse waveforms versus time. The output pulse is shifted forward in time, and the pulsewidth is compressed. The leading edge of the output pulse is not altered significantly, but a large dip is located on the trailing part of the pulse. Cao *et al.* explained this pulse compression with the negative second
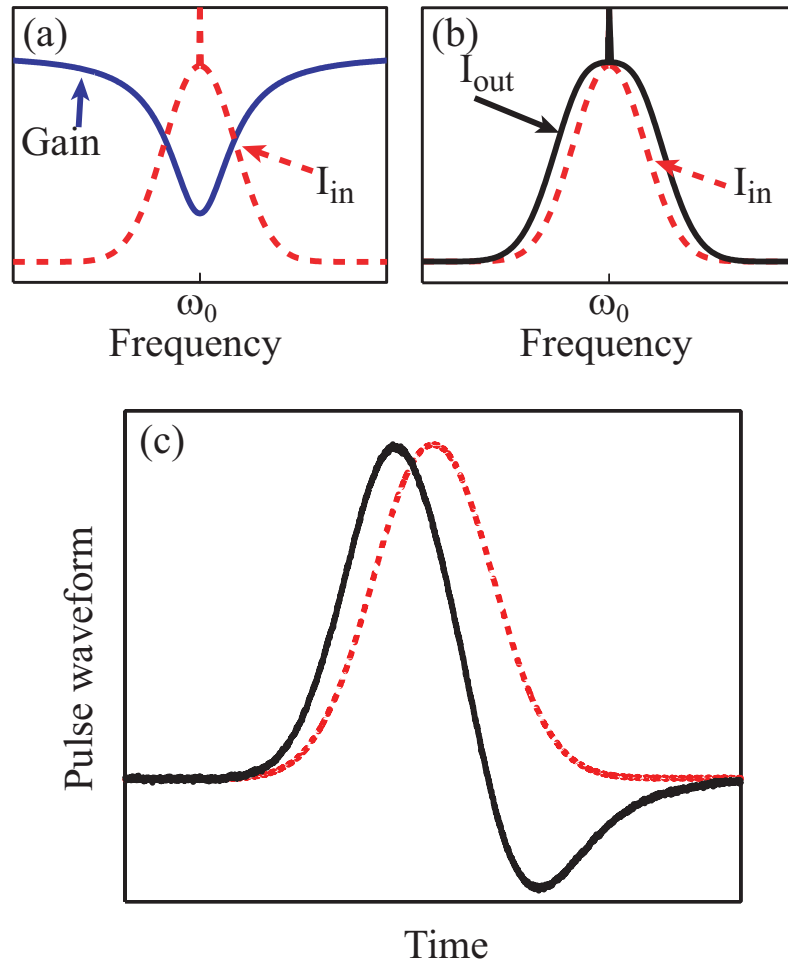
Figure 4.2: (a) Gain hole spectrum induced by coherent population oscillations and the input pulse spectrum. (b) Input and output pulse spectrums. (c) Input and output waveforms.

derivative of the absorption coefficient and derived the pulse compression and the advancement factors [107]. This mechanism, which we refer to as "pulse spectrum broadening," competes with gain recovery. By controlling these two mechanisms, we can regulate the amount of broadening or compression experienced by a pulse during propagation through an amplifier.

4.4 Rate equations for erbium ions

To model our experimental observations, we perform computer simulations of pulse propagation through the EDFA by numerically solving the 5-level-system rate equations for erbium ions including amplified spontaneous emission (ASE) [108, 109]. Pump and signal absorption processes are considered as shown in Fig. 4.3. Er^{3+} ions in the ground state (1) transit to an excited state (3) by absorbing a 980-nm pump photon. From the excited state, the ions decay to the metastable state (2) with a short lifetime (7 μs) or are re-excited to a higher energy level by excited state absorption (ESA). The metastable state has a relatively long lifetime of about 10 ms, and erbium ions can transit between the metastable state and the ground state by absorbing or emitting 1550-nm signal photons. We also consider pump ESA from the metastable state and the very fast and non-radiative decay from higher energy levels. The rate equations of erbium ions in an EDFA are
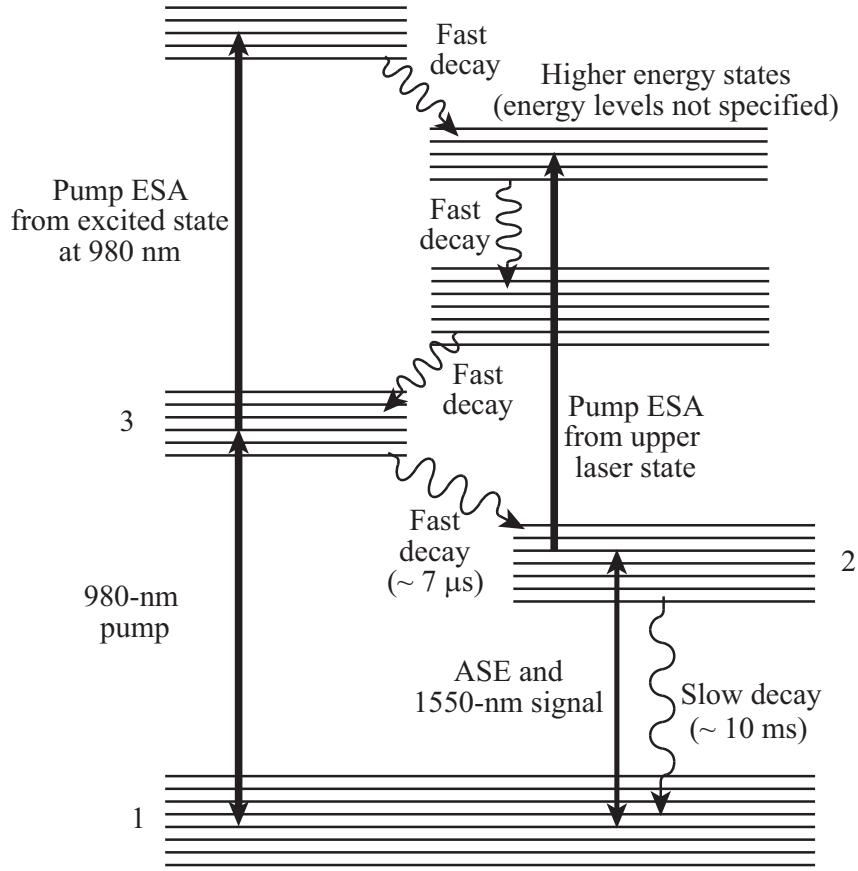
Figure 4.3: Energy diagram of erbium ions.

$$\frac{dN_1}{dt} = \sum_i \left[\frac{N_2 \sigma^e(\nu_i)}{h\nu_i A_S} - \frac{N_1 \sigma^a(\nu_i)}{h\nu_i A_S} \right] P_{S,ASE}(\nu_i)$$

$$+ \left[\frac{N_3 \sigma^e(\nu_P)}{h\nu_P A_P} - \frac{N_1 \sigma^a(\nu_P)}{h\nu_P A_P} \right] P_P + \frac{N_2}{\tau_{21}}, \tag{4.1}$$

$$\frac{dN_2}{dt} = \sum_i \left[\frac{N_1 \sigma^a(\nu_i)}{h\nu_i A_S} - \frac{N_2 \sigma^e(\nu_i)}{h\nu_i A_S} \right] P_{S,ASE}(\nu_i) - \frac{N_2}{\tau_{21}} + \frac{N_3}{\tau_{32}}, \tag{4.2}$$

$$\frac{dN_3}{dt} = \left[\frac{N_1 \sigma^a(\nu_P)}{h\nu_P A_P} - \frac{N_3 \sigma^e(\nu_P)}{h\nu_P A_P} \right] P_P + \frac{N_3}{\tau_{32}}, \tag{4.3}$$

where:

$N_{1,2,3} \equiv$ average number of Er^{3+} ions in the ground, metastable, and excited states, respectively,

$A_{S,P} \equiv$ effective signal and pump mode areas, respectively,

$\sigma^{a,e}(\nu_i) \equiv$ absorption and emission cross-section at a frequency of ν_i,

$1/\tau_{21,32} \equiv$ decay rates of the metastable state and the excited state, respectively,

$P_{P,S} \equiv$ pump and signal power at 980 nm and 1550 nm, respectively, and

$P_{ASE}(\nu_i) \equiv$ ASE power at a frequency of ν_i.

In the simulations, the mode area of the ASE is approximately equal to that of the signal field. All mode areas are assumed independent of longitudinal position, even though this is not strictly true. The longitudinal dependence of the ASE, signal, and pump power levels is included by stepping the waves along the fiber in small steps and computing the inversion and gain coefficient at each step [108]. Equations for the development of the signal, pump, and ASE fields are given by

$$\frac{dP_S(z, \nu_S)}{dz} = \frac{A_C}{A_S} \left[N_2(z)\sigma^e(\nu_S) - N_1(z)\sigma^a(\nu_S) \right] P_S(z, \nu_S), \tag{4.4}$$

$$\frac{dP_P(z, \nu_P)}{dz} = -\frac{A_C}{A_P} \left[N_1(z)\sigma^a(\nu_P) - N_3(z)\sigma^e(\nu_P) \right] P_P(z, \nu_P)$$
$$-\frac{A_C}{A_P} \left\{ [N_3(z) + N_2(z)] \sigma_{ESA}^a(\nu_P) \right\} P_P(z, \nu_P) \tag{4.5}$$

$$\frac{dP_{ASE}^\pm(z, \nu_i)}{dz} = \pm\frac{A_C}{A_S} \left[N_2(z)\sigma^e(\nu_i) - N_1(z)\sigma^a(\nu_i) \right] P_{ASE}^\pm(z, \nu_i)$$
$$\pm\frac{A_C}{A_S} N_2(z)\sigma^e(\nu_i) 2h\nu_i \left(\frac{\Delta\nu_i}{n} \right) \tag{4.6}$$

where:

$A_C \equiv$ fiber core area,

$\sigma_{ESA}^a(\nu_P) \equiv$ absorption cross-section at pump frequency,

$P_{ASE}^\pm(z, \nu_i) \equiv$ ASE field at a position z and a frequency of ν_i, where $+$ and $-$ indicate forward and backward propagation, respectively,

$\Delta\nu_i \equiv$ spectral width of ASE signal at ν_i, and

$n \equiv$ refractive index of the fiber.

The last term in Eq. 4.6 is the spontaneous emission power at a given point in the fiber, referred to as an equivalent noise power. The spontaneous emission rate into a given mode is the same as the stimulated emission rate into that mode with one photon already present in the mode [110]. The total ASE power at a point z along

Table 4.1: Coefficients used in the numerical calculations.

Er^3+ concentration, N_{total}	3.4×10^{24} m^{-3}
Fiber core area, A_C	7.35×10^{-12} m^2
Effective pump mode area, A_P	9.62×10^{-12} m^2
Effective signal mode area, A_S	2.73×10^{-11} m^2
Excited state lifetime, τ_{32}	7×10^{-6} s
Metastable state lifetime, τ_{21}	10.5×10^{-3} s
Erbium doped fiber length, L	9.4 m
Signal emission cross-section, $\sigma^e(\nu_S)$	2.97×10^{-25} m^2
Signal absorption cross-section, $\sigma^a(\nu_S)$	2.13×10^{-25} m^2
ESA absorption cross-section, $\sigma^a_{\text{ESA}}(\nu_P)$	2.5×10^{-26} m^2
ASE absorption cross-section, $\sigma^a_{\text{ASE}}(\nu_i)$	
1425 nm	4.10×10^{-26} m^2
1475 nm	1.34×10^{-25} m^2
1512.5 nm	2.44×10^{-25} m^2
1537.5 nm	3.05×10^{-25} m^2
1565 nm	1.1×10^{-25} m^2
1615 nm	1.43×10^{-26} m^2
ASE emission cross-section, $\sigma^e_{\text{ASE}}(\nu_i)$	
1425 nm	7.94×10^{-27} m^2
1475 nm	4.02×10^{-26} m^2
1512.5 nm	1.6×10^{-25} m^2
1537.5 nm	3.19×10^{-25} m^2
1565 nm	1.95×10^{-25} m^2
1615 nm	3.63×10^{-26} m^2
ASE linewidth, $\Delta\sigma_{\text{ASE}}(\nu_i)$	
1425 nm	7.39×10^{12} m^2
1475 nm	6.89×10^{12} m^2
1512.5 nm	3.28×10^{12} m^2
1537.5 nm	3.17×10^{12} m^2
1565 nm	3.67×10^{12} m^2
1615 nm	8.05×10^{12} m^2

the fiber is the sum of the ASE power from the previous sections of the fiber and the added local spontaneous emission power. The values of some coefficients used in the simulations are listed in Table 4.1.

4.5   Experimental details

To examine the advancement and distortion effects of the pulse-on-background method, we have performed experiments for various conditions using the setup illustrated in Fig. 4.4. We use a 980-nm diode laser as the pump source, and the dashed box in Fig. 4.4 represents two types of signal source systems prepared for the cases of mutually coherent and incoherent background fields. Two percent of the signal beam intensity is split off for use as a reference, while the rest is sent into an erbium doped fiber (EDF). The pump beam at 980 nm and the signal beam at 1550 nm are combined in a wavelength division multiplexer (WDM) and co-propagate through the EDF. The output pulse is measured after filtering out the pump using another WDM. In the following two sections, we show experimental results of the pulse-on-background method for various conditions.

In Fig. 4.4(a), a tunable diode laser operates at a wavelength of 1550 nm and the laser light is sent through an electro-optic modulator (EOM). When an electric field applied to the crystal in the EOM is changed, the Pockels effect alters the polarization of the laser light exiting the EOM [111], and the polarizer after the EOM turns the polarization modulation into an amplitude modulation. The applied voltage is
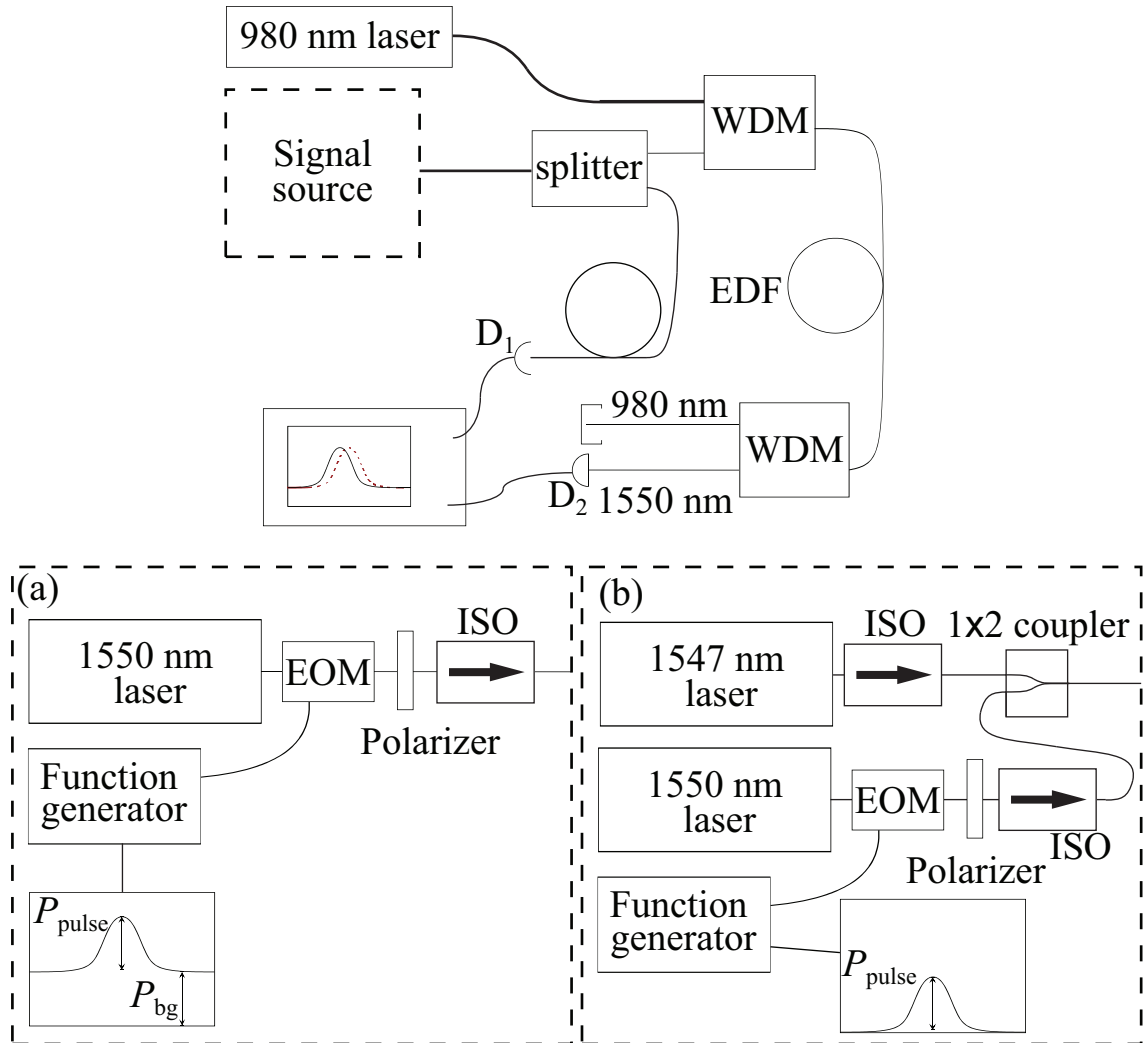
Figure 4.4: Experimental setup and signal source systems for (a) mutually coherent background and (b) mutually incoherent background fields.

driven by a function generator to generate a Gaussian pulse on a variable-intensity background. P_{pulse} and P_{bg} represent the power of the pulse and the background. Then the signal beam is sent through an isolator and coupled into a fiber. In this signal source system, the pulse and the background are mutually coherent. Fig. 4.4(b) shows the signal source system whose pulse and background are mutually incoherent. The voltage applied to the EOM is controlled to generate a pulse on no background, and another diode laser operating at 1547 nm is used as the source of the CW background. The pulse and the background are combined at a 1×2 fiber coupler and sent to the splitter.

4.6 Results for coherent background

To characterize pulse-width distortion, which includes pulse broadening and compression, we define the pulse-width ratio as the ratio of the full width at half maximum (FWHM) of the output pulse to the input pulse FWHM ($\tau_{\text{out}}/\tau_{\text{in}}$). Another important parameter is the background-to-pulse power ratio ($P_{\text{bg}}/P_{\text{pulse}}$). In Fig. 4.5(a), we plot the pulse-width ratio against the background-to-pulse power ratio for various input pulse widths. The horizontal line at the pulse-width ratio of 1 represents no pulse-width distortion. The pump power P_{pump} and pulse power P_{pulse} are 35 mW and 55 μW, respectively, and the average inversion level $(N_2 - N_1)/N_2 = 0.9$, where N_2 and N_1 are the number density of erbium ions in the EDFA in the metastable and ground states, respectively. Under our experimental conditions, pulse-width ratios between

0.84 and 1.43 were observed for different pulse widths and background-to-pulse power ratios. The experimental results are well described by the numerical model. Further, fractional advancement, the ratio of pulse advancement to input pulse FWHM, was found to be independent of the power ratio as shown in Fig. 4.5(b). Therefore we conclude that the power ratio can be used as a free parameter to minimize the pulse
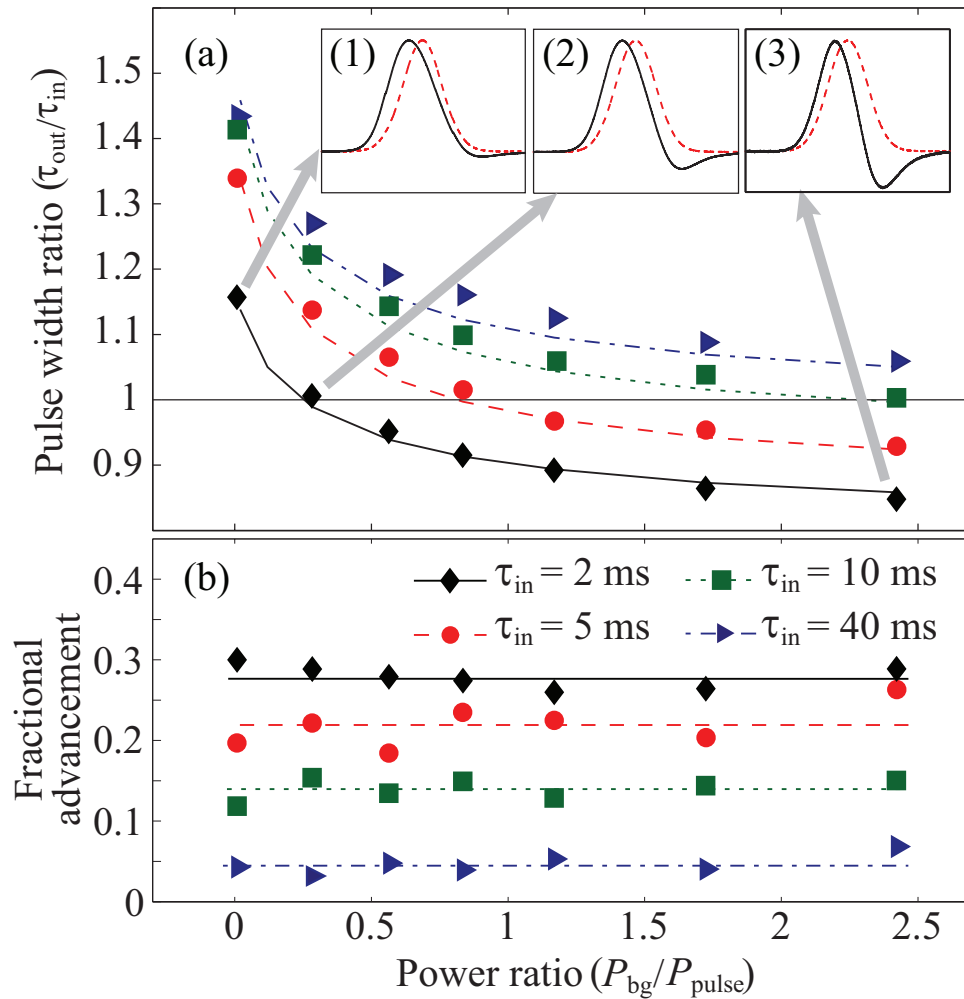

Figure 4.5: (a) Experimentally measured (symbols) and theoretically predicted (lines) pulse-width ratio vs. background-to-pulse power ratio for different pulse widths. (b) Experimentally measured fractional advancement vs. background-to-pulse power ratio, with best-fit horizontal lines showing average advancement.

distortion without changing the fractional advancement. The output pulse width is equal to the input pulse width when the background-to-pulse power ratio is about 0.3, 0.8, and 2.4 for pulse widths of 2 ms, 5 ms, and 10 ms, respectively.

In addition, the time traces of the input (dashed curve) and output (solid curve) pulse for 2-ms pulse width are shown in insets (1), (2), and (3) of Fig. 4.5 at power ratios of 0, 0.8 and 2.5, respectively. Pulse broadening due to the gain recovery effect occurs at low background-to-pulse power ratio as shown in inset (1), while inset (3) illustrates that a higher background-to-pulse power ratio is associated with a smaller gain recovery effect and larger pulse spectrum broadening, resulting in a tendency towards pulse compression. Furthermore, the broadening effect for a 2-ms pulse width is weaker than that for longer pulse widths, since the pulse tail exits the material too quickly to experience the recovered gain. Note that the input and output pulse widths are equal for a background-to-pulse power ratio of 0.3 as shown in inset (2), which indicates that the pulse-width distortion is eliminated by controlling the power ratio.

Even though the pulse-width distortion is removed, the trailing edge of the pulse in inset (2) of Fig. 4.5 experiences additional pulse-shape distortion. The degree of this distortion can be characterized by the quantity [77]

$$
\begin{aligned}
D &= \left(\frac{\int_{-\infty}^{+\infty} ||E'(t+\Delta t)|^2 - |E(t)|^2|dt}{\int_{-\infty}^{+\infty} |E'(t+\Delta t)|^2} \right)^{\frac{1}{2}} \\
&\quad - \left(\frac{\int_{-\infty}^{+\infty} ||E(t+\delta t)|^2 - |E(t)|^2|dt}{\int_{-\infty}^{+\infty} |E(t+\delta t)|^2} \right)^{\frac{1}{2}}
\end{aligned} \tag{4.7}
$$

where $E'(t)$ and $E(t)$ are the normalized output and input field envelopes, respectively, Δt is the time advancement of the pulse, and δt is the temporal resolution of our detection system. The first term represents the distortion caused by pulse reshaping, and the second term is a measure of noise. Noise was eliminated from the pulse-shape distortion by subtracting the reference power from the same reference power which is shifted in time by the temporal resolution of our detection system δt.

Figure 4.6 shows a distinct pattern in both the experimental and numerical data. At low power ratios, the primary source of distortion is pulse broadening associated with gain recovery, leading to the behavior shown in inset (1) of Fig. 4.5. However, once the power ratio becomes higher than the minimum distortion point, pulse com-

Figure 4.6: Experimentally measured (symbols) and theoretically predicted (lines) pulse-shape distortion vs. background-to-pulse power ratio for different pulse widths.

pression becomes the dominant contribution to the distortion, leading to the behavior

shown in inset (3) of Fig. 4.5. To emphasize the possibility of reducing pulse-shape

distortion, time traces of the input and output pulse for 10-ms pulse widths at power

ratios of 0 and 1.2 are shown in insets (1) and (2) of Fig. 4.6. Note that the 10-ms

output pulse at zero power ratio shows a stronger pulse broadening effect than that

of the 2-ms pulse in inset (1) of Fig. 4.5. In addition, the input and output pulse

shapes at a power ratio of 1.2, which is approximately the minimum distortion point,

show pulse advancement with little distortion. Thus, proper selection of the power

ratio for a particular pulse width can reduce pulse distortion.

Furthermore, we investigated the dependence of pulse distortion on pump power

because the process of gain recovery depends on the pump power. The pulse power
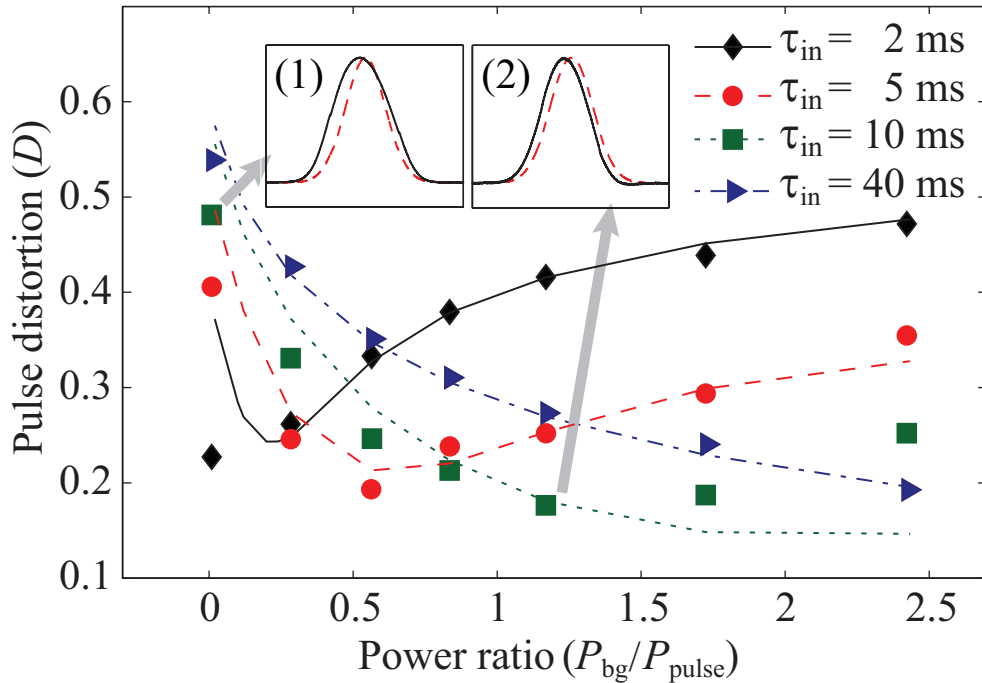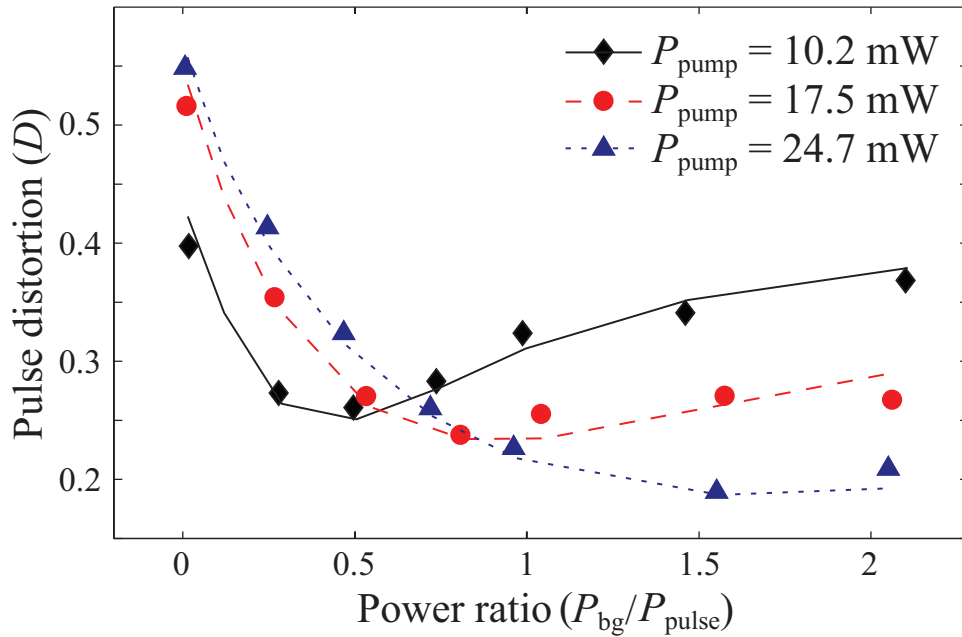

Figure 4.7: Experimentally measured (symbols) and theoretically predicted (lines) pulse distortion vs. background-to-pulse power ratio for different pump powers.

and the pulse width were held fixed at 80 μW and 10 ms, respectively, while the average inversion level was about 0.86, 0.79, and 0.54 for the pump powers of 10.2 mW, 17.5 mW, and 24.7 mW, respectively. These results are shown in Fig. 4.7. The gain recovery becomes stronger if the pump power increases, and it compensates for the pulse spectrum broadening at the higher background-to-pulse power ratios. The fractional advancement of a Gaussian pulse of 10-ms pulse width is largest when the pump power is 17.5 mW, agreeing very well with reference [40], and has no significant dependence on the power ratio.

Next, we investigate the pulse-power dependence of the fractional advancement and pulse-shape distortion using a Gaussian pulse of 10-ms duration on no background

Figure 4.8: Experimentally measured pulse-shape distortion (left axis) and fractional advancement (right axis) versus pulse power, with no background. The curves are guides for the eye.

to choose the optimum pulse power. In Fig. 4.8, we plot the pulse-shape distortion and the fractional advancement against the pulse power. As the pulse power increases, the pulse-shape distortion also increases but saturates around a pulse power of 0.3 mW. The fractional advancement has its maximum value at the 0.37-mW pulse power and then decreases slowly. In inset (1) of Fig. 4.8, at low pulse power (0.01 mW), the pulse is shifted and broadened by the gain-recovery effect. At high pulse power (0.9 mW) as shown in inset (2) of Fig. 4.8, the output pulse becomes substantially broadened because the pulse peak is amplified much less than the leading edge of the pulse due to the saturated gain. Therefore, under our experimental conditions, the pulse of 0.37-mW pulse power is expected to have the maximum fractional advancement if we add a background of appropriate power.

Finally, we investigate the pulse-power dependence of the pulse-on-background method, performing experiments and computer simulations using the methods described previously. Using a single laser modulated by an EOM, we generate Gaussian pulses of 10-ms duration with various pulse and background powers. In Fig. 4.6 and 4.7, we sent a pulse of power of $55 - 80 \mu$ W through an EDFA and showed that fractional advancement is independent of the background-to-pulse power ratio. More careful investigation, however, has been performed and shows that pulse advancement depends on pulse power as shown in Fig. 4.9(a). With increasing power ratio, pulse advancement increases for a pulse power of 50 μW, is maintained for a power of 100 μW (similar to the power used in our previous results), and decreases for pulse

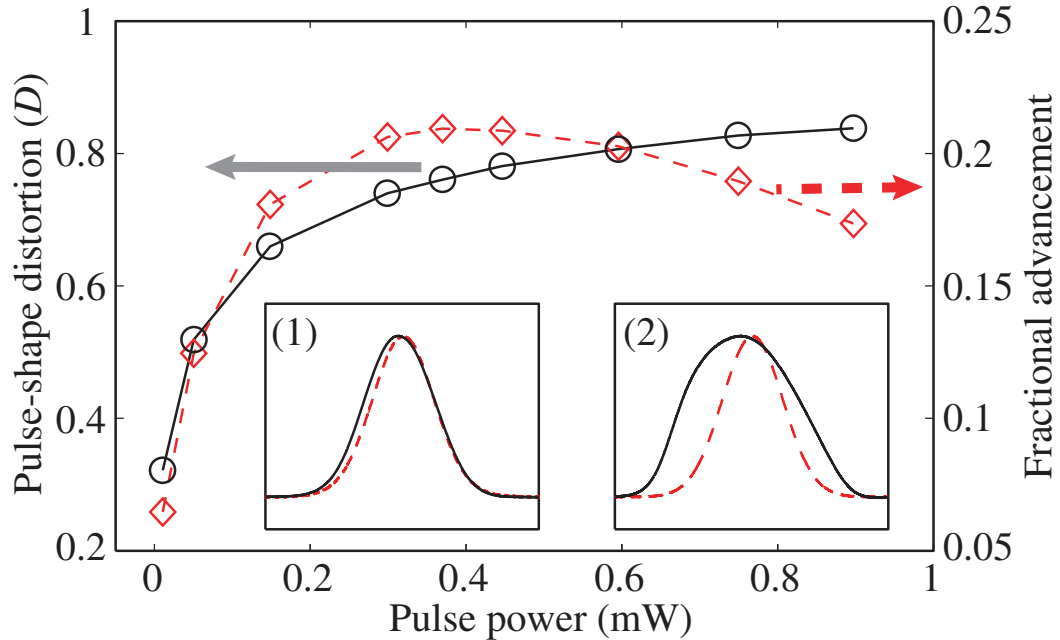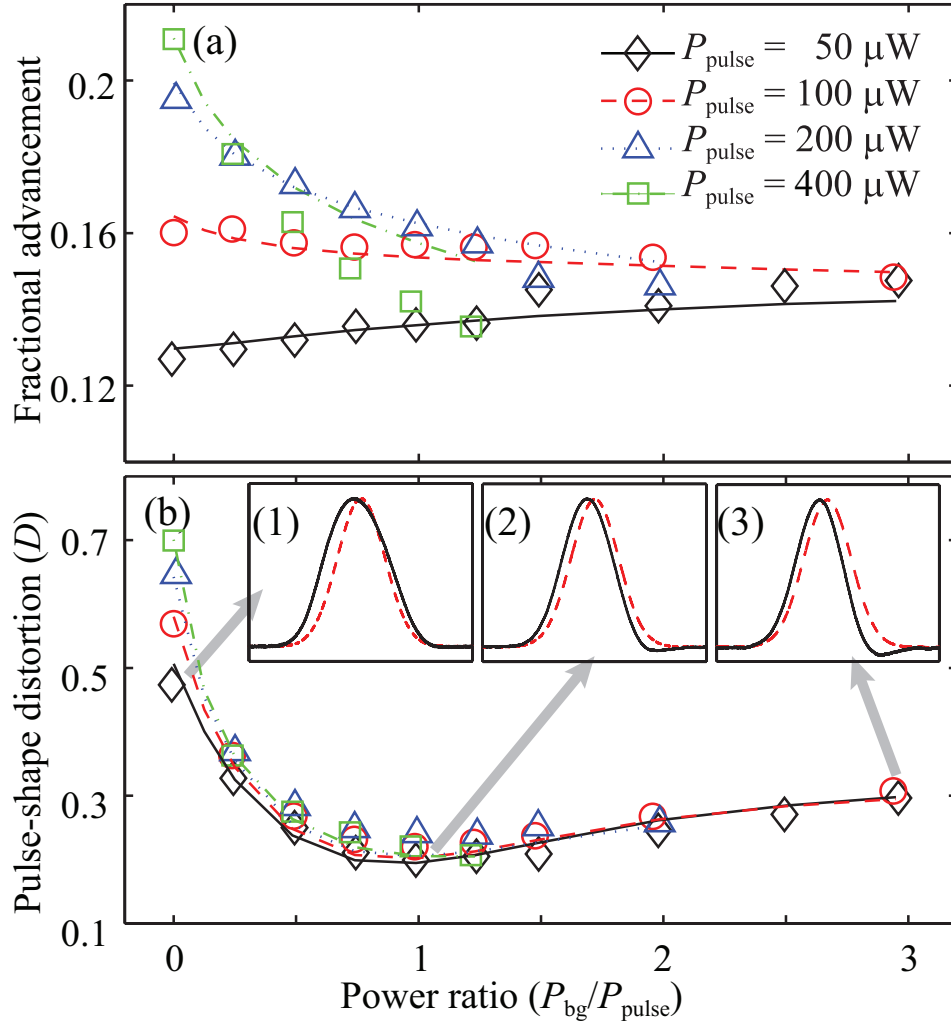Figure 4.9: (a) Experimentally measured (symbols) and theoretically predicted (curves) fractional advancement versus background-to-pulse power ratio for different pulse powers. (b) Experimentally measured (symbols) and theoretically predicted (curves) pulse-shape distortion versus background-to-pulse power ratio.

powers of 200 μW and higher. As shown in Fig. 4.9, experiment and theory match well except the case for pulse power of 400 μW which is very high power in our system. According to reference [80], as the background power increases, the spectral hole induced by CPO becomes deeper at low background power, maintains its line shape at middle power, and becomes broad and shallow at high power. Therefore, the group

index related to the line shape of the spectral hole increases at low background power, is conserved at middle power, and decreases at high power. On the other hand, the pulse-shape distortion against the background-to-pulse power ratio does not depend on the pulse power except at low power ratios as shown in Fig. 4.9(b). The pulse broadening and compression associated with gain recovery and pulse spectrum broadening are shown in inset (1) and (3) of Fig. 4.9(b), respectively. Under our present experimental conditions, the pulse-shape distortion has the minimum value of ∼0.2 at power ratio of 1 as shown in inset (2) of Fig. 4.9(b). Finally, we could reduce the pulse-shape distortion from 0.56 to 0.21 (56%) while the fractional advancement maintains its values at about 0.16 (3%) for pulse power of 100 μW.

4.7 Results using mutually incoherent background

In the previous section, we observed that the pulse distortion and advancement depend on the pump power, background-to-pulse power ratio, and pulse width as well as pulse power through an erbium-doped fiber amplifier. In this section, we implement the POB method using separate, mutually incoherent lasers to generate the pulse and background field.

In many systems, it is more convenient to use a separate laser for generating the background field than to use a single laser with an EOM, and in this case the background field and pulse are generally incoherent with each other. When the signals are, for instance, return-to-zero pulses, adding the background field from another laser

is more convenient than modifying the signals with a modulator. If we assume that the dipole dephasing time τ_{32} of the material system is much smaller than the ground state recovery time τ_{21} and the inverse of the detuning frequency (or modulation frequency) Δ [81], the CPO effect is sensitive only to intensity modulation of the incident laser power. In this case, a background field incoherent to the pulse should have the same properties as a coherent background field in the POB method. To prove this, we performed experiments using the methods described in Section 4.5 with signal system (b) in Fig. 4.4. A Gaussian pulse of 10-ms duration and 60-μW pulse power on no background at a wavelength of 1550 nm is generated using an EOM and a polarizer, another CW laser is used for background power at 1547 nm, they are combined at an 1×2 fiber coupler, and they co-propagate. The pump power P_{pump} was fixed at 17.5 mW, inducing an average inversion level of $(N_2 - N_1)/N_2 = 0.79$.

In Fig. 4.10, we plot the pulse-shape distortion and the fractional advancement against the background-to-pulse power ratio $P_{\text{bg}}/P_{\text{pulse}}$ for coherent and incoherent background fields. As shown in Fig. 4.10, at low (and high) power ratios, the gain recovery (and pulse spectrum broadening) effect induces the pulse-shape distortion, having a minimum value at a power ratio of about 1. Note that the the POB method operates identically within experimental error in both background cases. Therefore, the POB method provides one more degree of freedom for reducing pulse distortion in fast-light propagation through an erbium-doped fiber amplifier.
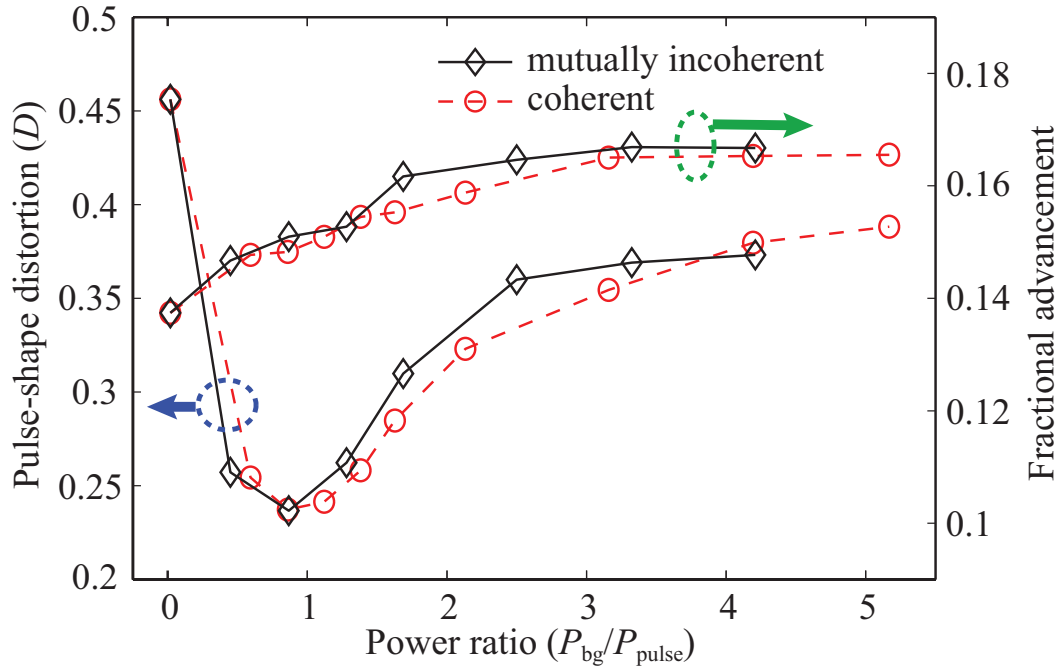
Figure 4.10: Experimentally measured pulse-shape distortion (left axis) and fractional advancement (right axis) versus background-to-pulse power ratio for coherent (circles) and mutually incoherent (diamonds) background fields to the pulse. The curves are guides for the eye.

4.8 Summary

In conclusion, we studied pulse propagation in an erbium doped fiber amplifier with a negative group velocity produced by coherent population oscillations, and we suggested a new method to reduce pulse-shape distortion induced by anomalous dispersion. When a pulse superposed on a CW background propagates through an EDFA, either pulse broadening or pulse compression can be observed. These results can be interpreted by examining the competing mechanisms of gain recovery and pulse spectrum broadening.

Numerical calculation of the 5-level-system rate equations for erbium ions was

performed to model pulse propagation in an EDFA, and the computer simulation took amplified spontaneous emission and excited state absorption into account. The distortion of the pulse shape caused by the two competing effects depends on input pulse width as well as pulse power, pump power, and background-to-pulse power ratio. With the proper choice of these parameters, we obtained significant pulse advancement with minimal pulse distortion. We also showed that comparable distortion reduction can be obtained through use of a mutually incoherent background field, a procedure that could be much more readily implemented under many circumstances than adding a coherent background field.

The EDFA has a CPO response time of 10 ms, which is too slow for applications in telecommunication. However, this long response time facilitates our characterization of the properties of the CPO process that we report here. We believe that the techniques we report here for minimizing pulse distortion can be applied to other CPO systems that display much faster response [44, 112, 113, 114].

Chapter 5

Conclusions and Discussion

In this thesis, I described my theoretical and experimental studies on two topics in the area of nonlinear optics. The first topic is interferometric spatial fringe patterns showing superresolution. In this research, I studied means to achieve an enhancement of spatial interference resolution over the classical Rayleigh limit through the use of nonlinear and quantum optical methods. In the second topic, I suggested and demonstrated a new procedure for fast-light pulse-distortion management which is caused by coherent population oscillations.

In the first part of this thesis, classical standard interference fringe pattern was described by quantum mechanics using photon operators and two-dimensional matrices representing individual optical elements. This method was extended to describe nonlinear interference patterns recorded on a material responding to multi-photon absorption using classical states of light. The theory indicates that the nonlinear

interference patterns has the narrower feature sizes than standard patterns, but with a spatial resolution identical to standard patterns. In addition, quantum lithography recorded by a quantum-state light on a multi-photon absorbing material was studied, showing that quantum interferometry generates even narrower feature than the nonlinear interference pattern while keeping a high visibility. The greatest advantage of nonlinear interferometry and quantum interferometry is its ability to enhance resolution of the interference pattern.

A nonlinear optical, phase-shifted-grating method for improving the resolution of feature sizes was implemented experimentally using an N-photon lithographic material. High spatial confinement of multi-photon interaction is caused by the nonlinear material's response, so that a photo-reaction only occurs in a smaller volume than the light intensity distribution, causing a narrowing of features within the interference pattern. Using this nonlinear photo-reaction, the phase-shifted-grating method was proposed by Bentley and Boyd. An M-fold enhancement in resolution compared to a normal interferometric lithography can be achieved by exposing an N-photon absorber M times and adjusting the phase difference between the two recording beams after each exposure. High visibility fringe patterns can be achieved for the case where the value of N is much larger than that of M. Moreover, for various combinations of phase shifts between the two arms of the interferometer, various non-sinusoidal patterns can be recorded. The field amplitude of each exposure is an additional free parameter for varying the shape of interference patterns as well. If each exposure has

different energy with controllable phase shift, arbitrary patterns can be obtained.

An experimental demonstration of the phase-shifted-grating method was performed using poly(methyl-methacrylate) (PMMA) which is a UV lithographic material. As the first step, linear and nonlinear optical properties of PMMA were examined. The linear absorption spectrum shows that PMMA is a transparent plastic passing visible light and strongly absorbing light in the ultraviolet region near 216 nm and 260 nm. In addition, experimental dosimetry was performed to verify the multi-photon nature of absorption in PMMA by recording interference patterns on a PMMA film for various recording pulse energies. The experimental result shows that the slope of the fitted line is about -3.7 indicating that PMMA is a three- and four-photon absorber at a wavelength of 800 nm. Then, we irradiated the sample with a single pulse with a pulse energy of 130 μJ to observe a standard interference pattern recorded on a multi-photon absorption material. The recorded fringe pattern has a period of 425 nm, which is close to the classical Rayleigh limit of $\lambda/2$. To enhance the resolution of the fringes, we irradiated the sample twice in sequence with a phase shift of π introduced for the second exposure. The measured AFM image shows that the period was reduced to 213 nm which is about a quarter of the wavelength of the recording light, indicating that we achieved a resolution that exceeds the Rayleigh limit at grazing angle by a factor of two. We also obtained a three-fold enhancement of resolution by irradiating three exposures in sequence with phase shifts of $2\pi/3$ and $4\pi/3$ for the second and third exposures, respectively. Non-sinusoidal patterns were

also experimentally obtained by using non-uniform phase shifts between exposures. As far as we know, this is the first experimental demonstration of spatial resolution enhancement by the phase-shifted grating method using a real lithographic material.

Quantum lithography (QL) was proposed to obtain superresolution of spatial interference pattern using multi-photon absorption and the quantum $N00N$ states of photons, but it has not been realized due to low multi-photon absorption efficiency. Recently, the optical centroid measurement (OCM) method was proposed for achieving spatial interferometric superresolution with much higher detection efficiency than that of quantum lithography. Instead of using a detector array whose pixels respond to multi-photon absorption as in QL, an array of single-photon detectors followed by postprocessing is used. The locations of the N detectors that fire in response to N incident photons are determined, and the centroid of the positions of those detectors is computed. A histogram of the positions of optical centroids determined by repeated measurements is then produced.

Theory predicts that this histogram will have resolution enhancement as much as QL, but with much higher detection efficiency. An analysis based on the use of combinatorics was also presented to provide an intuitive understanding of the tradeoffs between the QL and OCM methods, and we suggested the use of a photon-number-resolving detector array to eliminate the loss of efficiency due to multi-arrivals at one pixel. Experimental demonstration was performed for two-photon interference for both the QL and OCM methods. The two detection systems were prepared using

multimode fibers (MMFs). For the QL case, a two-photon detector was mimicked by dividing the output of a single MMF into two additional MMFs monitored by two single-photon detectors operating in coincidence. The input of the MMF was scanned using a motorized translation stage in discrete steps while recording the photon counts. For the OCM case, the optical centroid position of two photons arriving at spatially separated two MMFs is located at the mean position of two fibers. We prepared several two-fiber systems having centroid at same position for various separations between them, and accumulation of the coincidence count rates at same centroid position measured the marginal probability distribution of optical centroid. The experimental results show that both QL and OCM have a resolution enhancement by a factor of two but the OCM method is more efficient than the QL method. Finally, we succeeded to achieve quantum spatial super-resolution by the OCM method showing an interference fringe pattern with 2-fold enhanced resolution. In addition, we achieved phase four-photon interference patterns by varying the phase of one arm of the interferometer, and this result indicates that multi-photon effects can be measured by using spatially separated detectors like the OCM detectors not by using multi-photon absorbing detectors. We feel that the OCM method will be a powerful means of providing still greater enhancement in resolution with large arrays of single-photon detectors. This is the first proof-of-principle experiment of the OCM method of quantum interference patterns.

In the second topic, the pulse-on-background method is studied for minimizing

pulse distortion induced by the fast-light propagation through an erbium doped fiber amplifier (EDFA). Anomalous dispersion produced by coherent population oscillations can induce fast-light pulse propagation, but it also produces pulse distortion. First, the mechanisms of pulse broadening and pulse compression in an erbium doped fiber amplifier are introduced. If the input pulse duration is long enough, the "gain recovery" effect broadens the pulse by adding energy to its trailing edge. Meanwhile, if the input is superimposed on a background, a gain spectral hole can be induced, and then the "pulse spectrum broadening" effect compresses the output pulse. By controlling these two competing mechanisms, we can reduce the pulse-width distortion and pulse-shape distortion.

To model our experimental observations, we performed computer simulations of pulse propagation through the EDFA by numerically solving the 5-level-system rate equations for erbium ions including amplified spontaneous emission. Furthermore, the pulse-on-background method was performed using an erbium doped fiber amplifier. The degree of the pulse-shape distortion can be characterized by the quantity D and was measured by varying the power of background for various experimental conditions. The experimental results show that the pulse-shape distortion depends on input pulse width as well as pulse power, pump power, and background-to-pulse power ratio. With the proper choice of these parameters, we obtained significant pulse advancement with minimal pulse distortion. We also showed that comparable distortion reduction can be obtained through use of a mutually incoherent background field, a

procedure that could be much more readily implemented under many circumstances.

We believe that the pulse-on-background technique for minimizing pulse distortion

can be applied to other CPO systems that display much faster response.

Bibliography

[1] R. W. Boyd, *Nonlinear Optics*, 2nd ed. (Academic Press, New York, 2003).

[2] V. Giovannetti, S. Lloyd, and L. Maccone, "Quantum Metrology," Phys. Rev. Lett. **96**, 010401 (2006).

[3] D. Gabor, "Microscopy by recorded wavefronts," Proc. R. Soc. Lond. A **197**, 454 (1949).

[4] A. N. Boto, P. Kok, D.S. Abrams, S. L. Braunstein, C.P. Williams, and J.P. Dowling, "Quantum interferometric optical lithography: Exploiting entanglement to beat the diffraction limit," Phys. Rev. Lett. **85**, 2733 (2000).

[5] V. Vali and R. W. Shorthill, "Fiber ring interferometer," Appl. Opt. **15**, 1099 (1976).

[6] A. A. Michelson and F. G. Pease, "Measurement of the diameter of alpha Orionis with the interferometer," Astrophysical J. **53**, 249 (1921).

[7] http://www.ligo.caltech.edu/

[8] A. F. Fercher, "Ophthalmic interferometry," Proceedings of the International Conference on Optics in Life Sciences, 221 (1990).

[9] S. R. J. Brueck, S. H. Zaidi, X. Chen, and Z. Zhang, "Interferometric lithography from periodic arrays to arbitrary patterns," Microelectron. Eng. **42**, 145-148 (1998).

[10] P. Kok, A. N. Boto, D. S. Abrams, C. P. Williams, S. L. Braunstein, and J. P. Dowling, "Quantuminterferometric optical lithography: Towards arbitrary two-dimensional patterns," Phys. Rev. A **63**, 063407 (2001).

[11] G. Björk, L.L. Sánchez-Soto, and J. Söderholm, "Entangled-state lithography: Tailoring any pattern with a single state," Phys. Rev.Lett. **86**, 4516-4519 (2001).

[12] C. J. Schwarz, Y. Kuznetsova, and S. R. J. Brueck, "Imaging interferometric microscopy," Opt. Lett. **28**, 1424 (2003).

[13] Q. Sun, P. R. Hemmer, and M. S. Zubairy, "Quantum lithography with classical light: Generation of arbitrary patterns," Phys. Rev. A **75**, 065803 (2007).

[14] H. S. Park, S. K. Lee, and J. Y. Lee, "Generation of super-resolution atomic state density distribution based on temporallycascaded multiple light exposures," Opt. Express, **16**, 21982 (2008)

[15] Lord Rayleigh, "Investigations in optics with special reference to the spectroscope," Phil. Mag. **8**, 261-274 (1879).

[16] T. Ito and S. Okazaki, "Pushing the limits of lithography," Nature **406**, 1027 (2000).

[17] H. Ooki, M. Komatsu, and M. Shibuya, "A Novel Super-Resolution Technique for Optical LithographyNonlinear Multiple Exposure Method," Jpn. J. Appl. Phys. **33**, L177 (1994).

[18] E. Yablonovitch and R. B. Vrijen, "Optical projection lithography at half the Rayleigh resolution limit by two-photon exposure," Opt. Eng. **38**, 334 (1999).

[19] D. V. Korobkin and E. Yablonovitch, "Twofold spatial resolution enhancement by two-photon exposure of photographic film," Opt. Eng. **41**, 1729 (2002).

[20] K. Wang and D.-Z. Cao, "Subwavelength coincidence interference with classical thermal light," Phys. Rev. A **70**, 041801(R) (2004).

[21] S. J. Bentley and R. W. Boyd, "Nonlinear optical lithography with ultra-high sub-Rayleigh resolution," Opt. Express **12**, 5735 (2004).

[22] R. W. Boyd and S. J. Bentley, "Recent progress in quantum and nonlinear optical lithography," J. Mod. Opt. **53**, 713 (2006)

[23] G. Khoury, H. S. Eisenberg, E. J. S. Fonseca, and D. Bouwmeester, "Nonlinear Interferometry via Fock-State Projection," Phys. Rev. Lett. **96**, 203601 (2006).

[24] P. R. Hemmer, A. Muthukrishnan, M. O. Scully, and M. S. Zubairy, "Quantum Lithography with Classical Light," Phys. Rev. Lett. 96, 163603 (2006)

[25] M. Kiffner, J. Evers, and M. S. Zubairy, "Resonant Interferometric Lithography beyond the Diffraction Limit," Phys. Rev. Lett. 100, 073602 (2008).

[26] H. Li, V. A. Sautenkov, M. M. Kash, A. V. Sokolov, G. R. Welch, Y. V. Rostovtsev, M. S. Zubairy, and M. O. Scully, "Optical imaging beyond the diffraction limit via dark states," arXiv: quant-ph/0803.2557v1 (2008).

[27] L. Brillouin, "Wave propagation and group velocity," Academic Press, New York, (1960).

[28] 17th CGPM, Resolution 1, CR, 97 (1983) and Metrologia, 20, 25 (1984)

[29] Lord Rayleigh, Proc. London Math. Society **IX**, 21 (1877).

[30] C. G. B. Garrett and D. E. McCumber, "Propagation of a Gaussian Light Pulse through an Anomalous Dispersion Medium," Phys. Rev. A, **1**, 305 (1970).

[31] S. Chu and W. Wong, "Linear pulse propagation in an absorbing medium," Phys. Rev. Lett. **48**, 738 (1982)

[32] B. Segard and B. Macke, "Observation of negative velocity pulse propagation," PHYS. LETT. A **109A**, 203 (1985).

[33] S. P. Tewari and G. S. Agarwal, "Control of phase matching and nonlinear generation in dense media by resonant field," Phys. Rev. Lett. **56**, 1811 (1986).

[34] S. E. Harris, J. E. Field, and A. Imamoglu, "Nonlinear optical processes using electromagnetically induced transparency," Phys. Rev. Lett. **64**, 1107 (1990).

[35] A. Kasapi, M. Jain, G. Y. Yin, and S. E. Harris, "Electromagnetically Induced Transparency: Propagation Dynamics," Phys. Rev. Lett. **74**, 2447 (1995).

[36] L. V. Hau, S. E. Harris, Z. Dutton, and C. H. Behroozi, "Light speed reduction to 17 metres per second in an ultracold atomic gas," Nature **397**, 594 (1999)

[37] A. V. Turukhin, V. S. Sudarshanam, M. S. Shahriar, J. A. Musser, B. S. Ham, and P. R. Hemmer, "Observation of Ultraslow and Stored Light Pulses in a Solid," Phys. Rev. Lett. **88**, 023602 (2002).

[38] M. S. Bigelow, N. N. Lepeshkin,and R. W. Boyd, "Observation of Ultraslow Light Propagation in a Ruby Crystal at Room Temperature," Phys. Rev. Lett. **90**, 113903 (2003).

[39] M. S. Bigelow, N. N. Lepeshkin,and R. W. Boyd, "Superluminal and Slow Light Propagation in a Room-Temperature Solid," Science **301**, 200 (2003).

[40] A. Schweinsberg, N. N. Lepeshkin, M. S. Bigelow, R. W. Boyd and S. Jarabo, "Observation of superluminal and slow light propagation in erbium-doped optical fiber," Europhys. Lett., **73**, 218 (2006).

[41] Y. Okawachi, M.S. Bigelow, J.E. Sharping, Z. Zhu, A. Schweinsberg, D.J. Gauthier R.W. Boyd, and A.L. Gaeta, "Tunable All-Optical Delays via Brillouin Slow Light in an Optical Fiber," Phys. Rev. Lett. **94**, 153902 (2005).

[42] Q. Xu, S. Sandhu, M. L. Povinelli, J. Shakya, S. Fan, and M. Lipson, "Experimental Realization of an On-Chip All-Optical Analogue to Electromagnetically Induced Transparency," Phys. Rev. Lett. **96**, 123901 (2006).

[43] 8. Y. Okawachi, M. A. Foster, J. E. Sharping, and A. L. Gaeta, Q. Xu, and M. Lipson, "All-optical slow light on a photonic chip," Opt. Express **14** , 2317 (2006).

[44] J. Mørk, R. Kjær, M. van der Poel, L. Oxenløwe, and K. Yvind, "Slow light in semiconductor waveguide at gigahertz frequencies," Opt. Express **13**, 8136 (2005).

[45] A.V. Uskov and C. J. Chang-Hasnain, "Slow and superluminal light in semiconductor optical amplifiers," Electron. Lett. **41**, 55 (2005).

[46] R. W. Boyd, D. J. Gauthier, and A. L. Gaeta, "Applications of Slow Light in Telecommunications," Optics and Photonics News **April**, 44 (2006).

[47] R. W. Boyd and D. J. Gauthier, "Transparency on an optical chip," Nature **441**, 701 (2006).

[48] K. Y. Song, M. Gonzalez Herraez, and L. Thevenaz, "Gain-assisted pulse advancement using single and double Brillouin gain peaks in optical fibers," Opt. Express **13**, 9758 (2005).

[49] M. D. Stenner, M. A. Neifeld, Z. Zhu, A. M. C. Dawes, and D. J. Gauthier, "Distortion management in slow-light pulse delay," Opt. Express **13**, 9995 (2005).

[50] J. B. Khurgin, "Performance limits of delay lines based on optical amplifiers," Opt. Lett. **31**, 948 (2006).

[51] A. Minardo, R. Bernini, and L. Zeni, "Low distortion Brillouin slow light in optical fibers using AM modulation," Opt. Express **14**, 5866 (2006)

[52] Z. Shi, R. Pant, Z. Zhu, M. D. Stenner, M. A. Neifeld, D. J. Gauthier, and R. W. Boyd, "Design of a tunable time-delay element using multiple gain lines for increased fractional delay with high data fidelity," Opt. Lett. **32**, 1986 (2007).

[53] R. Pant, M. D. Stenner, M. A. Neifeld, Z. Shi, R. W. Boyd, and D. J. Gauthier, "Maximizing the opening of eye diagrams for slow-light systems," Appl. Opt. **46**, 6513 (2007).

[54] R. Pant, M. D. Stenner, M. A. Neifeld, and D. J. Gauthier, "Optimal pump profile designs for broadband SBS slow-light systems," Opt. Express **16**, 2764 (2008)

[55] T. Schneider, A. Wiatreck, and R. Henker, "Zero-broadening and pulse compression slow light in an optical fiber at high pulse delays," Opt. Express **16**, 15617 (2008)

[56] R. M. Camacho, M. V. Pack, and J. C. Howell, "Low-distortion slow light using two absorption resonances," Phy. Rev. A **73**, 063812 (2006)

[57] A. Kolkiran and G. S. Agarwal, "Quantum interferometry using coherent beam stimulated parametric down-conversion," Opt. Express **16** 6479 (2008).

[58] M. Goppert-Mayer, "ber Elementarakte mit zwei Quantensprngen," Ann. Phys. **9**, 273 (1931).

[59] W. Kaiser and C. G. B. Garrett, "Two-Photon Excitation in CaF2: Eu^{2+}," Phys. ReV. Lett. **7**, 229 (1961).

[60] G. S. He, L. Tan, Q. Zheng, and P. N. Prasad, "Multiphoton Absorbing Materials: Molecular Designs, Characterizations, and Applications," Chem. Rev. **108**, 1245 (2008).

[61] J. B. Shear, E. B. Brown, and W. W. Webb, "Multiphoton-Excited Fluorescence of Fluorogen-Labeled Neurotransmitters," Anal. Chem. **68**, 1778 (1996).

[62] E. W. Van Stryland, H. Vanherzeele, M. A. Woodall, M. J. Soileau, A. L. Smirl, S. Guha, T. F. Boggess, "Two photon absorption, nonlinear refraction and optical limiting in semiconductors," Optical Eng. **24**, 613 (1985).

[63] N. G. Basov, A. Z. Grasyuk, I. G. Zubarev, and V. A. Katulin, "GaAs under two-photon optical excitation of neodymium glass laser emission," JETP Lett. **1**, 118 (1965).

[64] W. Denk, J. H. Strickler, W. W. Webb, "Two-Photon Laser Scanning Fluorescence Microscopy," Science **248**, 73 (1990).

[65] D. A. Parthenopoulos, P. E. Rentzepis, "Three-dimensional optical storage memory," Science **245**, 843 (1989); D. A. Parthenopoulos, P. E. Rentzepis, " Two-photon volume information storage in doped polymer systems," J. Appl. Phys. **68**, 5814 (1990).

[66] K. D. Belfield, K. J. Schafer, Y. Liu, J. Liu, X. Ren and E. W. Van Stryland, "Multiphoton-absorbing organic materials for microfabrication, emerging optical applications and non-destructive three-dimensional imaging," J. Phys. Org. Chem. **13**, 837 (2000).

[67] S. Kawata, H.-B. Sun, T. Tanaka, and K. Takada, "Finer features for functional microdevices," Nature **412**, 697 (2001).

[68] D. N. Klyshko, "Scattering of light in a medium with nonlinear polarizability," Zh. Eksp. Teor. Fiz. **55**, 1006 (1968) [English translation in Sov. Phys. JETP **28**, 522 (1969)].

[69] D. C. Burnham and D. L. Weinberg, "Observation of Simultaneity in Parametric Production of Optical Photon Pairs," Phys. Rev. Lett. **25**, 84 (1970).

[70] R. Horodecki, P. Horodecki, M. Horodecki, and K. Horodecki, "Quantum entanglement," Rev. Mod. Phys. **81**, 865 (2009).

[71] C. K. Hong, Z. Y. Ou, and L. Mandel, "Measurement of subpicosecond time intervals between two photons by interference," Phys. Rev. Lett. **59**, 2044 (1987).

[72] H. Lee, P. Kok, and J. P. Dowling, "A quantum Rosetta stone for interferometry," J. Mod. Opt. **49**, 2325 (2002).

[73] Z. J. Ou, *Multi-Photon Quantum Interference.* (Springer, New York, 2007).

[74] G. Nimtz and A. Haibel, "Basics of superluminal signals," Ann. Phys. **11**, 163 (2002).

[75] M. D. Stenner, D. J. Gauthier, and M. A. Neifeld, "The speed of information in a 'fast-light' optical medium," Nature **16**, 425 (2003).

[76] M.D. Stenner, D.J. Gauthier, and M.A. Neifeld, 'Fast causal information transmission in a medium with a slow group velocity,' Phys. Rev. Lett. **94**, 053902 (2005).

[77] M. S. Bigelow, N. N. Lepeshkin, H. Shin, and R. W. Boyd, "Propagation of smooth and discontinuous pulses through materials with very large or very small group velocities," J. Phys.: Condens. Matter **18**, 3117 (2006).

[78] G. M. Gehring, A. Schweinsberg, C. Barsi, N. Kostinski, and R. W. Boyd, "Observation of Backward Pulse Propagation Through a Medium with a Negative Group Velocity," Science, **312**, 895 (2006).

[79] S. E. Schwartz and T. Y. Tan, "Wave interactions in saturable absorbers," Appl. Phys. Lett. **10**, 4 (1967).

[80] L. W. Hillman, R. W. Boyd, J. Krasinski and C.R. Stroud, Jr., "Observation of a spectral hole due to population oscillations in a homogeneous broadened optical absorption line," Opt. Comm. **45**, 416 (1983).

[81] G. Piredda and R. W. Boyd, "Slow light by means of coherent population oscillations: laser linewidth effects," J. Europ. Opt. Soc. **2**, 07004 (2007).

[82] R. J. Mears, L. Reekie, S. B. Poole, and D. N. Payne, "Low-threshold tunable CW and Q-switched fibre laser operating at 1.55μm," Electron. Lett., **22**, 159 (1986).

[83] H. J. Chang, H. Shin, M. N. O'Sullivan-Hale, and R. W. Boyd, "Implementation of sub-Rayleigh-resolution lithography using an N- photon absorber," J. Mod. Opt. **53**, 2271 (2006).

[84] http://refractiveindex.info/

[85] J. A. Moore and Jin O. Choi, "Radiation Effects on Polymers," ACS symposium series **475**, 156 (1991).

[86] T.H.Fedynyshyn, R.R.Kunz, R.F.Sinta, R.B.Goodman, and S.P.Doran, "Polymer photochemistry at advanced optical wavelengths," J. Vac. Sci. Technol. B 18, 3332 (2000).

[87] A. Gupta, R. Liang, F. D. Tsay, and J. Moacanin, "Characterization of a Dissociative Excited State in the Solid State: Photochemistry of Poly(methy1 methacrylate). Photochemical Processes in Polymeric Systems.," Macromolecules, 13, 1696 (1980).

[88] E. J. S. Fonseca, C. H. Monken, and S. Pádua, "Measurement of the de Broglie Wavelength of a Multiphoton Wave Packet," Phys. Rev. Lett. **82**, 2868 (1999).

[89] M. W. Mitchell, J. S. Lundeen, and A. M. Steinberg, "Super-resolving phase measurements with a multiphoton entangled state," Nature **429**, 161 (2004).

[90] T. Nagata, R. Okamoto, J. L. OBrien, K. Sasaki, S. Takeuchi, "Beating the Standard Quantum Limit with Four-Entangled Photons," Science **316**, 726 (2007).

[91] P. Walther, J.-W. Pan, M. Aspelmeyer, R. Ursin, S. Gasparoni, and A. Zeilinger, "De Broglie Wavelength of a Nonlocal Four-Photon State," Nature **429**, 158 (2004).

[92] I. Afek, O. Ambar, and Y. Silberberg, "High-NOON States by Mixing Quantum and Classical Light," Science **328**, 879 (2010).

[93] M. D'Angelo, M. V. Chekhova, and Y. Shih, "Two-Photon Diffraction and Quantum Lithography," Phys. Rev. Lett. **87**, 013602 (2001).

[94] Y. Kawabe, H. Fujiwara, R. Okamoto, K. Sasaki, and S. Takeuchi, "Quantum interference fringes beating the diffraction limit," Opt. Express **15**, 14244 (2007).

[95] J. Gea-Banacloche, "Two-photon absorption of nonclassical light," Phys. Rev. Lett. **62**, 1603 (1989).

[96] J. Javanainen and P. L. Gould, "Linear intensity dependence of a two-photon transition rate," Phys. Rev. A **41**, 5088 (1990).

[97] O. Steuernagel, J. Opt. B: Quantum Semiclass. Opt. **6**, S606 (2004).

[98] M. Tsang, Phys. Rev. A **75**, 043813 (2007).

[99] M. Tsang, Phys. Rev. Lett. **101**, 033602 (2008).

[100] W. N. Plick, C. F. Wildfeuer, P. M. Anisimov, and J. P. Dowling, Phys. Rev. A **80**, 063825 (2009).

[101] M. Tsang, Phys. Rev. Lett. **102**, 253601 (2009).

[102] G. Goltsman et.al. Appl. Phys. Lett. **79**, 705 (2001).

[103] B. Dayan, A. Peer, A. A. Friesem, and Y. Silberberg, Phys. Rev. Lett. **94**, 043602 (2005)

[104] H. Shin, A. Schweinsberg, G. Gehring, K. Schwertz, H. J. Chang, R. W. Boyd, Q. Park, and D. J. Gauthier, "Reducing pulse distortion in fast-light pulse propagation through an erbium-doped fiber amplifier," Opt. Lett. **32**, 906 (2007).

[105] H. Shin, A. Schweinsberg, and R. W. Boyd, "Reducing pulse distortion in fast-light pulse propagation through an erbium-doped fiber amplifier using a mutually incoherent background field," Opt. Commun. **282**, 2085 (2009).

[106] G. P. Agrawal and N. A. Olsson, "Self-Phase Modulation and Spectral Broadening of Optical Pulses in Semiconductor Laser Amplifiers," IEEE J. Quantum Elect. **25**, 2297 (1989).

[107] H. Cao, A. Dogariu, and L. J. Wang, "Negative Group Delay and Pulse Compression in Superluminal Pulse Propagation," IEEE J Sel. Top. QUANT. **9**, 52 (2003).

[108] P. F. Wysocki, R. F. Kalman, M. J. F. Digonnet, and B. Y. Kim, "A comparison of 1.48 μm and 980 nm pumping for Er-doped superfluorescent fiber sources," Proc. SPEI, Fiber Laser Sources and Amplifiers III 1581, 40 (1991).

[109] P. F. Wysocki, J. L. Wagener, M. J. F. Digonnet, and H. J. Shaw, "Evidence and modeling of paired ions and other loss mechanisms in erbium-doped silica fibers," Proc. SPEI, Fiber Laser Sources and Amplifiers IV 1789, 66 (1992).

[110] P.C. Becker, N.A. Olsson, and J.R. Simpson, *Erbium-Doped Fiber Amplifiers.* (Academic Press, 1999).

[111] B. E. A. Saleh and Malvin Carl Teich, *Fundamentals of Photonics.* (Wiley-Interscience, 2007).

[112] P. Ku, F. Sedgwick, C. J. Chang-Hasnain, P. Palinginis, T. Li, H. Wang, S. Chang, and S. Chuang, "Slow light in semiconductor quantum wells," Opt. Lett. **29**, 2291 (2004).

[113] P. Palinginis, S. Crankshaw, F. Sedgwick, E. Kim, M. Moewe, C. J. Chang-Hasnain, H. Wang, and S. Chuang, "Ultraslow light (< 200 m/s) propagation in a semiconductor nanostructure," Appl. Phys. Lett. **87**, 171102 (2005).

[114] H. Su and S. L. Chuang, "Room temperature slow and fast light in quantum-dot semiconductor optical amplifiers," Appl. Phys. Lett. **88**, 061102 (2006).